Washington University in St. Louis

## Washington University Open Scholarship

January 2010

# Electrospray Methodologies for Characterization and Deposition of Nanoparticles

Luis Balam Modesto Lopez
*Washington University in St. Louis*

Follow this and additional works at: https://openscholarship.wustl.edu/etd

WASHINGTON UNIVERSITY

School of Engineering and Applied Science

Department of Energy, Environmental & Chemical Engineering

Dissertation Examination Committee:

Pratim Biswas, Chair
Richard Axelbaum
Robert E. Blankenship
Da-Ren Chen
Young-Shin Jun
Jill D. Pasteris

ELECTROSPRAY METHODOLOGIES FOR CHARACTERIZATION AND

DEPOSITION OF NANOPARTICLES

by

Luis Balam Modesto López

A dissertation presented to the
Graduate School of Arts and Sciences
Of Washington University in
Partial fulfillment of the
Requirements for the degree
Of Doctor of Philosophy

May, 2010

Saint Louis, MO

**Abstract of Dissertation**

Electrospray Methodologies for Characterization and Deposition of Nanoparticles

by

Luis Balam Modesto López

Doctor of Philosophy in Energy, Environmental and Chemical Engineering

Washington University in St. Louis, 2010

Professor Pratim Biswas, Chairperson


Electrospray is an aerosolization method that generates highly charged droplets from solutions or suspensions and, after a series of solvent evaporation – droplet fission cycles, it results in particles carrying multiple charges. Highly charged particles are used in a variety of applications, including particle characterization, thin film deposition, nanopatterning, and inhalation studies among several others. In this work, a soft X-ray photoionization was coupled with an electrospray to obtain monodisperse, singly charged nanoparticles for applications in online size characterization with electrical mobility analysis. Photoionization with the soft X-ray charger enhanced the diffusion neutralization rate of the highly charged bacteriophages, proteins, and solid particles. The effect of nanoparticle surface charge and nanoparticle agglomeration in liquids on the electrospray process was studied experimentally and a modified expression to calculate the effective electrical conductivity of nanosuspensions was proposed. The effective electrical conductivity of $TiO_2$ nanoparticle suspensions is strongly dependent on the electrical double layer and the agglomeration dynamics of the particles; and such dependence is more remarkable in liquids with low ionic strength. $TiO_2$ nanoparticle

agglomerates with nearly monodisperse sizes in the nanometer and submicrometer ranges were generated, by electrospraying suspensions with tuned effective electrical conductivity, and used to deposit photocatalytic films for water-splitting. Nanostructured films of iron oxide with uniform distribution of particles over the entire deposition area were formed with an electrospray system. The micro-Raman spectra of the iron oxide films showed that transverse and longitudinal optical modes are highly sensitive to the crystallize size of the electrospray-deposited films. The fabrication of films of natural light-harvesting complexes, with the aim of designing biohybrid photovoltaic devices, was explored with an electrospray. The ability to charge chlorosomes with large number of charges allowed their ballistic deposition onto $TiO_2$ nanostructured columnar films simultaneously maintaining their light-harvesting properties. Single units of natural light-harvesting complexes were isolated in charged electrospray droplets for subsequent size characterization. The charge distribution of natural light-harvesting complexes, aerosolized with a collision nebulizer, was determined with tandem differential mobility analysis. It was found that nebulized light-harvesting complexes were multiply charged; hence they have potential applications in the deposition of functional films using electric fields. The studies conducted as part of this dissertation addressed fundamental issues in the characterization and deposition of nanoparticle suspensions and elucidated applications of the electrospray technique, particularly for solar energy utilization.

**Table of Contents**

**Chapter 3: Role of the Effective Electrical Conductivity of Nanosuspensions in the Generation of TiO$_2$ Agglomerates with Electrospray ...................................................52**

# List of Figures

**Chapter 4**

**Chapter 6**

**Appendix I**

# Chapter 1: Background and Overview

**1.1 Background**

This dissertation focuses on the characterization of nanomaterials and their deposition characteristics by electrospray. Here, the term nanomaterials refers to solid or biological materials in the form of particles or films, having at least one dimension below 100 nm and unique physicochemical properties or functionalities. Electrospray is an aerosolization method that involves both mechanical and electrical forces to feed a liquid through a capillary and to create an electric field gradient between the capillary tip and an electrode, respectively. When the mechanical and electrical forces in the liquid meniscus at the capillary outlet are in equilibrium, the liquid takes a conical shape, called a Taylor cone, and emits a liquid jet [1-3]. Viscous instabilities in the liquid cause the jet to break into highly charged droplets that undergo a series of fissions and generate smaller droplets, until the solvent completely evaporates [2]. Electrospray produces highly charged droplets with a nearly monodisperse size distribution, and the average droplet diameter can be precisely controlled from tens of nanometers to tens of micrometers, by adjusting process parameters [4-6]. Electrospray of a liquid containing a uniformly dissolved solute will result in the production of ions, whereas electrospray of a suspension will generate highly charged particles. Both its ability to generate highly charged, monodisperse droplets in a well-controlled mode and its efficacy to produce nanoparticles with a high charge-state make the electrospray a unique method to generate airborne single particles or particle agglomerates for inhalation studies and targeted drug delivery [7-12], to produce highly charged ions for mass spectrometry analyses [13-16], and to deposit layered structures with tailored feature size for nanostructured film fabrication [17-31]. Industrial and agricultural processes such as car painting and crop spraying also employ electrospray, and there is

interest in using electrospray as a source of colloid thrusters for satellite propulsion[7].

The physicochemical properties of nanoparticle suspensions are strongly related to the size and concentration of the suspended particles and to their electrokinetic phenomena[32-37]. A nanoparticle suspension, also called a nanofluid or nanosuspension, contains particles with diameters ranging from a few nanometers to approximately 100 nm. An increase in the particle number density of nanosuspensions enhances the effective viscosity and the thermal and electrical conductivities. Literature reports suggest that the electrical conductivity of nanoparticle suspensions is influenced not only by the conductivities of the liquid and the particle material, but also by both the net surface charge and the agglomeration of the particles[33, 35-37]. In this dissertation, particle agglomeration refers to the formation of particle clusters, by collision due to the Brownian motion of particles, held together by weak interparticle electrostatic interactions; the resulting particle clusters are called agglomerates. In an electrospray, when the capillary geometry and the liquid flow rate are fixed, the effective electrical conductivity of the liquid is the ultimate parameter that influences the droplet formation and discharge dynamics because it not only affects the liquid motion inside Taylor cones[38], by inducing viscosity changes, but also controls the number density of charge carriers that determine the droplet charge[15]. Hence, in electrospray of nanosuspensions the effective electrical conductivity may influence the size, morphology, and charge-state of the resulting particles or agglomerates. Thus, we must assess the final properties and transport characteristics of nanomaterials generated by an electrospray, both of which are size dependent, to effectively implement them in suitable applications.

The characterization of nanomaterials with gas-phase methodologies requires generating an aerosol from a powder or a nanosuspension, followed by analyzing it via light scattering, mass spectrometry, or electrical mobility measurements. A number of simple aerosolization techniques, such as nebulization or atomization, produce a large droplet size (in the micrometer range) that causes the formation of particle agglomerates [39], and hence they are not appropriate when a single particle needs to be analyzed with high precision. In contrast, a technique such as electrospray allows us to generate single nanoparticles or to fragment macromolecules into their main components [8, 40-42]. Solid-phase analytical techniques, which complement gas-phase methodologies, are generally performed using, for example, electron microscopy techniques, X-ray diffraction (XRD), and micro-Raman (μ-Raman) spectroscopy. All those methods require that the material be immobilized onto a substrate while still maintaining its integrity. After we have analyzed a nanomaterial, the next step is to process it for particular applications.

The specific application dictates the desired nanomaterial properties, including size, morphology, and charge-state. For applications in aerosol-assisted size characterization techniques, researchers desire to maximize the output of the particle number density from the aerosolization instrument to improve the sensitivity of the detection equipment. However, for applications in inhalation studies with animals or targeted drug delivery, both a higher output particle number density and tight control of particle size and charge would be relevant to assess precisely the deposition location of particles in the respiratory tract and dosage effect. For thin-film and coating applications

we are more concerned with the film uniformity, morphology, and porosity as well as with the crystal size of the individual grains that form the film.

To link all the aspects of characterization and deposition of nanomaterials with electrospray, this introductory chapter briefly explains the interaction of nanoparticles in liquids, the mechanism through which nanoparticles acquire charge in the electrospray, and the methodologies to reduce the charge-state of electrosprayed nanoparticles. Next, each of the following chapters in the dissertation is outlined, emphasizing the fundamental questions and motivation behind each study.

### 1.1.1 Nanoparticle Interactions in a Liquid

In electrosprays, the liquid electrical conductivity is one key parameter that determines the jet and droplet formation dynamics[38, 43, 44]. Several studies have proposed that conductivity phenomena of nanoparticle suspensions differ largely from those of micrometer (or larger) size particles[32-34, 36, 37, 45]; hence, it is very pertinent for the purpose of this dissertation to explain both the interaction of nanoparticles in a liquid and the role of nanoparticles in modifying the liquid conductivity.

Nanoparticles have more uncoordinated bonds at the surface compared to larger particles, in addition to the ion vacancies, interstitials, and surface chemistry specific to each material[46-48]. These surface phenomena impart a net charge to the nanoparticles such that when suspended in a liquid medium, an ionic layer called an electrical double layer (EDL) develops around them. This ionic layer, which moves along with the particle and influences its electrophoretic mobility, is composed mainly of ions of opposite

polarity to that of the nanoparticle net surface charge. The thickness of the EDL depends

on the strength of the particle surface charge and the ionic strength of the liquid medium.

Thicker EDLs tend to prevent particle agglomeration and sedimentation because of the

electrostatic repulsion between adjacent nanoparticles, but they also tend to decrease the

particle electrophoretic mobility because of an increased drag on the particle. Due to the

complexity of these colloidal phenomena, we can consider different case scenarios. For

instance, consider a case where the particle number density in a liquid is relatively high

such that the frequency of interparticle collisions associated with the random motion of

particles is also high. In such a case, if the EDL is sufficiently thin, the interparticle

collision rate increases and particles agglomerate and sediment. In the case of thicker

EDLs, the electrostatic repulsion between the EDLs of adjacent particles prevents particle

agglomeration. However, at even higher ionic strengths the electrostatic repulsion of

adjacent nanoparticles is high enough to cause a compression of the EDL, thereby

resulting in an increase of the particle agglomeration rate [49]. For particles to collide and

agglomerate, they need to overcome a potential energy barrier beyond which the collision

process is not reversible. Recent experimental data show that the effective electrical

conductivity of nanoparticle suspensions arises from a contribution of both the particle

agglomeration and the EDL, and not just from the individual conductivities of the liquid

and the particles. More specifically, nanoparticle agglomerates and their resulting

networks represent a pathway for charge conduction while thicker EDLs enhance ion

diffusion in the liquid. In electrospray of nanosuspensions, these combined nanoparticle

effects may contribute to variations in the number density of charge carriers present in the

liquid, hence they may significantly influence both the droplet's surface conductivity and the charging dynamics.

1.1.2 Nanomaterials Charging with Electrospray

This section gives a qualitative explanation of the mechanism by which an electrospray generates charged droplets and nanoparticles. Several authors have done quantitative descriptions using theoretical calculations and numerical simulations, which are omitted here [1, 5, 38, 50-54]. First, this section describes a standard electrospray setup, and then explains the charging mechanisms that occur in the electrospray.

A typical electrospray system (Figure 1-1) consists of a capillary needle through which a liquid that may be a pure solvent, a solution, or a suspension is fed using a syringe pump; a high voltage source connected to the capillary; and a grounded electrode placed perpendicularly to the capillary to create a strong electric field gradient. The capillary needle is generally tapered and made of a conductive material. The grounded electrode shape may vary from a ring-like electrode to a plate, depending on the application of the electrospray [55]. A particular requirement is that the liquid must exhibit some conductivity. As the liquid flows through the capillary, the voltage is increased to a critical value where the mechanical and the electrostatic forces in the liquid are in equilibrium. At this point, the liquid meniscus at the capillary tip takes the shape of a cone and emits a liquid jet to minimize the surface charge density. This is the so-called Taylor cone, named after Sir G. I. Taylor [3]. Furthermore, the shear stress in the liquid causes instabilities that result in jet breakup and in the formation of droplets. Droplets

produced in this way are highly charged because during the jet breakup process the flow of charge is also transferred from the jet to the droplets. The electrospray has various modes of operation; however, the cone-jet mode is the most widely used for its stability and for producing nearly monodisperse droplets.
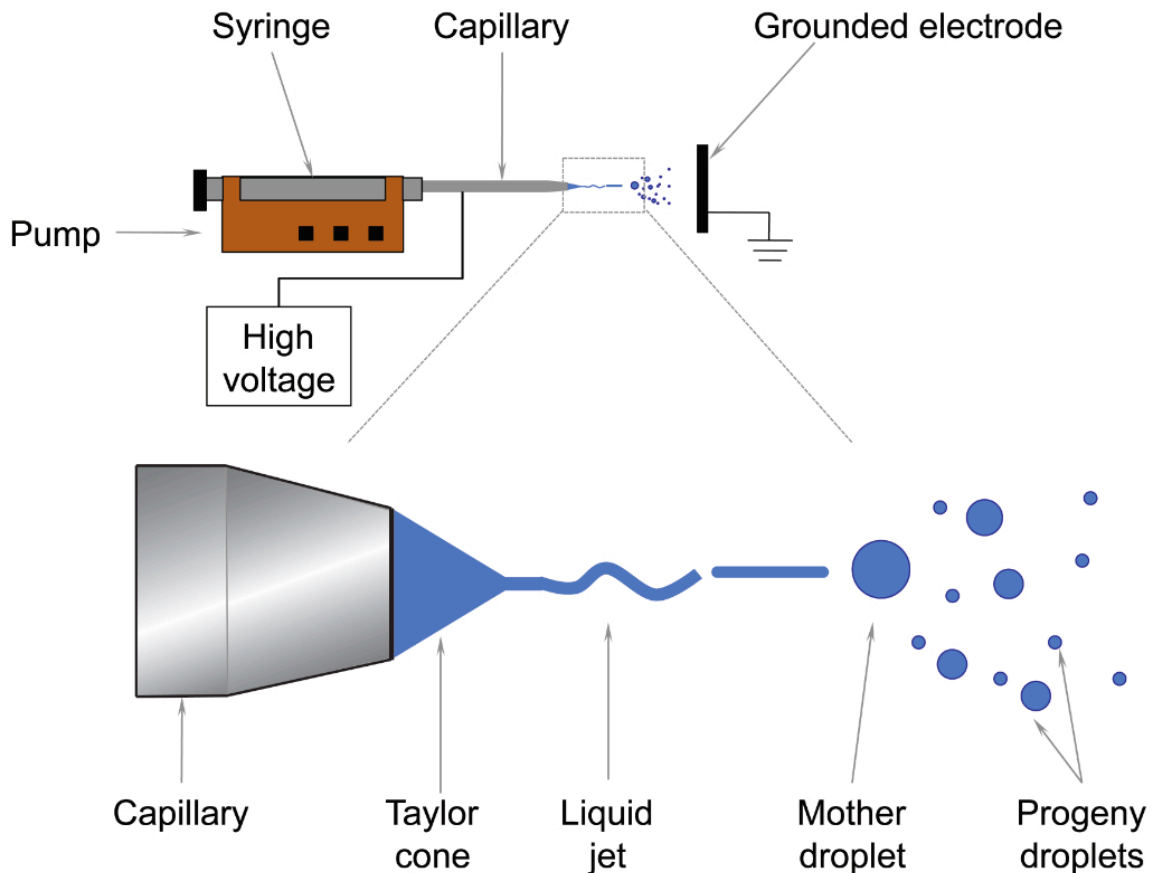


**Figure 1-1:** Standard electrospray system for film deposition.

As a highly charged droplet evaporates, its mass decreases while the number of charges on the droplet remains constant; thus the surface charge density increases. Simultaneously, the electrostatic repulsion between charges of the same polarity

increases at the drop surface[2, 56]. At a critical point, known as the Rayleigh limit[57], the electrostatic repulsive force becomes of the same order as the attractive surface tension. Above the Rayleigh limit, the droplet will become unstable and will release charge through a series of fissions. Literature reports identify two mechanisms of droplet fissions. In the first mechanism, defined as a rough fission mode[2] and observed in droplets with low electrical conductivity, a droplet breaks into a few progeny droplets of similar size, whereas in the second mechanism, a droplet forms one or several Taylor cones and emits much finer droplets than the progeny droplets generated in the first mechanism[58]. This droplet evaporation-fission cycle will continue for both the initial and the progeny droplets until the solvent depletes. Experimental work done with micrometer-sized droplets indicate that a droplet loses approximately 1-2 % of its mass and up to 50 % of its Rayleigh limit charge in each fission[44]. Some authors have proposed that the charge-to-mass ratio of a progeny droplet is proportional to the electrical conductivity at the surface of the mother droplet, whereas its size scales inversely proportional to the mother droplet's surface electrical conductivity raised to the power 2/3[44].

Some researchers have proposed that in highly charged droplets of pure liquids or solutions, ions are generated by an ion emission mechanism (IEM), in which the potential energy of ions distributed on a diffuse layer around the drop surface overcomes the Gibbs free energy barrier and allows ions to "evaporate"[59]. A field of the order of $10^9$ V/m must be applied before ions have a reasonable probability to escape the drop surface. Conversely, other researchers have suggested that in highly charged droplets containing nanoparticles or macromolecules the charge on the drop surface is transferred to the

particles enclosed in it; this is the so-called charge residue mechanism (CRM)[60]. However, some other authors have proposed macromolecules acquire charge by the IEM, and not by the CRM, depending on their solvation state in the charged droplet[15, 61]. Data found in the literature indicates that the number of charges on a electrosprayed nanoparticle scales with the square of particle size, which is proportional to the particle surface area[62]. Regardless of the charging mechanism, we must reduce the high charge-state of nanoparticles produced by electrospray, to avoid particle losses, if we desire to characterize them with electrical mobility or light scattering techniques.

### 1.1.3 Charge Neutralization Methods

Nanoparticle size characterization methods that employ an electrospray and electrical mobility-based techniques[63] reduce the initial high charge-state of the particles to a known equilibrium state. Charge-reduction is essential to avoid particle losses, due to external electric fields, and to determine the particle size accurately. The main charge neutralization mechanism for highly charged aerosol particles is diffusion neutralization, also referred to interchangeably as diffusion charging. While several numerical models of diffusion charging exist in literature[64-67] this section explains only the generalities of the diffusion charging mechanism and its relevance to the electrospray process.

In diffusion neutralization, highly charged aerosol particles are exposed to a bipolar ion environment[68] where they lose charge by random collisions with ions of opposite polarity. The frequent ion-particle collisions will bring the particles to a state of charge equilibrium with the ionic atmosphere. Note that a similar mechanism using

unipolar ions is used to charge particles[39]. In the charge-equilibrium state, a Boltzmann distribution describes the fraction of charged particles, and experimental studies have demonstrated that after sufficient long exposure time to the bipolar ion mixture most particles carry 0 or at most ±1 charge. The key ion properties that determine the particle charging probabilities are electrical mobility, mass, diffusion coefficient, mean thermal velocity, and mean free path[69]. Since these properties are interdependent, usually ion mobility and mass are applied to derive the others. If the positive and negative ion number densities are initially balanced, the charge-state of the aerosol particles will eventually reach a quasi steady state at which the rate of attachment of positive ions exactly balances the rate of attachment of negative ions[70]. Both the Boltzmann equilibrium charge distribution and the quasi steady state are particularly important for particle size characterization via electrical mobility analysis because the most commonly used instruments have been designed based on theories that assume singly charged particles in a steady state charge distribution[63]. Additionally, for practical purposes we desire that the number density of bipolar ions be sufficiently high to increase the ion-particle collision probability so that the particles reach the equilibrium charge-state "instantaneously". $Am^{241}$, $Kr^{85}$, and $Po^{210}$ are the most widely used sources of bipolar ions in aerosol instrumentation[68, 71, 72]. Although these materials have proven to be effective, their performance is limited to narrow ranges of gas flow rate, relative humidity, and gas media, and they must be handled with extreme caution because of their radioactive nature. In the literature, a methodology to generate monodisperse, singly charged particles using an electrospray and a $Po^{210}$ source was proposed, and this method has been routinely employed by researchers across various fields to characterize a wide

range of nanomaterials including, metal oxides, macromolecules, viruses, and natural light-harvesting structures among several others [8, 21, 42, 73]. Nevertheless, from a safety perspective, we desire alternative technologies to avoid the use of radioactive sources.

## 1.2 Overview

Despite numerous studies, several issues in the investigation of electrospray methodologies for characterization and deposition of nanoparticle suspensions still remain unresolved. Aerosol scientists have studied a variety of methods to equilibrate the charge-state of electrosprayed nanomaterials for electrical mobility analysis. However, there are no literature reports on the evaluation of bipolar ion sources with the ability to produce a sufficiently high ion number density environment in a controlled and stable manner, which could be a potential alternative for radioactive neutralizers. The existing scaling laws of electrospray predict the size of pure, highly conductive liquid droplets. However, these mathematical expressions do not address the influence of nanoparticle interactions in liquids and the stability of a precursor nanosuspension on the size distribution and morphology of electrosprayed particles or agglomerates. Furthermore, previous studies of electrospray deposition of suspensions [74-76] did not investigate the influence of both the size and the morphology of the depositing particles or particle agglomerates on the film porosity and thickness. Despite the use of electrospray in a variety of nanostructured film processing applications, its efficacy both to process natural photosynthetic antennae and to design biohybrid photovoltaic devices has not been explored. The studies performed as part of this dissertation were aimed to address these questions on the characterization and deposition of a wide range of nanomaterials

including metal oxide nanoparticles, proteins, viruses, and photosynthetic complexes. These materials were selected because of their novel properties and potential use in energy and environmental studies, which include photovoltaics, soil and water remediation, capture of gaseous contaminants, and inhalation studies with animals among several others.

1.2.1 Objectives

The objectives of this dissertation were as follows:

- To evaluate the efficacy of an electrospray – soft x-ray charger (SXC) system to generate monodisperse, singly charged nanoparticles for online electrical mobility analysis.

- To determine the effect of both nanoparticle surface charge and nanoparticle agglomeration in precursor suspensions on the size distribution and morphology of agglomerates produced by electrospray.

- To study the electrospray-deposition characteristics of nanoparticle suspensions, including crystallite size and porosity of the films.

- To investigate the feasibility of electrospray to aerosolize charged, single units of natural light-harvesting complexes, which have delicate structures and can be used to design photovoltaic devices.

The specific materials used in the studies conducted as part of this dissertation and their characteristics of interest are summarized in Table 1-1.

**Table 1-1:** Summary of nanomaterials used in the studies of this dissertation

| Material | Characteristics | Applications |
| --- | --- | --- |
| $TiO_2$ nanoparticles | Well-known photocatalytic material, produced in large scale. | Photocatalytic films by light activation. Investigation of agglomerate formation for drug delivery and inhalation studies. |
| $Fe_2O_3$ nanoparticles | Light absorption in the visible range. | Photocatalytic films, pigments, water and soil remediation. Studies of crystal growth with spectroscopic techniques. |
| Ovalbumin (OVA) protein | Protein with diameter in the nanometer range (~6.3 nm), readily available. | Aerosolization for inhalation studies in animals. |
| MS2 bacteriophages | Surrogate of viruses, nanosized and monodisperse particle. | Studies of virus capture and inactivation. Aerosolization for inhalation studies in animals. |
| Chlorosomes | Highly efficient light-harvesting antenna, resistant to extreme conditions of light and temperature. | Biohybrid light-harvesting devices. Studies of photosynthesis. |
| Light-harvesting 2 (LH2) complex | Efficient natural photosynthetic systems | Biohybrid light-harvesting devices. Studies of photosynthesis. |
| Fenna-Matthews-Olson (FMO) protein | Component of the photosynthetic structure in green sulfur bacteria | Linker for energy transfer from the chlorosome to a reaction center in the cell membrane. |
| Poly(3-octylthiophene-2,5-diyl) (P3OT) | Conducting polymer | Photovoltaics for fabrication of organic solar cells heterojunctions |

1.2.2 Outline

This section describes the content of the dissertation and highlights the most relevant outcomes of each chapter. Chapter 2 discusses the coupling of a soft X-ray charger (SXC) with an electrospray for online electrospray size spectrometry analyses of bioparticles. A SXC was effectively and safely implemented as a source of bipolar ions to reduce the high charge-state of electrosprayed nanoparticles. Chapter 3 focuses on $TiO_2$ nanoparticle interactions in liquids with varying electrical conductivity and on the electrospray characteristics of nanosuspensions to generate agglomerates with tailored sizes. The study proposes an expression to calculate the effective electrical conductivity of $TiO_2$ nanosuspensions by considering particle surface charge and particle agglomeration effects in the precursor suspension. Then, it describes a facile methodology to generate airborne, highly charged nanoparticle agglomerates in the submicrometer size range that were applied to the deposition of photocatalytic films. Nevertheless, the generation of nanoparticle agglomerates with tightly controlled sizes may be beneficial for other research areas such as inhalation studies with animals. Chapter 4 explains the electrospray-deposition of iron oxide nanostructured films and their characterization using micro-Raman spectroscopy. Deposition with electrospray facilitated the control of the film area, provided a uniform distribution of grain sizes needed to test the statistical variation of the Raman spectra, and allowed flexibility in the choice of substrate material. The study demonstrated that the spectral separation between two optical modes, characteristic of the Raman spectra of hematite, could be used to estimate the crystallite size of nanostructured films. Chapter 5 focuses on the characterization of natural light-harvesting complexes aerosolized with electrospray and

nebulization methods. The results demonstrate that we can highly charge light-harvesting complexes and isolate their single units in electrospray droplets to precisely measure their size in real time. The study also found that light-harvesting complexes formed clusters in droplets generated with a nebulizer and that they carried multiple charges. Chapter 6 addresses the use of electrospray for the characterization of chlorosomes, a natural photosynthetic antenna system, and for the fabrication of biohybrid photovoltaic devices. The key aspect in the study was the use of an electrospray system to aerosolize chlorosomes, and then deposit them using electric fields. The incompatibility issue between some of the components of the biohybrid device was overcome by a sequential process: aerosolization, drying in flight, followed by deposition. The approach demonstrated in Chapter 6 has broader applicability in the characterization and sequential deposition of components with varying chemistry to fabricate biomimetic solar cells. Chapter 7 summarizes the major outcomes of this dissertation and discusses its future and broader implications. Finally, Appendix I summarizes my (LBML) curriculum vitae at the time of completion of this dissertation and a list of coursework attended at Washington University in St. Louis.

To assist readers, each chapter is written such that it may stand alone as a description of a body of research, with an introduction and conclusions section tailored to the particular audience. Readers are referred to other chapters of this dissertation or other references when appropriate. To aid readers in finding appropriate citation information, each chapter contains its own list of references. Some references are cited in multiple chapters and therefore appear in multiple reference sections.

**1.3 References**

1. D.-R. Chen and D. Y. H. Pui. Experimental investigation of scaling laws for

electrospraying: Dielectric constant effect. *Aerosol Sci. Tech.*, 1997, **27**(3), 367-

380.

2. J. F. de la Mora. On the outcome of the coulombic fission of a charged isolated drop. *J.

Colloid. Interf. Sci.*, 1996, **178**(1), 209-218.

3. G. Taylor. Disintegration of water drops in an electric field. *Proceedings of the Royal

Society of London. Series A, Mathematical and Physical Sciences*, 1964,

**280**(1382), 383-397.

4. D.-R. Chen, D. Pui, and S. Kaufman. Electrospraying of conducting liquids for

monodisperse aerosol generation in the 4 nm to 1.8 μm diameter range. *J. Aerosol

Sci.*, 1995, **26**(6), 963-977.

5. A. M. Ganan-Calvo, J. Davila, and A. Barrero. Current and droplet size in the

electrospraying of liquids. Scaling laws. *J. Aerosol Sci.*, 1997, **28**(2), 249-275.

6. J. Rosell-Llompart and J. F. de la Mora. Generation of monodisperse droplets 0.3 to 4

μm in diameter from electrified cone-jets of highly conducting and viscous-

liquids. *J. Aerosol Sci.*, 1994, **25**(6), 1093-1119.

7. M. Gamero-Castano and V. Hruby. Electrospray as a source of nanoparticles for

efficient colloid thrusters. *J. Propul. Power*, 2001, **17**(5), 977-987.

8. C. J. Hogan, E. M. Kettleson, B. Ramaswami, D. R. Chen, and P. Biswas. Charge

reduced electrospray size spectrometry of mega- and gigadalton complexes:

Whole viruses and virus fragments. *Anal. Chem.*, 2006, **78**(3), 844-852.

9. C. J. Hogan, M. H. Lee, and P. Biswas. Capture of viral particles in soft X-ray-enhanced corona systems: Charge distribution and transport characteristics. *Aerosol Sci. Tech.*, 2004, **38**(5), 475-486.

10. A. Gomez. The electrosrpay and its application to targeted drug delivery. *Respir. Care*, 2002, **47**(12), 1419-.

11. A. Gomez, D. Bingham, L. de Juan, and K. Tang. Production of protein nanoparticles by electrospray drying. *J. Aerosol Sci.*, 1998, **29**(5-6), 561-574.

12. J. C. Ijsebaert, K. B. Geerse, J. C. M. Marijnissen, J. W. J. Lammers, and P. Zanen. Electro-hydrodynamic atomization of drug solutions for inhalation purposes. *J. Appl. Physiol.*, 2001, **91**(6), 2735-2741.

13. J. B. Fenn. Ion formation from charged droplets - roles of geometry, energy, and time. *J. Am. Soc. Mass Spectrom.*, 1993, **4**(7), 524-535.

14. J. B. Fenn. Electrospray wings for molecular elephants (Nobel lecture). *Angew. Chem. Int. Edit.*, 2003, **42**(33), 3871-3894.

15. C. J. Hogan, J. A. Carroll, H. W. Rohrs, P. Biswas, and M. L. Gross. Charge carrier field emission determines the number of charges on native state proteins in electrospray ionization. *J. Am. Chem. Soc.*, 2008, **130**(22), 6926-6927.

16. S. Zhou, B. Prebyl, and K. Cook. Profiling pH changes in the electrospray plume. *Anal. Chem.*, 2002, **74**(19), 4885-4888.

17. B. Lee. Fabrication of a protein film by electrospray deposition method and investigation of photochemical properties by persistent spectral hole burning. *Biomaterials*, 2003, **24**(12), 2045-2051.

18. I. Lenggoro, K. Okuyama, J. Fernandez de la Mora, and N. Tohge. Preparation of
    ZnS nanoparticles by electrospray pyrolysis. *J. Aerosol Sci.*, 2000, **31**(1), 121.

19. I. W. Lenggoro, H. M. Lee, and K. Okuyama. Nanoparticle assembly on patterned
    "plus/minus" surfaces from electrospray of colloidal dispersion. *J. Colloid. Interf.
    Sci.*, 2006, **303**(1), 124-130.

20. X. Li, J. Huang, Z. Ahmad, and M. Edirisinghe. Electrohydrodynamic coating of
    metal with nano-sized hydroxyapatite. *Bio-Med. Mater. Eng.*, 2007, **17**(6), 335-
    346.

21. L. B. Modesto-Lopez, A. M. Collins, R. E. Blankenship, and P. Biswas. Electrospray-
    assisted characterization and deposition of chlorosomes to fabricate a light-
    harvesting biomimetic device. *Energy Environ. Sci.*, 2010, **3**, 216 - 222.

22. L. B. Modesto-Lopez, J. D. Pasteris, and P. Biswas. Sensitivity of micro-Raman
    spectrum to crystallite size of electrospray-deposited and post-annealed films of
    iron-oxide nanoparticle suspensions. *Appl. Spectr.*, 2009, **63**(6), 627-635.

23. V. N. Morozov and T. Y. Morozova. Electrospray deposition as a method to fabricate
    functionally active protein films. *Anal. Chem.*, 1999, **71**(7), 1415-1420.

24. V. N. Morozov and T. Y. Morozova. Electrospray deposition as a method for mass
    fabrication of mono- and multicomponent microarrays of biological and
    biologically active substances. *Anal. Chem.*, 1999, **71**(15), 3110-3117.

25. I. B. Rietveld, K. Kobayashi, H. Yamada, and K. Matsushige. Electrospray
    deposition, model, and experiment: Toward general control of film morphology.
    *J. Phys. Chem. B*, 2006, **110**(46), 23351-23364.

26. R. Saf, M. Goriup, T. Steindl, T. E. Hamedinger, D. Sandholzer, and G. Hayn. Thin organic films by atmospheric-pressure ion deposition. *Nat. Mater.*, 2004, **3**(5), 323-329.

27. W. D. Teng, Z. A. Huneiti, W. Machowski, J. R. G. Evans, M. J. Edirisinghe, and W. Balachandran. Towards particle-by-particle deposition of ceramics using electrostatic atomization. *J. Mater. Sci. Lett.*, 1997, **16**(12), 1017-1019.

28. I. Uematsu, H. Matsumoto, K. Morota, M. Minagawa, A. Tanioka, Y. Yamagata, and K. Inoue. Surface morphology and biological activity of protein thin films produced by electrospray deposition. *J. Colloid. Interf. Sci.*, 2004, **269**(2), 336-340.

29. A. Vanzomeren, E. Kelder, J. Marijnissen, and J. Schoonman. The production of thin-films of LiMn2O4 by electrospraying. *J. Aerosol Sci.*, 1994, **25**(6), 1229-&.

30. O. Wilhelm, S. Pratsinis, D. Perednis, and L. Gauckler. Electrospray and pressurized spray deposition of yttria-stabilized zirconia films. *Thin Solid Films*, 2005, **479**(1-2), 121-129.

31. J. Xie, J. Tan, and C. Wang. Biodegradable films developed by electrospray deposition for sustained drug delivery. *Journal of Pharmaceutical Sciences*, 2008, **97**(8).

32. K. Anoop, S. Kabelac, and T. Sundararajan. Rheological and flow characteristics of nanofluids: Influence of electroviscous effects and particle agglomeration. *J. Appl. Phys.*, 2009, **106**(3), 034909.

33. S. Chakraborty and S. Padhy. Anomalous electrical conductivity of nanoscale colloidal suspensions. *Acs Nano*, 2008, **2**(10), 2029-2036.

34. J. Crawshaw and G. Meeten. Shear-induced changes of electrical conductivity in suspensions. *Rheol. Acta*, 2006, **46**(2), 183-193.

35. R. C. D. Cruz, J. Reinshagen, R. Oberacker, A. M. Segadaes, and M. J. Hoffmann. Electrical conductivity and stability of concentrated aqueous alumina suspensions. *J. Colloid. Interf. Sci.*, 2005, **286**(2), 579-588.

36. F. Fang and Y. F. Zhang. DC electrical conductivity of Au nanoparticle/chloroform and toluene suspensions. *J. Mater. Sci.*, 2005, **40**(11), 2979-2980.

37. S. Ganguly, S. Sikdar, and S. Basu. Experimental investigation of the effective electrical conductivity of aluminum oxide nanofluids. *Powder Technol.*, 2009, **196**(3), 326-330.

38. A. Barrero, A. M. Ganan-Calvo, J. Davila, A. Palacios, and E. Gomez-Gonzalez. The role of the electrical conductivity and viscosity on the motions inside Taylor cones. *J. Electrostat.*, 1999, **47**(1-2), 13-26.

39. W. C. Hinds. 1999, New York: John Wiley & Sons.

40. S. L. Kaufman. Analysis of biomolecules using electrospray and nanoparticle methods: The gas-phase electrophoretic mobility analyzer (GEMMA). *J. Aerosol Sci.*, 1998, **29**(5/6).

41. I. Lenggoro, B. Xia, K. Okuyama, and J. F. de la Mora. Sizing of colloidal nanoparticles by electrospray and differential mobility analyzer methods. *Langmuir*, 2002, **18**(12), 4584-4591.

42. G. Allmaier, C. Laschober, and W. Szymanski. Nano ES GEMMA and PDMA, new tools for the analysis of nanobioparticles—protein complexes, lipoparticles, and viruses. *J. Am. Soc. Mass Spectrom.*, 2008, **19**(8), 1062-1068.

43. A. Barrero, A. Ganan-Calvo, J. Davila, A. Palacio, and E. Gomez-Gonzalez. Low and high Reynolds number flows inside Taylor cones. *Phys. Rev. E*, 1998, **58**(6), 7309-7314.

44. H. C. Hunter and A. K. Ray. On progeny droplets emitted during Coulombic fission of charged microdrops. *Phys. Chem. Chem. Phys.*, 2009, **11**(29), 6156-6165.

45. J. Widegren and L. Bergstrom. Electrostatic stabilization of ultrafine titania in ethanol. *J. Am. Ceram. Soc.*, 2002, **85**(3), 523-528.

46. M. K. Nowotny, T. Bak, and J. Nowotny. Electrical properties and defect chemistry of TiO2 single crystal. I. Electrical conductivity. *J. Phys. Chem. B*, 2006, **110**(33), 16270-16282.

47. M. K. Nowotny, T. Bak, and J. Nowotny. Electrical properties and defect chemistry of TiO2 single crystal. III. Equilibration kinetics and chemical diffusion. *J. Phys. Chem. B*, 2006, **110**(33), 16292-16301.

48. Y. Tang and M. Ouyang. Tailoring properties and functionalities of metal nanoparticles through crystallinity engineering. *Nat. Mater.*, 2007, **6**(10), 754-759.

49. J. K. Jiang, G. Oberdorster, and P. Biswas. Characterization of size, surface charge, and agglomeration state of nanoparticle dispersions for toxicological studies. *J. Nanopart. Res.*, 2009, **11**(1), 77-89.

50. J. F. de la Mora. The fluid dynamics of Taylor cones. *Annu. Rev. Fluid. Mech.*, 2007, **39**, 217-243.

51. J. F. de la Mora and I. G. Loscertales. The current emitted by highly conducting Taylor cones. *J. Fluid. Mech.*, 1994, **260**, 155-184.

52. R. P. A. Hartman, D. J. Brunner, D. M. A. Camelot, J. C. M. Marijnissen, and B. Scarlett. Electrohydrodynamic atomization in the cone-jet mode physical modeling of the liquid cone and jet. _J. Aerosol Sci._, 1999, **30**(7), 823-849.

53. R. P. A. Hartman, D. J. Brunner, D. M. A. Camelot, J. C. M. Marijnissen, and B. Scarlett. Jet break-up in electrohydrodynamic atomization in the cone-jet mode. _J. Aerosol Sci._, 2000, **31**(1), 65-95.

54. C. J. Hogan and P. Biswas. Porous Film Deposition by Electrohydrodynamic Atomization of Nanoparticle Sols. _Aerosol Sci. Tech._, 2008, **42**(1), 75-85.

55. A. Jaworek. Electrospray droplet sources for thin film deposition. _J. Mater. Sci._, 2007, **42**(1), 266-297.

56. K. Y. Li, H. H. Tu, and A. K. Ray. Charge limits on droplets during evaporation. _Langmuir_, 2005, **21**(9), 3786-3794.

57. L. Rayleigh. On the equilibrium of liquid conducting masses charged with electricity. _Philosophical Magazine_, 1882, **14**, 184-186.

58. J. N. Smith, R. C. Flagan, and J. L. Beauchamp. Droplet evaporation and discharge dynamics in electrospray ionization. _J. Phys. Chem. A_, 2002, **106**(42), 9957-9967.

59. B. A. Thomson and J. V. Iribarne. Field induced ion evaporation from liquid surfaces at atmospheric pressure. _J. Chem. Phys._, 1979, **71**, 4451- 4463.

60. M. Dole, L. L. Mack, R. L. Hines, R. C. Mobley, L. D. Ferguson, and M. B. Alice. Molecular beams of macroions. _J. Chem. Phys._, 1968, **49**(5), 2240 - 2249.

61. C. Hogan, _Charging, clustering, and fragmentation of nanoparticles and macromolecules in electrohydrodynamic atomization_, in _Department of Energy,_

*Environmental and Chemical Engineering*. 2008, Washington University in St. Louis: St. Louis. p. 282.

62. J. Suh, B. Han, K. Okuyama, and M. Choi. Highly charging of nanoparticles through electrospray of nanoparticle suspension. *J. Colloid. Interf. Sci.*, 2005, **287**(1), 135-140.

63. E. O. Knutson and K. T. Whitby. Aerosol classification by electric mobility: Apparatus, theory, and applications. *J. Aerosol Sci.*, 1975, **6**, 443-451.

64. N. A. Fuchs and A. G. Sutugin. 1970, Ann Arbor: Ann Arbor Science.

65. B. Y. H. Liu. 1976, New York: Academic Press.

66. H. Y. Wen, G. P. Reischl, and G. Kasper. Bipolar Diffusion Charging of Fibrous Aerosol-Particles .1. Charging Theory. *J. Aerosol Sci.*, 1984, **15**(2), 89-101.

67. K. T. Whitby, ed. B.Y.H. Liu, Elsevier, New York, 1976.

68. B. Y. H. Liu, D. Y. H. Pui, and B. Y. Lin. Aerosol Charge Neutralization by a Radioactive Alpha-Source. *Particle Characterization*, 1986, **3**(3), 111-116.

69. G. P. Reischl, J. M. Makela, R. Karch, and J. Necid. Bipolar charging of ultrafine particles in the size range below 10 nm. *J. Aerosol Sci.*, 1996, **27**(6), 931-949.

70. R. Flagan, in *Aerosol Measurement*, eds. P.A. Baron and K. Willeke, John Wiley & Sons, New Jersey, Second edn., 2001, pp. 537 - 568.

71. H. M. Lee, C. S. Kim, M. Shimada, and K. Okuyama. Effects of mobility changes and distribution of bipolar ions on aerosol nanoparticle diffusion charging. *J. Chem. Eng. Jpn.*, 2005, **38**(7), 486-496.

72. M. Shimada, B. W. Han, K. Okuyama, and Y. Otani. Bipolar charging of aerosol nanoparticles by a soft X-ray photoionizer. *J. Chem. Eng. Jpn.*, 2002, **35**(8), 786-793.

73. G. Bacher, W. W. Szymanski, S. L. Kaufman, P. Zollner, D. Blaas, and G. Allmaier. Charge-reduced nano electrospray ionization combined with differential mobility analysis of peptides, proteins, glycoproteins, noncovalent protein complexes and viruses. *J. Mass Spectrom.*, 2001, **36**(9), 1038-1052.

74. M. Fujimoto, T. Kado, W. Takashima, K. Kaneto, and S. Hayase. Dye-sensitized solar cells fabricated by electrospray coating using TiO2 nanocrystal dispersion solution. *J. Electrochem. Soc.*, 2006, **153**(5), A826-A829.

75. S. N. Jayasinghe, A. N. Qureshi, and P. A. M. Eagles. Electrohydrodynamic jet processing: An advanced electric-field-driven jetting phenomenon for processing living cells. *Small*, 2006, **2**(2), 216-219.

76. Y. Kashiwa, Y. Yoshida, and S. Hayase. All-metal-electrode-type dye sensitized solar cells (transparent conductive oxide-less dye sensitized solar cell) consisting of thick and porous Ti electrode with straight pores. *Appl. Phys. Lett.*, 2008, **92**(3), 033308.

# Chapter 2: Soft X-Ray Charger (SXC) System for Use With

# Electrospray for Mobility Measurement of Bioparticles

**2.1 Abstract**

Electrospray size spectrometry analysis (ESSA) is a simple mobility based aerosol technique to characterize the size and charge state of nanometer-sized particles because it does not require special sample preparation.  The analysis can be carried out online and in real-time, and it requires a minimal sample volume, typically less than 0.1 mL. Particularly crucial for ESSA is the use of a neutralizer to bring the multiply charged particles, generated by the electrospray, to the Boltzmann equilibrium charge distribution for further size measurement. A typical ESSA setup uses a Po-210 neutralizer that has a short half-life time and its radioactive nature raises serious safety concerns that translate into practical disadvantages.  In the present study, a soft X-ray charger (SXC) was demonstrated to be effective in the neutralization of multiply charged nano- and bio-particles.  Calculations showed that photoionization with the SXC generated a bipolar ion number concentration in the neutralization chamber one and two orders of magnitude higher than the Po-210 and Kr-85 neutralizers, respectively. Additionally, it was established that photoionization may be effectively and safely implemented in ESSA and the results of this study provide support for the further development of a SXC that may be incorporated into an electrospray aerosol generation system.

**2.2 Introduction**

With the emergence of nano-bio hybrid systems constructed with novel nanometer-sized biological particles such as viruses, proteins, or natural complexes[1, 2], it is essential to develop safer and practical measurement techniques that do not need complex sample preparation procedures and allow for a precise on-line characterization based on particle size and charge. The size, shape, and charge of particles, for instance, influence the deposition mechanism (diffusion, impaction, or sedimentation) and therefore also influence the deposition location of particles in the human respiratory tract.[3] Electrospray size spectrometry analysis (ESSA) is an aerosol technique that provides information of the particle size and the charge state of various particle types (i.e. solid particles and biological particles) in the submicrometer and nanometer-size ranges.[4-7] Its relative simplicity and the fact that the analysis is carried out online and in real-time make ESSA an attractive method for the online identification of proteins and viruses.[1, 4-7] In ESSA, highly charged, monodispersed aerosol particles are generated by an electrospray, which are then exposed to a bipolar ion environment to reduce their number of charges to the Boltzmann's equilibrium charge-state, where theoretically most of them carry zero or one (positive or negative) charge. Subsequently, the size of the singly charged particles is obtained on the basis of their electrical mobility, which is inversely proportional to particle size and directly proportional to particle charge.[8] Several studies have demonstrated the applicability of ESSA to tasks requiring benign handling and transport of biological or otherwise fragile particles such as identifying specific proteins within a protein mixture[4, 5, 7], characterizing giga- and megadalton complexes[6], studying the size and morphology of carbon nanotubes[9], and measuring

the size of light-harvesting chlorosomes[1]. To generate the neutralizing bipolar ion environment, a typical configuration of an ESSA setup uses a Po-210 diffusion neutralizer, which is an α-particle emitter (i.e. radioactive). Note that emitters that generate bipolar ions are used as neutralizers when applied to charged particles, and as chargers when applied to neutral particles, and in both cases the mechanism involves collisions of ions with the particles being analyzed. While Po-210 has been demonstrated to be effective in neutralizing electrosprayed particles, there are three main concerns about its applicability. One being the safety concern, because of its chemical nature, a Po-210 sources needs special handling to avoid radioactive exposure and contamination (requiring significant protocols for acquiring the source). The second issue is its short half-life time (120 days) that requires frequent replacement. An alternative to solve the short half-life time constraint of Po-210 is to use a Kr-85 source, a β-particle emitter, which has a half-life of 10.8 years. However, in previous studies the bipolar ion generation rate of a Kr-85 charger was found to be one order of magnitude smaller than the Po-210,[10] which significantly affects the accuracy of the ESSA. Moreover, the particles' attainment of the equilibrium charge-state with a Kr-85 charger was found to be dependent on the residence time in the charger (i.e. the carrier gas flow rate) and it was achieved only at longer residence time[10], as compared to a Po-210 source. The third concern is particle loss, in the case of nanoparticles, due to ineffective removal of the charge. The number of charges on electrosprayed particles scales with the square of particle diameter and the probability of ion collision with a particle decreases with decreasing particle size; this probability is particularly low for nanoparticles, where the gas mean free path is larger than the size of the particles. For instance, in the case of

neutral particles, the fraction of particles that acquire a single charge by diffusion is much smaller than the fraction of particles carrying no charge. Similarly, for initially charged nanoparticles, the opposite phenomenon occurs and only a small fraction of them carry no charge.

A potential alternative to the Po-210 neutralizer is to use photoionization with a soft X-ray charger (SXC) device. A SXC has several practical advantages over conventional diffusion neutralizers. For instance, with the SXC direct photoionization of carrier gas molecules and of aerosol particles (by photoemission of a surface electron) occurs simultaneously resulting in the generation of a high number of positive and negative ions with nearly equal number concentration, this in turn may enhance the particle neutralization efficiency by diffusion.[11-13] In addition, the SXC can generate bipolar ions at a rate one order of magnitude higher than a-ray emitters; the ion generation can be readily controlled by turning the device on and off, thus it does not require special handling; and it does not need to be replaced frequently.[13] In a nanoparticle charging model that accounted for simultaneous photoionization and diffusion charging, Jiang et al[11, 14] demonstrated that the photoionization yield coefficient, the parameter that governs photoionization charging, depends only on particle size, while the ion attachment coefficient, which governs the diffusion charging mechanism, depends on both the particle size and the initial charge-state. Thus, photoionization may be more effective to neutralize multiply charged particles of a given size.

Previous SXC studies, however, focused on using photoionization to charge particles and collect them using electric fields[12, 15, 16] or to investigate the achievement of the equilibrium charge-state of aerosol particles with low charge-state.[13, 17, 18] To the best of

our knowledge, photoionization with a SXC has never been applied to neutralize (i.e. reduce the charge-state) highly charged particles generated by an electrospray, where the number of charges carried by particles scales with the square of particle size.[19] In the present study, the application of a SXC to ESSA of polystyrene latex (PSL) particles, bacteriophage MS2, and ovalbumin (OVA) protein is reported. PSL particles are routinely used as standards for size calibration in various instruments. MS2 is commonly used as a surrogate of biothreat viruses[20], its nucleic acid sequence and crystal structure are well-characterized, and it has a size in the range of 24 - 27 nm, depending on the characterization technique[6, 20-23]. Ovalbumin is a protein with a size of approximately 6 nm, it has been studied by high-performance liquid chromatography with inductively coupled plasma mass spectrometric detection[24], and has been employed in animal inhalation studies. Moreover, PSL, MS2, and OVA particles have been characterized using the electrospray and electrical mobility-based techniques, thus they are suitable to demonstrate the functioning of a SXC in ESSA.

## 2.3 Experimental Section

### 2.3.1 Materials

Standard polystyrene latex (PSL) particles of 60 nm in diameter were purchased from Duke Scientific and diluted in deionized water to a concentration of 13 vol %. Bacteriophage MS2 (ATCC 15597-B1) was propagated as described previously[25]. Following propagation, phage suspensions were concentrated and purified using an Amicon Centriplus YM-10 filtration device (Millipore Corp., Bedford, MA). Suspensions were centrifuged at 3000 x g for 8 min, and then washed in 20 mM ammonium acetate to

dilute out impurities.  This process was repeated three times to sufficiently concentrate and purify the phage suspensions.  An ovalbumin (OVA, Sigma-Aldrich) solution of 0.005 wt % was prepared in 20 mM ammonium acetate.

### 2.3.2 Diffusion Neutralizers

An aerosol diffusion neutralizer typically consists of a radioactive source that emits $\alpha$ or $\beta$ particles that, upon collision with the molecules of the carrier gas, generate a bipolar ion environment. The bipolar ions then collide with the aerosol particles, resulting in, depending on their polarity, an increase or a reduction of the number of charges on the particles. In the present study, Po-210 ($\alpha$-particle emitter, 0.5 mCi, TSI) and Kr-85 ($\beta$-particle emitter, 2 mCi, TSI) sources were used as diffusion neutralizers. Po-210 sources are commonly used to bring highly charged particles to an equilibrium charging state in ESSA.[4-6, 22] The Po-210 and Kr-85 sources used in this study were 4 months-old and 9 years-old, respectively.

### 2.3.3 Photoionizer

The SXC device (Hamamatsu Photonics Ltd., Japan, Model L7113) used in this study operates with an input potential of 12 V and generates X-rays with an intensity of 3.5 - 9.5 keV and wavelength of 0.12 - 0.41 nm, from a circular beryllium window of approximately 1.5 cm in diameter. A detailed description of the SXC can be found in previous publications from our group and other authors[12, 13, 15, 18] .

2.3.4 Characterization of Particle Size

**Table 2-1:** Experimental plan to compare the performance of a SXC with diffusion neutralizers.

| Test | Electrospray system | Capillary inner diameter [μm] | Charger | Neutralization chamber volume [m$^3$] | Objective |
|------|---------------------|-------------------------------|---------|----------------------------------------|-----------|
| 1 | | | Po-210 | | To compare the efficacy of a SXC with the commonly used Po-210 charger in electrospray size spectrometry, using a well-characterized commercial setup. |
| | EAG | 40 | | $2.8 \times 10^{-5}$ | |
| 2 | | | SXC | | |
| 3 | | | Kr-85 | $10 \times 10^{-5}$ | To compare the efficacy of a SXC with that of a Kr-85 charger in electrospray size spectrometry. |
| | In-house | 160 | | | |
| 4 | | | SXC | $1.3 \times 10^{-5}$ | |

The experimental plan is summarized in Table 2-1. In a first set of experiments, a commercial electrospray aerosol generator (EAG, Model 3480, TSI Inc.), with a capillary inner diameter of 40 μm, was operated in the cone-jet mode to aerosolize suspensions of PSL particles, bacteriophage MS2, and OVA as depicted in Figure 2-1(a). The EAG uses a total gas flow rate of 1.1 L min$^{-1}$ (i.e. 1.0 L min$^{-1}$ air + 0.1 L min$^{-1}$ CO$_2$) to carry the highly charged aerosol particles from the electrospray zone to a neutralization chamber. The neutralization chamber has a circular window on one side where a Po-210 neutralizer of 2.5 cm in diameter (active area = 1.5 cm) is inserted. Following charge neutralization, aerosol particles were sent to a scanning mobility particle sizer (SMPS) system to measure their particle size distribution. The SMPS is composed of an electrostatic

classifier, a differential mobility analyzer (DMA, TSI Inc., Models 3081 and 3085), and an ultrafine condensation particle counter (UCPC, TSI Inc., 3025A). Briefly, the functioning of the DMA is depicted in Figure 2-1(a); singly charged particles are introduced from the top of the instrument at a volumetric flow rate $Q_a$, the voltage in the central electrode of the DMA increases gradually, with each voltage value corresponding to a certain particle electrical mobility.
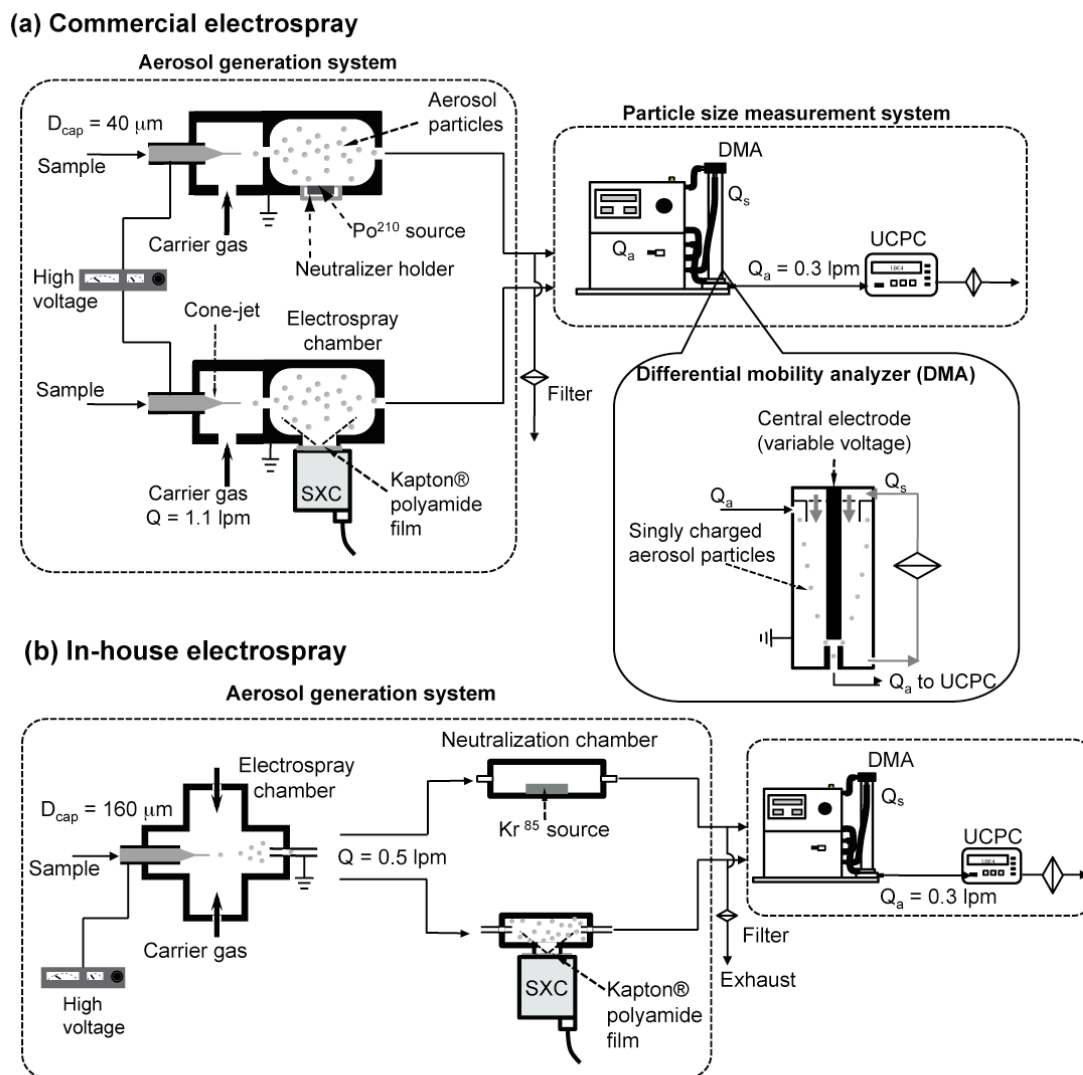


**Figure 2-1:** Experimental setup for size spectrometry, (a) commercial electrospray setup and (b) in-house electrospray setup.

As particles move down, only particles with the right electrical mobility, at a given voltage, pass through the slit at the bottom of the DMA and are sent to the UCPC to be counted using optical methods. The rest of the particles are carried away by the sheath flow $Q_s$. A more detailed description of the DMA and the electrical mobility theory can be found elsewhere[8]. Note that the electrostatic classifier in the SMPS has a Kr-85 neutralizer built-in; however, in all the experiments it was bypassed to evaluate only the performance of the bipolar ion generators upstream in the neutralization chamber. Bypass of the Kr-85 in the SMPS did not have any significant effect in the particle size distribution. Initially, experiments were carried out using the Po-210 source incorporated in the EAG (Test 1), then the Po-210 source was removed and replaced with the SXC device, which was then attached to the chamber window, and the same set of experiments were conducted (Test 2). In the case of the SXC, a thin polyamide film (Kapton[TM] 30HN, DuPont Corp., 30 mm thick) was used to seal the circular window where the Po-210 source is usually inserted and to protect the X-ray emitter surface from the aerosol flow as well as to keep the neutralization chamber airtight[12, 16].

In a third set of experiments, measurements were carried out in an in-house electrospray system with the Kr-85 source as shown in Figure 2-1(b) (Test 3). The setup configuration had to be changed (compared to Tests 1 and 2) because of the cylindrical shape of the Kr-85 neutralization chamber. For these experiments, the suspensions were fed with a syringe pump, at a flow rate of 0.5 mL min$^{-1}$, through a tapered stainless steel capillary needle of 160 mm inner diameter. The capillary was set inside a closed chamber through which particle-free $CO_2$ carrier gas was sent at a rate of 0.5 L min$^{-1}$. The highly charged particles were then passed through the neutralization chamber containing a Kr-85

source. Subsequently, charge-reduced electrosprayed particles were sent to the SMPS

system. In the last set of experiments (Test 4) the Kr-85 charger in the in-house

electrospray system was replaced with a soft X-ray neutralization chamber as shown in

Figure 2-1(b) and the same measurements were carried out.


## 2.4 Results and Discussion

The efficacy of a bipolar neutralizer in reducing the number of charges on an

electrosprayed particle depends on the number concentration of bipolar ions generated by

the neutralizer, the residence time of the particle in the neutralization chamber, and the

particle size.[10-13, 17, 26, 27] Table 2-2 summarizes the ion number concentration[12, 13]

generated by each charger for the specific neutralization chamber volume calculated

with:

$$n_i = \left[ \frac{I_s}{\alpha e V} \right]^{\frac{1}{2}}$$ 
(1)

In expression (1), $I_s$ is the saturation current, $\alpha$ is the recombination constant for bipolar

ions (1.6 x $10^{-12}$ m$^3$ s$^{-1}$), $e$ is the electron elementary charge (1.6 x $10^{-19}$ C), and $V$ is the

volume of the neutralization chamber. Note that ion concentrations in Table 2-2 are ideal

values since the calculations do not account for wall deposition losses. The maximum

energy of $\alpha$ and $\beta$ particles is 5.3 MeV and 0.695 MeV, respectively,[10] three orders of

magnitude higher than the photon energy of the soft X-rays (9.5 keV). However, the

bipolar ion number concentration generated with the SXC is one and two orders of

magnitude higher than the Po-210 and the Kr-85 neutralizers, respectively. Similar results

were reported in charging studies comparing a SXC and an $\alpha$-ray emitter (Am-241)

source by Shimada et al.[13] Because the number of charges carried by electrosprayed particles is known to scale with the square of the particle size[19] and because the probability of a particle colliding with an ion decreases with decreasing particle size, a high ion number concentration is desired to increase the ion-particle collision probability and to effectively bring the particle charging state to the Boltzmann charge distribution over the entire size range. Furthermore, Liu et al[27] reported that the saturation current (i.e. the ion number concentration) of a Po-210 neutralizer decreases with increasing source age. For instance, the $I_s$ of a 4 month-old Po-210 neutralizer was approximately 15 nA and it dropped to 7 nA and 0.7 nA after 8 and 24 months, respectively.[27] Thus, the values of $I_s$ in Table 2-2 represent the best-case scenario for the Po-210 neutralizer in this study. Conversely, the SXC is known to have uniform saturation current during its lifetime, and generate bipolar ions with nearly the same electrical mobility.[13] Note that a better comparison of the neutralizers' performance would be based on the product $n_i t$, where $t$ is the particles' residence time in the charger. However, since the neutralization chamber volume and the carrier gas flow rate were constant (i.e., constant residence time) for both the SXC and Po-210 charger the performance depended only on the ion number concentration in the neutralization chamber, which was higher in the case of the SXC. After comparing the ion number concentration generated by each neutralizer, experiments were carried out to verify the actual performance of each neutralizer with electrosprayed particles of different characteristics.

**Table 2-2:** Calculated ion number concentration for each charger.

| Charger | Saturation current, $I_s$ [A][a] | Ion concentration, $n_i$ [# m$^{-3}$] | Ion production rate, S [# m$^{-3}$ s$^{-1}$] |
|---|---|---|---|
| Soft X-ray (EAG) | 1.5 x 10$^{-7}$ | 1.4 x 10$^{14}$ | 3.35 x 10$^{16}$ |
| Soft X-ray (In-house) | | 2.1 x 10$^{14}$ | 7.23 x 10$^{16}$ |
| Po-210 (EAG) | 2.0 x 10$^{-8}$ | 5.3 x 10$^{13}$ | 4.5 x 10$^{15}$ |
| Kr-85 (In-house) | 1.5 x 10$^{-9}$ | 7.6 x 10$^{12}$ | 9.4 x 10$^{13}$ |

[a] The $I_s$ of the SXC was provided by manufacturer, and for the diffusion chargers the value was taken from Liu et al.[27]
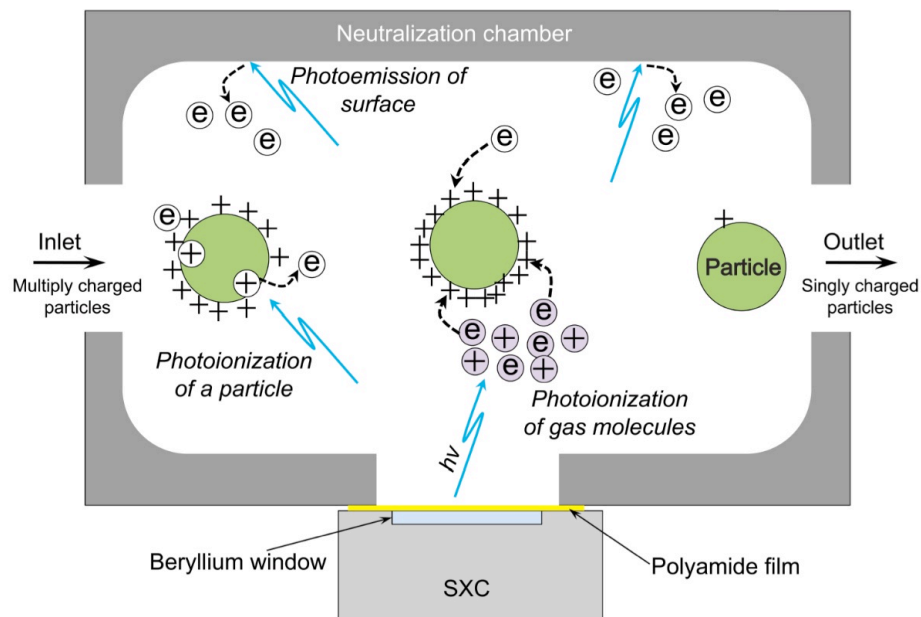


**Figure 2-2:** Mechanism of photoionization of highly charged electrosprayed particles.

The charge neutralization mechanism of electrosprayed particles using photoionization is depicted in Figure 2-2. Nanoparticles, entering the neutralization chamber, were multiply charged as a result of the electrospray, and the average number of elementary charges, $q$, carried by each particle is summarized in Table 2-3.

**Table 2-3:** Total number concentration measured at the outlet of the electrospray system.

| Particle | Number of charges acquired by electrospray, $q^b$ | Measured average total number concentration [# cm$^{-3}$] | | Particle loss$^c$ [%] |
| --- | --- | --- | --- | --- |
| | | SXC | Po-210 | |
| PSL (60 nm) | 674 | 8.66 x 10$^4$ | 5.03 x 10$^4$ | 41.9 |
| MS2 (24.1 nm) | 114 | 9.59 x 10$^4$ | 8.37 x 10$^4$ | 12.7 |
| OVA (6.38 nm) | 8 | 2.70 x 10$^5$ | 2.08 x 10$^5$ | 23.0 |

$^b$ $q = 0.23D_p^{1.95}$, from Suh et al.[19]   $^c$With respect to the SXC and calculated with 100 x ([SXC]-[Po-210])/[SXC].

In the chamber, an equal number of bipolar ions are generated with a SXC by three mechanisms, namely, direct photoionization of particles, photoionization of carrier gas molecules, and photoemission of the chamber wall. The bipolar ions then collide randomly with the highly charged particles leaving zero or one charge by the so-called diffusion neutralization mechanism (i.e. the same mechanism as diffusion charging) that results from the Brownian motion of the ions and particles.

2.4.1 SXC and Po-210 Charger

Particle size distribution measurements with the EAG are shown in Figure 2-3 for the SXC and the Po-210 source. Note that for both neutralizers (Tests 1 and 2) the neutralization chamber volume and the residence time in the chamber were constant, however the ion number concentration was higher with the SXC (see Table 2-2). Electrospray of 60 nm PSL particles neutralized with the SXC and with Po-210 resulted in a peak mobility diameter of 63 nm in both cases (Figure 2-3(a)). Nevertheless, the particle number concentration at 63 nm had a two-fold increase with the SXC compared

to the Po-210 neutralizer, and because the size distribution was unimodal, it can be inferred that the 60 nm PSL particles selected with the DMA carried only one charge. The particle size distribution of MS2 phages, shown in Figure 2-3(b), with both the SXC and the Po-210 neutralizer resulted in a narrow mode diameter at 24.1 nm, in excellent agreement with previous size spectrometry reports.[6, 23, 28] Such a value is slightly smaller than the reported size of 27.5 nm using X-ray crystallography.[21] However, the discrepancy was attributed to the MS2 phage encapsulating water molecules in the X-ray crystallographic studies and undergoing compression in the electrosprayed droplet.[6, 21] The narrow peak showed that a major fraction of the MS2 phages carried +1 charge. Figure 3(c) shows the particle size distribution of electrosprayed OVA particles, after neutralization with the SXC and with the Po-210 source. The particle size distribution shows three peaks at 6.38 nm, 7.91 nm, and 8.82 nm that correspond to monomers, dimers, and trimers, respectively carrying +1 charge, in very good agreement with previous reports[7].

These results indicate that photoionization with the SXC was sufficient to bring a larger fraction of nanoparticles to the equilibrium charge-state (zero or one charge), compared to particles neutralized with the Po-210 source, independent of the particles' initial charge-state. It also means that photoionization with the SXC reduced the particle loss by deposition onto system walls as can be observed in Figures 2-3 and 2-4. This fact was verified by measuring the total particle number concentration at the output of the commercial electrospray and the results are summarized in Table 2-3. The difference in total particle number concentration was attributed to a larger fraction of particles carrying zero or one charge with the SXC, compared to the Po-210 neutralizer. The multiply

charged particles exiting the Po-210 neutralizer would have higher electrical mobility, and consequently tend to deposit at shorter distances without reaching the DMA slit or the CPC.

The parameters that govern the charging mechanisms by photoionization and by diffusion are the photoelectric yield coefficient and the ion attachment coefficient, respectively. The photoelectric yield coefficient depends only on particle size, even for very small particles, because the photon energy of soft X-rays ($\sim 7.4 \times 10^{-16}$ J) is much greater than the work function of most uncharged materials.
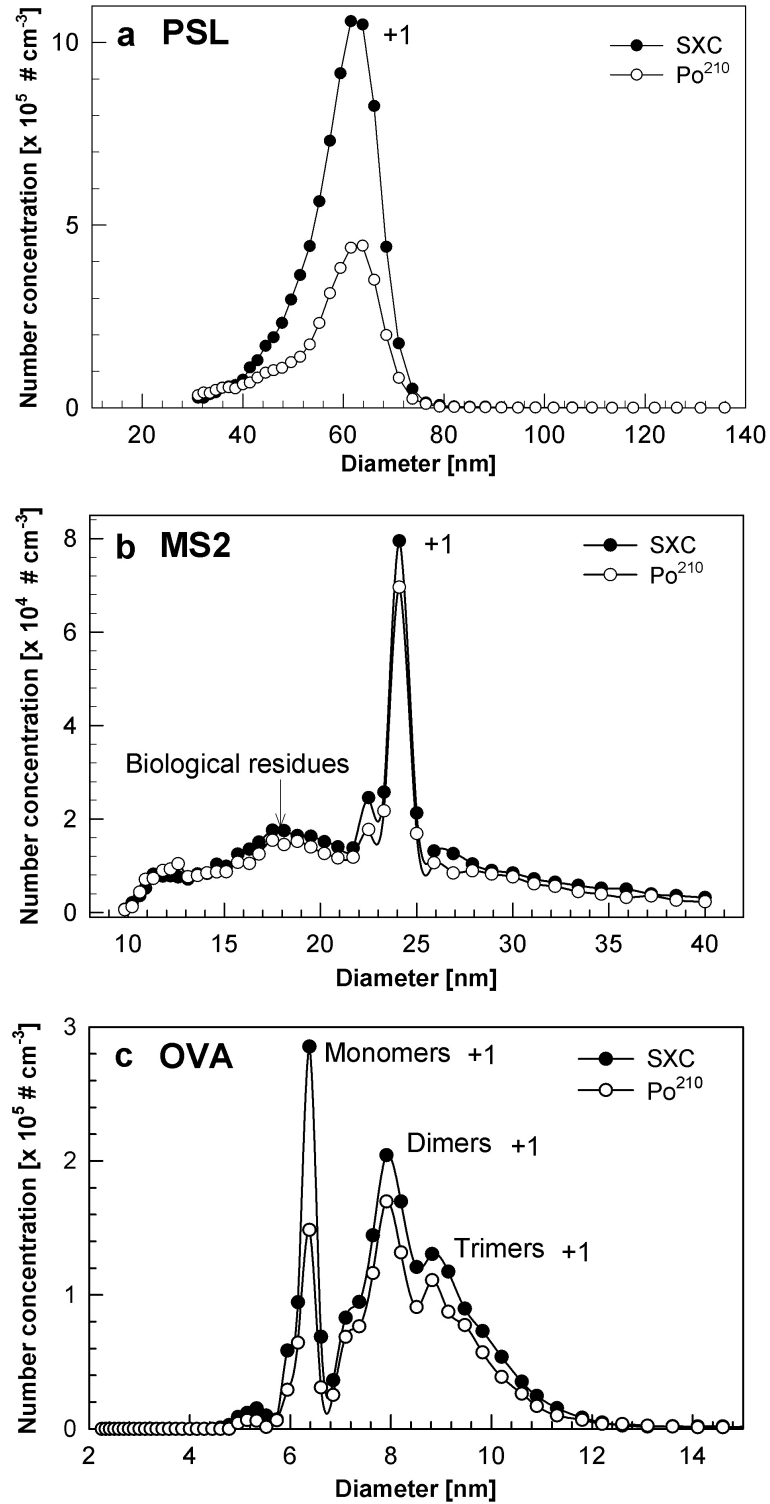
**Figure 2-3:** Particle size distribution of (a) 60 nm PSL particles, (b) bacteriophage MS2, and (c) OVA obtained with a SXC and a Po-210 charger in a commercial electrospray setup.

On the contrary, the ion attachment coefficient depends on both the particle size and the initial charge state of the particle, and its value decreases as the number of charges on a particle increases.[11] In a charging model that accounts for simultaneous diffusion charging and photoionization charging mechanisms Jiang et al[11] established that the energy flux from the charger plays a key role in defining which mechanism is dominant. The energy flux was defined in terms of $K_cI$, where $K_c$ is a material dependent empirical constant and $I$ is the irradiation intensity in J m$^{-2}$ s$^{-1}$. Because $K_c$ is not available in the literature for most materials Jiang et al[11] used a range of $K_cI$ values in their model. They found that if the product $K_cI < 10^{31}$ J m$^{-2}$ s$^{-1}$ diffusion charging is dominant, conversely if $K_cI > 10^{33}$ J m$^{-2}$ s$^{-1}$ photoionization charging is dominant. In the present study; however, both charging mechanisms were investigated separately, thus an energy flux threshold for which each mechanism is dominant could not be established. Note that in case of the SXC diffusion charging (i.e., diffusion neutralization) also takes place after the carrier gas molecules have been directly photoionized (see Figure 2-2). Furthermore, in the case of highly charged particles, the work function depends not only on the bulk properties of the particles, which govern the electrochemical potential, but also on the state of its surface layer, which influences the potential difference between the particles and the gas media. In addition, although the electrosprayed particles are positively and highly charged, the photon energy of the soft X-rays is high enough to eject electrons out of their surface layer. The maximum charge level a sphere can acquire by photoionization before the process reaches a saturation point is given by Equation (2)[26]:

$$q_{max} = \frac{4\pi\varepsilon_0}{e^2}\left(hv - \Phi_\infty\right)r - \frac{3}{8} \tag{2}$$

Where $\varepsilon_0$ is the permittivity of vacuum (8.85 x $10^{-12}$ $C^2$ $N^{-1}$ $m^{-2}$), *hv* is the photon energy (7.4 x $10^{-16}$ J), $\Phi_{\circ}$ is the work function of the particle material, and *r* is the particle radius. Based on expression (2), estimates of the maximum number of charges that 6.31 nm, 24.1 nm, and 60 nm particles acquire by photoionization with the SXC are 10071, 38465, and 95763 respectively. These values are much greater than the Gaussian limit of the particles (i.e. the critical point at which a charged solid particle becomes unstable), implying that upon charging with direct photoionization, multiply charged particles with positive polarity become a sink for negative ions, making it reasonable to assume that these particles reach the Boltzmann equilibrium charge distribution instantaneously, thereby resulting in enhancement of the diffusion neutralization rates.

### 2.4.2 SXC and Kr-85 Charger

These sets of experiments were conducted with the aim of providing ancillary results on the efficacy of the SXC as a neutralizer; because it is known that a Kr-85 neutralizer is not applicable to electrosprayed particles due to its strong dependence on gas flow rate.[10] Figure 2-4 shows the particle size distribution of (a) bacteriophage MS2 and (b) OVA particles aerosolized with the in-house system and neutralized with the SXC and with the Kr-85 charger.
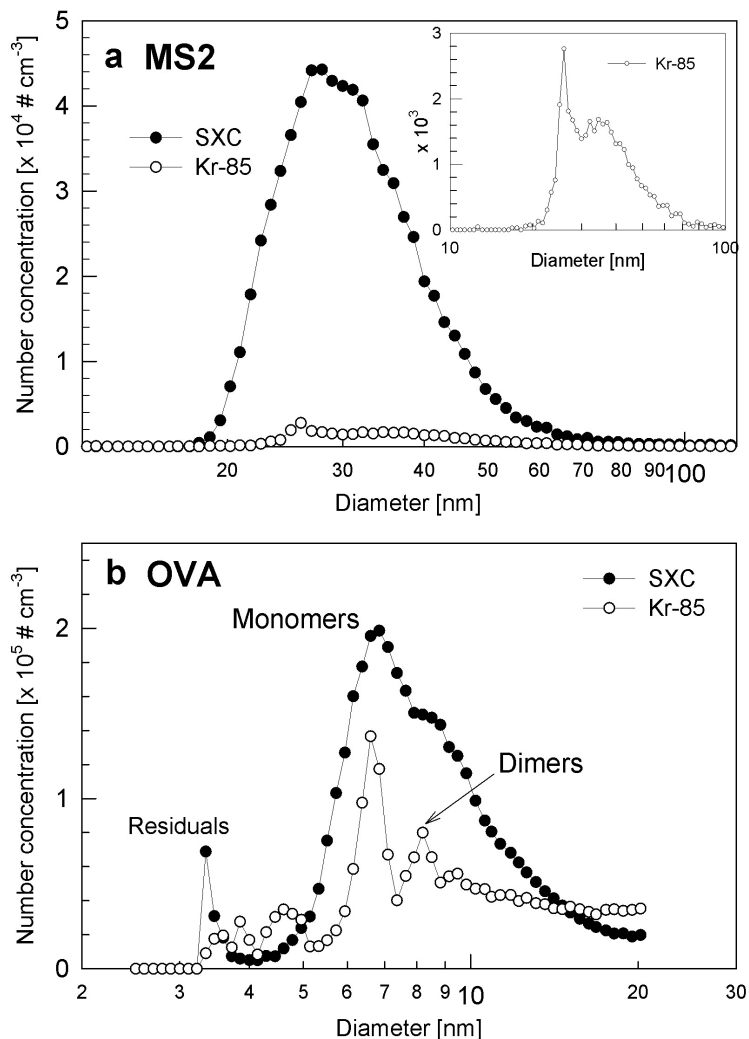
**Figure 2-4:** Particle size distribution of (a) bacteriophage MS2 and (b) OVA obtained with a SXC and a Kr-85 charger in an in-house electrospray setup.

The capillary diameter of the in-house electrospray system was three times larger than the EAG capillary. Thus, the initial droplet size was calculated to be approximately 3 μm. In the case of a larger droplet size, it is more probable that the droplet contained more than one particle resulting in a broader particle size distribution. Figure 2-4(a) shows the particle size distribution of MS2 phages, with a mode diameter of 26 nm, which is in the range of values found in literature for the size of MS2 phages[6, 21, 22, 28]. Note that this value is 2 nm larger than the one obtained with the EAG in this and previous studies[6, 23,

[28] and closer to the value reported by Golmohammadi et al[21] using x-ray crystallography, which may suggest that MS2 bacteriophages underwent less compression due to the larger droplet size generated in the in-house electrospray system compared to the EAG. For comparison, the particle size distribution obtained with the Kr-85 charger is shown in the inset in Figure 2-4(a). The particle number concentration after neutralization with the SXC was one order of magnitude higher than the value obtained with the Kr-85 charger. That large discrepancy may have arisen because the flow profile was sufficiently nonideal that most of the flow passed directly from the inlet to the outlet inside the neutralizer such that the actual residence time of a large fraction of the particles was much shorter than the calculated residence time for uniformly mixed flow. The particle size distribution of OVA, shown in Figure 2-4(b), shows the characteristic monomer and dimer peaks at 6.8 nm and 8.2 nm respectively. Again, note that the particle number concentration was higher with the SXC than with the Kr-85 charger.

## 2.5 Conclusions

Photoionization with a SXC was shown to be as effective in neutralizing multiply charged particles, in the nanometer size range, as the commonly used Po-210 diffusion neutralizer. With the SXC, direct photoionization of aerosol particles and gas molecules as well as Brownian diffusion of ions took place simultaneously, which enhanced the neutralization efficiency, thereby resulting in instantaneous achievement of the particles' Boltzmann charge distribution. Electrospray size spectrometry analysis of PSL, MS2 bacteriophages, and OVA particles neutralized with the SXC showed excellent agreement

with the radioactive Po-210 source used in the present and previous studies. Total number concentration measurements showed that photoionization with the SXC was sufficient to bring highly charged particles to the equilibrium charge state and reduced particle losses. When compared against a Kr-85 β-ray emitter in an in-house electrospray system, the SXC resulted in higher particle number concentration for the two particles tested, due to both the higher ion number concentration generated with the SXC and the Kr-85 performance's dependence on the carrier gas flow rate. Although, the Po-210 neutralizer is broadly used in ESSA, the results of this study demonstrate that it can be replaced with a safer and more controllable technology such as photoionization with soft X-rays. Nevertheless, an improved SXC design that could be incorporated into an EAG needs to be further investigated.

## 2.6 References

[1] L. B. Modesto-Lopez, A. M. Collins, R. E. Blankenship, and P. Biswas. Electrospray-assisted characterization and deposition of chlorosomes to fabricate a light-harvesting biomimetic device. *Energy Environ. Sci.*, 2010, **3**, 216-222.

[2] C. B. Mao, D. J. Solis, B. D. Reiss, S. T. Kottmann, R. Y. Sweeney, A. Hayhurst, G. Georgiou, B. Iverson, and A. M. Belcher. Virus-based toolkit for the directed synthesis of magnetic and semiconducting nanowires. *Science*, 2004, **303**(5655), 213-217.

[3] A. Gomez. The electrospray and its application to targeted drug delivery. *Respir. Care*, 2002, **47**(12), 1419-1431.

[4] G. Allmaier, C. Laschober, and W. Szymanski. Nano ES GEMMA and PDMA, new
    tools for the analysis of nanobioparticles—protein complexes, lipoparticles, and
    viruses. *J. Am. Soc. Mass Spectr.*, 2008, **19**(8), 1062-1068.

[5] G. Bacher, W. W. Szymanski, S. L. Kaufman, P. Zollner, D. Blaas, and G. Allmaier.
    Charge-reduced nano electrospray ionization combined with differential mobility
    analysis of peptides, proteins, glycoproteins, noncovalent protein complexes and
    viruses. *J. Mass. Spectrom.*, 2001, **36**(9), 1038-1052.

[6] C. J. Hogan, E. M. Kettleson, B. Ramaswami, D. R. Chen, and P. Biswas. Charge
    reduced electrospray size spectrometry of mega- and gigadalton complexes:
    Whole viruses and virus fragments. *Anal. Chem.*, 2006, **78**(3), 844-852.

[7] S. L. Kaufman. Analysis of biomolecules using electrospray and nanoparticle
    methods: The gas-phase electrophoretic mobility analyzer (GEMMA). *J. Aerosol
    Sci.*, 1998, **29**(5/6), 537-552.

[8] E. O. Knutson and K. T. Whitby. Aerosol classification by electric mobility:
    Apparatus, theory, and applications. *J. Aerosol Sci.*, 1975, **6**, 443-451.

[9] B. Ku and P. Kulkarni. Morphology of single-wall carbon nanotube aggregates
    generated by electrospray of aqueous suspensions. *J. Nanopart. Res.*, 2008, 1-11.

[10] J. H. Ji, G. N. Bae, and J. Hwang. Characteristics of aerosol charge neutralizers for
    highly charged particles. *J. Aerosol Sci.*, 2004, **35**(11), 1347-1358.

[11] J. Jiang, M. H. Lee, and P. Biswas. Model for nanoparticle charging by diffusion,
    direct photoionization, and thermionization mechanisms. *J. Electrostat.*, 2007,
    **65**(4), 209-220.

[12] P. Kulkarni, N. Namiki, Y. Otani, and P. Biswas. Charging of particles in unipolar coronas irradiated by in-situ soft X-rays: enhancement of capture efficiency of ultrafine particles. *J. Aerosol Sci.*, 2002, **33**(9), 1279-1296.

[13] M. Shimada, B. W. Han, K. Okuyama, and Y. Otani. Bipolar charging of aerosol nanoparticles by a soft X-ray photoionizer. *J. Chem. Eng. Jpn.*, 2002, **35**(8), 786-793.

[14] J. Jiang, J. C. J. Hogan, D.-R. Chen, and P. Biswas. Aerosol charging and capture in the nanoparticle size range (6-15 nm) by direct photoionization and diffusion mechanisms. *J. Appl. Phys.*, 2007, **102**(3), 034904-034907.

[15] C. J. Hogan, M. H. Lee, and P. Biswas. Capture of viral particles in soft X-ray-enhanced corona systems: Charge distribution and transport characteristics. *Aerosol Sci. Tech.*, 2004, **38**(5), 475-486.

[16] E. M. Kettleson, B. Ramaswami, C. J. Hogan, M. H. Lee, G. A. Statyukha, P. Biswas, and L. T. Angenent. Airborne virus capture and inactivation by an electrostatic particle collector. *Environ. Sci. Technol.*, 2009, **43**(15), 5940-5946.

[17] B. W. Han, M. Shimada, K. Okuyama, and M. Choi. Classification of monodisperse aerosol particles using an adjustable soft X-ray charger. *Powder Technol.*, 2003, **135**, 336-344.

[18] H. Lee, C. Kim, M. Shimada, and K. Okuyama. Bipolar diffusion charging for aerosol nanoparticle measurement using a soft X-ray charger. *J. Aerosol Sci.*, 2005, **36**(7), 813-829.

[19] J. Suh, B. Han, K. Okuyama, and M. Choi. Highly charging of nanoparticles through electrospray of nanoparticle suspension. *J. Colloid Interf. Sci.*, 2005, **287**(1), 135-140.

[20] J. H. Thomas, S. K. Kim, P. J. Hesketh, H. B. Halsall, and W. R. Heineman. Bead-based electrochemical immunoassay for bacteriophage MS2. *Anal. Chem.*, 2004, **76**(10), 2700-2707.

[21] R. Golmohammadi, K. Valegård, K. Fridborg, and L. Liljas. The refined structure of bacteriophage MS2 at 2.8 A resolution. *J. Mol. Biol.*, 1993, **234**(3), 620.

[22] C. S. Kaddis, S. H. Lomeli, S. Yin, B. Berhane, M. I. Apostol, V. A. Kickhoefer, L. H. Rome, and J. A. Loo. Sizing large proteins and protein complexes by electrospray ionization mass spectrometry and ion mobility. *J. Am. Soc. Mass Spectr.*, 2007, **18**(7), 1206-1216.

[23] J. Thomas, B. Bothner, J. Traina, W. H. Benner, and G. Siuzdak. Electrospray ion mobility spectrometry of intact viruses. *Spectrosc.-Int. J.*, 2004, **18**(1), 31-36.

[24] K. Takatera and T. Watanabe. Determination of sulfhydryl-groups in ovalbumin by high-performance liquid-chromatography with inductively-coupled plasma-mass spectrometric detection. *Anal. Chem.*, 1993, **65**(24), 3644-3646.

[25] C. Hogan, E. Kettleson, M. Lee, B. Ramaswami, L. Angenent, and P. Biswas. Sampling methodologies and dosage assessment techniques for submicrometre and ultrafine virus aerosol particles. *J. Appl. Microbiol.*, 2005, **99**(6), 1422-1434.

[26] E. Hontanon and F. E. Kruis. Single charging of nanoparticles by UV photoionization at high flow rates. *Aerosol Sci. Tech.*, 2008, **42**(4), 310-323.

[27] B. Liu, D. Pui, and B. Lin. Aerosol charge neutralization by a radioactive alpha-source. *Part. Part. Syst. Char.*, 1986, **3**(3), 111-116.

[28] R. M. Eninger, C. J. Hogan, P. Biswas, A. Adhikari, T. Reponen, and S. A. Grinshpun. Electrospray versus Nebulization for Aerosolization and Filter Testing with Bacteriophage Particles. *Aerosol Sci. Tech.*, 2009, **43**(4), 298-304.

# Chapter 3: Role of the Effective Electrical Conductivity of Nanosuspensions in the Generation of TiO$_2$ Agglomerates with Electrospray

**3.1 Abstract**

Suspensions with varying volume fraction of TiO$_2$ nanoparticles and ionic strength were electrosprayed to obtain agglomerates of different characteristics, which were then deposited to produce films with tailored morphology, thickness, and porosity. The role of the nanoparticle volume fraction in both the effective electrical conductivity of TiO$_2$ nanosuspensions and the control of the size of agglomerates produced by electrospray was investigated. A simple modified equation for the effective electrical conductivity of TiO$_2$ nanoparticle suspensions was derived. The equation, which accounted for the diffuse ionic layer surrounding the nanoparticles and the agglomeration in a liquid, showed that the effective electrical conductivity is not only a function of the liquid and the particle conductivities, and the particle volume fraction but also a function of both the thickness of the adsorbed ionic layer on the particles and the particle size. Gradual increase of the number of particles in the suspension resulted in an increase in the suspension's effective electrical conductivity, when the initial liquid conductivity was in the range of 10$^{-4}$ to 10$^{-3}$ S m$^{-1}$. When the liquid conductivity was in the range of 10$^{-3}$ to 10$^{-2}$ S m$^{-1}$, however, addition of particles did not have any significant effect on the effective electrical conductivity. Control over the size of the TiO$_2$ nanoparticle agglomerates was achieved by electrospraying suspensions with liquid electrical conductivity of the order of 10$^{-3}$ S m$^{-1}$ and by varying particles volume fraction in the suspension. Electrospray deposition of suspensions with TiO$_2$ volume fraction = 0.04 % resulted in a more compact film with lower porosity and showed better water-splitting performance.

**3.2 Introduction**

Nanostructured thin films have a wide range of applications as photocatalysts, sensors, and solar cells because of their improved catalytic, electrical, optical, and mechanical properties. During film synthesis by aerosol routes, resulting film properties and film morphology are strongly dependent on the size and morphology of the depositing particles (Kulkarni & Biswas, 2003, 2004; Thimsen & Biswas, 2007). For instance, the total surface area and thickness of the film are two key parameters that evolve with changes in the size and morphology of the particles forming the film. For a constant film thickness, deposition of single spherical particles would result in a more dense film, whereas deposition of agglomerates would give a more porous film with larger surface area (Madler *et al*., 2006; Thimsen & Biswas, 2007). The desired thickness and surface area are dependent of the specific application. Consequently, precise control over the particle size and morphology during film fabrication is needed to engineer the preferred film properties.

Electrosprays, operating in the cone-jet mode (D.-R. Chen & Pui, 1997; Cloupeau & Prunet-Foch, 1994; de la Mora & Loscertales, 1994; Hartman *et al*., 1999) allow the generation of monodisperse droplets in the submicrometer range (Hogan & Biswas, 2008b; Lenggoro *et al*., 2002), making it a useful tool for depositing uniform films (Jaworek & Sobczyk, 2008; Modesto-Lopez *et al*., 2009; Rietveld *et al*., 2006). In previous studies, electrospray was used to fabricate porous particulate films with large surface area by directly depositing presynthesized nanoparticles of TiO$_2$, Fe$_2$O$_3$, and ZnO suspended in a volatile liquid (C. H. Chen *et al*., 1999; Fujimoto *et al*., 2006; Hogan & Biswas, 2008b; Modesto-Lopez, et al., 2009). Hogan and Biswas (2008a) studied the

physical properties of porous particulate films produced by electrospraying zinc oxide nanoparticle sols using sequential Monte Carlo simulations. Their studies focused on the effect of the particle's concentration on film porosity and surface roughness, and they found that for given electrospray conditions a higher number concentration of particles in the precursor suspension would result in thicker films with higher film porosity. Previous studies, however, did not stress the control of the size of the sprayed primary particles or agglomerates, which is essential for tuning the film morphology. Scaling laws to calculate the jet diameter ($D_j$), the mother droplet size ($D_D$), and the emitted current from the electrostatically produced spray have been proposed based on process parameters and liquid properties, namely electrical conductivity, viscosity, and dielectric constant. Among those, the electrical conductivity is the critical parameter affecting $D_j$ and $D_D$, and it plays an important role in the tangential stress in the motion inside Taylor cones (Barrero *et al.,* 1999). The scaling laws establish that the initial droplet size decreases with the increase in the electrical conductivity (D.-R. Chen & Pui, 1997; de la Mora & Loscertales, 1994; Ganan-Calvo *et al.*, 1997), although the equations generally refer to the solvent's electrical conductivity because the solutes used in earlier studies did not affect the solution's conductivity. However, literature reports indicate that when nanoparticles are dispersed in a liquid, the suspension's effective electrical conductivity varies with the volume fraction of particles. Such an effect is more remarkable when a poorly conductive liquid is used as solvent. In addition, the electrical conductivity of highly concentrated suspensions is used as an indicator of their stability and to determine the amount of solids suspended.

Maxwell's model for dilute dispersions relates the effective electrical conductivity of a suspension to the liquid and the particle conductivities and to the volume fraction of suspended particles (< 20 %), in which the fields surrounding each sphere do not disturb each other to any significant extent (Pavlin *et al.,* 2002). Furthermore, Maxwell's model is applicable only when the electrical conductivity of the continuous phase is sufficiently high. Recent experimental studies have demonstrated that the electrical conductivity of nanoparticle suspensions exhibit a different behavior from that of larger particles, and this phenomenon has been identified as an "anomalous" electrical conductivity of nanofluids (Chakraborty & Padhy, 2008; Cruz *et al.*, 2005; Fang & Zhang, 2005). These studies revealed that the diffuse ionic layer surrounding the nanoparticles play an important role in establishing the effective electrical conductivity.

The role of the electrical conductivity in the electrospray of pure liquids has been studied in the past. However, to the best of our knowledge there are no literature reports on the effective electrical conductivity of nanosuspensions of metal oxide semiconductors and its relationship to the electrospray process. More specifically, a direct investigation of the relationship between nanoparticle volume fraction and effective electrical conductivity, and their role during the agglomerate formation in the charged droplets generated by electrospray has not been performed. This work is focused on nanoparticles of metal oxide semiconductors because of their significant technological applications in pigments; in films for solar cells, sensors, and hydrogen generation by water-splitting; and in functional coatings among several others. Titanium dioxide was chosen as the test material because of its well-known photocatalytic properties and its broad applications in water-splitting films and dye-sensitized solar cells, in addition to its availability and

relatively low cost (Bach *et al*., 1998; Fujimoto, et al., 2006; Gratzel, 2004; Iskandar *et al*., 2007; Jiang *et al*., 2007; Modesto-Lopez *et al*., 2010; Pagliaro *et al*., 2009; Thimsen *et al*., 2008). The objective of the present work is to investigate the contribution of both the volume fraction of TiO$_2$ nanoparticles and the solvent's conductivity (or ionic strength) to the suspension's effective electrical conductivity. A modified Maxwell equation is proposed to explain the atypical behavior of the electrical conductivity observed in TiO$_2$ nanosuspensions. Agglomerates with tailored size and morphology were generated by electrospray and collected onto a grounded substrate to fabricate nanostructured films. The films, characteristics were investigated with a water-splitting system by measuring the hydrogen generation rate upon light activation.

## 3.3 Experimental Method and Calculations

The experimental test plan is summarized in Table 3-1. It can be divided in three main parts, the electrical conductivity measurements, the online real-time particle size distribution measurements, and the film deposition and watersplitting performance.

**Table 3-1:** Experimental plan of electrospray of TiO₂ nanoparticle suspensions. The solvent was a mixture of water : ethanol (1:9 vol).

| | **Experiment** | **Volume fraction of particles, $\phi_{p,v}$ [%]** | **HNO$_3$ conc. [mM]** | **Objective** |
|---|---|---|---|---|
| 1) | Electrical conductivity measurement | 0.002-0.400 | - | To study the effect of particle volume fraction on $K_{eff}$ (low electrical conductivity range). (Fig 3-2) |
| 2) | | 0.002-0.400 | 0.016 – 3.2 | To study the effect of the liquid electrical conductivity on $K_{eff}$. (Fig 3-2) <br><br> To find a point where $K_{eff}$ becomes nearly constant regardless of $\phi_{p,v}$. (Figs 3-2 & 3-3) |
| 3) | Particle size distribution measurement | 0.002-0.400 | 0.32 | At $K_{eff}$ on the order of $10^{-3}$ S m$^{-1}$ study the effect of particle volume fraction on the size of electrosprayed droplets (Fig. 3-4) and agglomerates (Fig 3-6). |
| 4) | | 0.002-0.400 | - | To compare the particle size distribution with that of suspensions in test 3) (Fig 3-7) |
| 5) | Film deposition | 0.04 – 0.40 | 0.32 | To study the effect of agglomerate size on film morphology and film properties. (Table 3-2) |

### 3.3.1 Preparation of TiO₂ Nanosuspensions

TiO₂ nanoparticles (Degussa P25) with a mean diameter $d_p$ = 26 nm (diameter given by manufacturer) were dispersed in a mixture of water and ethanol (1:9 v/v). There are two reasons for the selection of the chosen water to ethanol ratio: the first is to ensure complete evaporation of solvent after spraying; and the second is to keep the particles dispersed for a sufficient amount of time to carry out the experiments and prevent their settling (the addition of a small volume of water helps in the second case). When

suspensions with higher water to ethanol ratios were electrosprayed the cone-jet mode was not achieved because of the high surface tension of water. This resulted in the formation of a corona discharge at the capillary tip when a higher electric field was applied. The preparation method of suspensions consisted of adding the TiO$_2$ nanoparticles to 1 mL of deionized (DI) water, sonicating the mixture for 10 min, then adding 9 mL of ethanol, to give a total liquid volume ($V_L$) of 10 mL, and finally sonicating it for 20 min. Suspensions with a particle volume fraction, $\phi_{p,v}$, of 0.400 %, 0.200 %. 0.100 %, 0.040 %, 0.02 %, and 0.004% were prepared. The volume of the bulk particles, $V_p$, was obtained by dividing the mass of particles by the bulk density of the particles (4 g mL$^{-1}$). $\phi_{p,v}$ was calculated by dividing $V_p$ by the total volume of the suspension ($V_p + V_L$). The suspensions were stable for several hours after sonication, which allowed sufficient time to carry out measurements of electrical conductivity, agglomerate size, and film deposition experiments.

### 3.3.1.a. Electrical conductivity measurements of TiO$_2$ nanosuspensions

The effective electrical conductivity of the suspensions was measured with a digital conductivity meter (Dip cell, Pt plate surface, Model 1054, Amber Science Inc., OR, USA). To observe the effect of particle volume fraction at different electrical conductivities (ionic strengths), nitric acid (HNO$_3$) was added gradually to the suspensions to control the electrical conductivity. After the suspension preparation, the same volume of HNO$_3$ was added to each of them to obtain concentrations of 0.016, 0.032, 0.064, 0.120, 0.320, and 3.200 mM of acid. At each acid concentration increment, the electrical conductivity of the suspension was measured five times. When one set of

five measurements was completed, the acid concentration was increased and the procedure was repeated.

3.3.2 Electrospray of TiO$_2$ Nanosuspensions for Particle Size Distribution Measurements

A schematic diagram of the system used to electrospray TiO$_2$ nanoparticle suspensions and measure the size distribution of sprayed agglomerates is shown in Figure 3-1(a). A syringe pump (Pump 22, Harvard Apparatus, South Natick, MA, USA) was used to feed the suspension through a stainless steel capillary needle with an inner diameter of 160 μm at a flow rate of 1 μL min$^{-1}$. A high voltage power supply was connected to the capillary and a positive potential of > 4 kV was applied for cone-jet formation at the capillary outlet. For the size distribution measurements, the needle was set inside a closed chamber and particle-free air was introduced at a rate of 0.3 L min$^{-1}$. After the electrospray generation, the highly charged aerosol was passed through a bipolar neutralizer (Kr$^{85}$, TSI, 3077) to reduce the number of charges and bring them to an equilibrium state. The neutralizer was placed immediately after the chamber to minimize loss of particles by deposition onto system walls due to the electric field. However, the distance between the electrospray zone and neutralization zone was approximately 5 cm, sufficient for droplet break up. Mobility-based real time particle size distribution measurements were carried out using an electrostatic classifier (TSI, Model 3080) and a long differential mobility analyzer (TSI, Model 3081), coupled to a condensation particle counter (TSI, Model 3025A).

3.3.3 Electrospray-Deposition of Nanostructured TiO$_2$ Films

The setup used for the film deposition experiments is shown in Figure 3-1(b). TiO$_2$ suspensions of particle volume fractions of 0.40 %, 0.20 %, 0.10 %, and 0.04 % were electrosprayed. The deposition time was varied so that the same mass of particles (0.165 mg) was collected on the substrate. An indium tin oxide (ITO)-coated glass (Delta Technologies Limited, Stillwater, MN, USA) was used as the substrate and was positioned perpendicularly at a distance of 1.5 cm away from the capillary exit. The suspension flow rate was kept constant at 1 µL min$^{-1}$. The electrospray was always operated in the cone-jet mode and a digital optical microscope (QX5, Digital Blue, Atlanta, GA, USA) was used to monitor the cone-jet during deposition experiments. All deposition experiments were carried out in an atmospheric pressure environment. In an ancillary experiment, samples of the dried agglomerates were collected by inserting an electron microscopy grid in the central part of the spray plume for less than 5 s, followed by analysis with a scanning electron microscope (SEM; Model S-4500, Hitachi Ltd., Japan). Figure 3-1(c) explains the electrospray deposition process of TiO$_2$ nanoparticle suspensions. First, a particle suspension is fed mechanically through a capillary nozzle, and a high voltage is applied to the capillary. Because of that high voltage, charge separation occurs in the liquid with the ions of opposite charge to the polarity of the applied voltage moving towards the capillary walls, and the ions of the same polarity as the applied voltage moving towards the tip of the capillary. At some critical voltage, the liquid forms a conical shape at the tip, to increase its surface area, and emits a liquid jet that breaks into a highly charged droplet, commonly known as the mother droplet, hereafter referred only as D$_D$. When this droplet reaches its Rayleigh limit, it undergoes

droplet fissions, and it is through this mechanism that smaller progeny droplets are generated. As will be discussed in the following sections, depending on $K_L$ and $\phi_{p,v}$ single primary particles or particle agglomerates can be produced, thereby resulting in different film morphologies and film properties.
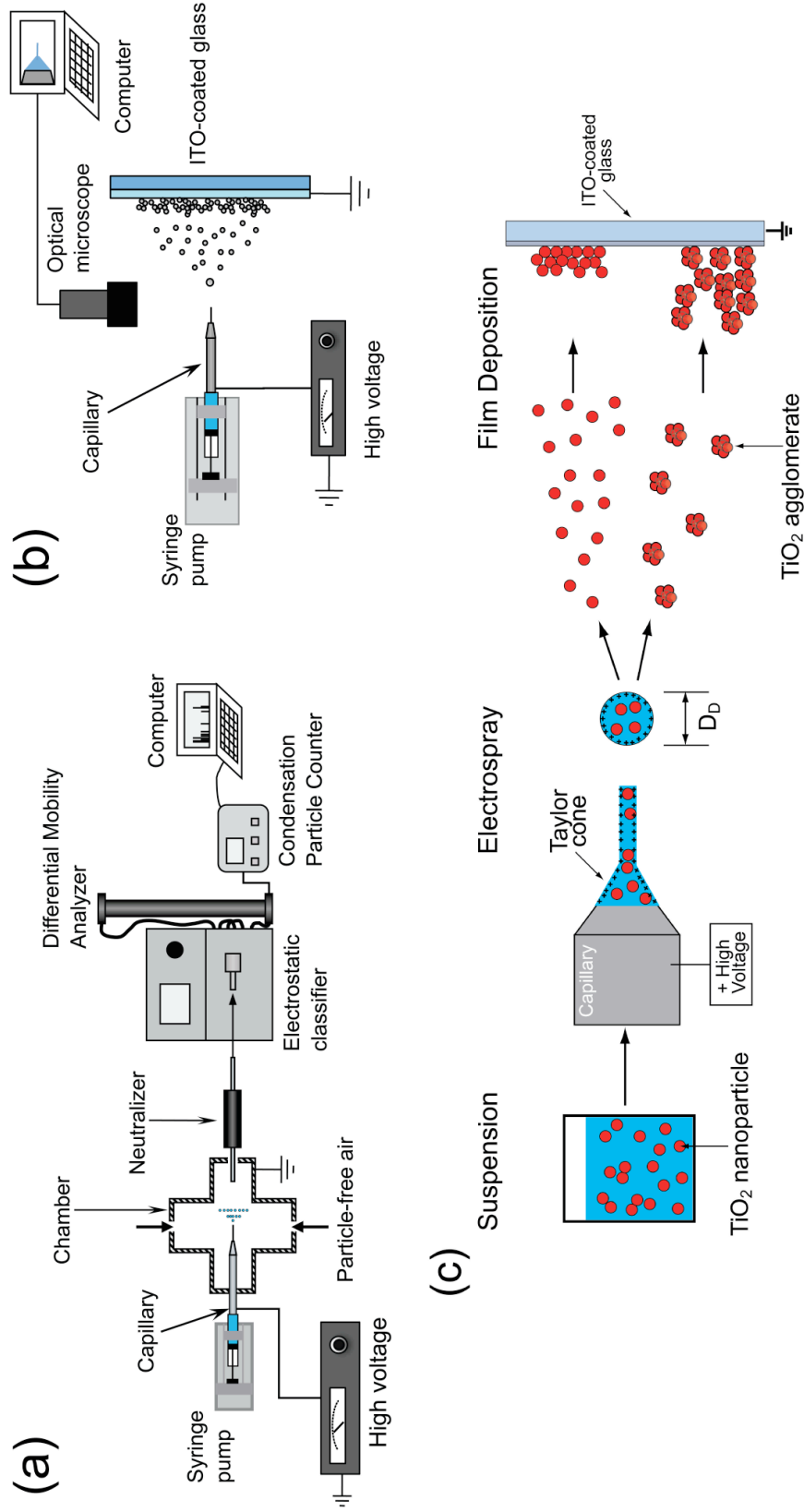
**Figure 3-1:** (a) Setup for electrospray and particle size measurement, (b) Setup for electrospray deposition of TiO$_2$ nanostuctured films, and (c) Illustration of the electrospray deposition process of TiO$_2$ nanoparticle suspensions.

*3.3.3.a. Film characterization*

Films were analyzed qualitatively with SEM and quantitatively using the air to particle volume ratio (APV) and film thickness. The APV is a parameter that is directly related to the film porosity, but it has the advantage that when represented in a linear scale the APV is more sensitive to changes in porosity for porosities close to unity (Hogan & Biswas, 2008b; Madler, et al., 2006). To calculate the APV of the electrospray-deposited TiO$_2$ nanostructured films, first the total volume of deposited particles ($V_{p,T}$) was determined by dividing the total deposited mass (0.165 mg) by the bulk density of the particles (4 g cm$^{-3}$); then the total volume of the film ($V_{film}$, volume of particles + volume of pores) was estimated from the average film height (from SEM images) and the total area of the film (1.8 cm$^2$). The APV is equal to ($V_{film} - V_{p,T}$)/$V_{p,T}$.

*3.3.3.b. Watersplitting experiments by light activation*

To further characterize the properties of the electrospray-deposited films, their watersplitting performance by light activation was measured. Sintering of the particles improves the electrical properties of the film by reducing the large number of grain boundaries and other defects located at particle-particle interfaces, which inhibit charge-carrier transport and promote recombination in a nanostructured film (Kulkarni & Biswas, 2003; Modesto-Lopez, et al., 2009; Thimsen, et al., 2008). In this work, electrospray deposited TiO$_2$ nanostructured films were post-annealed at 600 ºC for 3 h (Porter *et al.*, 1999) to improve their electrical properties by enhancing particle-particle contact due to neck formation. The watersplitting performance of the films was tested

using a standard 2-electrode photocell with a platinum wire counter electrode and 1 M

KOH electrolyte. The $TiO_2$ films were illuminated with a UV light ($\lambda < 400$ nm) from a

400 W Xe arc lamp (Oriel). The current through the external circuit, which is

proportional to the hydrogen production rate in the water-splitting system, was measured

using a multimeter (Keithley) and, normalized by the mass of the deposited $TiO_2$

particles. Details of the procedure and experimental setup for watersplitting performance

can be found elsewhere (Thimsen, et al., 2008).

### 3.3.4 Model Calculations

#### *3.3.4.a. Derivation of an effective electrical conductivity formula*

When particles are immersed in a liquid, they acquire certain number of surface

charges. These charges are the result of adsorption or desorption of ionic species in

solution. Ions of opposite charge to that of the particle's surface (counter ions) will be

attracted to it, causing the formation of an ionic layer around the particle. The Maxwell

expression has been used to estimate the effective electrical conductivity of suspensions

of uncharged particles with solids volume fraction less than 20 % (Cruz, et al., 2005;

Pavlin, et al., 2002; Wang *et al*., 2003):

$$K_{eff,M} = K_L \left( \frac{2K_L + K_p - 2(K_L - K_p)\phi_{p,v}}{2K_L + K_p + (K_L - K_p)\phi_{p,v}} \right) \qquad (1)$$

where, $K_{eff,\,M}$ is the effective electrical conductivity of the suspension from Maxwell

model, $K_L$ is the liquid electrical conductivity, $K_p$ is the bulk electrical conductivity of the

particles, and $\phi_{p,v}$ is the volume fraction of particles in the liquid. For poorly conductive

particles (as in the case of $TiO_2$ which has a $K_p = 10^{-11}$ S m$^{-1}$ (Beckenridge & Hosler, 1953)) equation (1) becomes a function of $K_L$ and $\phi_{p,v}$ only:

$$K_{eff} = 2K_L \left( \frac{1 - \phi_{p,v}}{2 + \phi_{p,v}} \right) \qquad\qquad (2)$$

The assumptions made in deriving Equations (1) and (2) impose certain constraints on its application. The Maxwell model is valid only when the suspended particles are well dispersed and do not interact with each other or when the electrical double layer surrounding the particles is very thin. Under such conditions, the conductivity becomes independent of the zeta potential. Experimental observations have shown that the net conductivity of poorly conductive particles in suspension may increase if the particles are heterogeneous, for example core-shell particles in which the core material has higher $K_p$ than the shell (Pavlin, et al., 2002). If the net conductivity of the heterogeneous particle increases, the effective conductivity of the suspensions will be increased provided that the suspending liquid has conductivity smaller than the particle. In such a case an equivalent conductivity of the particle needs to be considered, and therefore the Maxwell equation has to be modified to account for this increased equivalent conductivity of the particles. In the present work, the approach of Pavlin et al. (2002), for the conductivity of biological cells (a core-shell type of particles) was used to modify Equation (1). Upon dispersion of the $TiO_2$ particles in water, they are surrounded by an adsorbed monolayer of OH$^-$ ions from water, therefore they can be treated as core-shell type of particles. The core, a $TiO_2$ particle, has much lower conductivity than the shell, which is made of an adsorbed water monolayer. The thickness *t* of the adsorbed layer can be obtained from the Langmuir formula for monolayer adsorption (Wang, et al., 2003):

$$t = \frac{1}{\sqrt{3}} \left( \frac{4M_L}{\rho_L N_A} \right)^{1/3} \tag{3}$$

In equation (3), $M_L$ is the molecular weight of the adsorbed liquid (water), $\rho_L$ is the density of the liquid, and $N_A$ is Avogadro's number. In this work, t was calculated to be 0.285 nm for water. Since the adsorbed monolayer moves along with the particle in solution, we need to consider a corrected particle diameter $d_p^* = 25.6$ nm ($d_p^* = d_p + 2t$). The volume occupied by the adsorbed monolayer ($v_{ad}$) on a TiO₂ particle is:

$$v_{ad} = \frac{\pi}{6} \left( d_p^{*3} - d_p^3 \right) \tag{4}$$

The only ionic species present in solution are OH⁻ and H⁺ ions, and since the TiO₂ surface acquires positive charge in a polar solvent (Widegren & Bergstrom, 2002), as a first approximation the adsorbed monolayer can be assumed to be made of OH⁻ ions. It is the adsorption of these ionic species that modifies the local effective conductivity of the particle, resulting in its enhancement. As a result, in further calculations, the conductivity of the particle, $K_p$, needs to be modified by an effective particle conductivity, $K_{c,p}$, which accounts for the effect of the adsorbed ions. This newly defined effective conductivity of the particles can be calculated using Maxwell's expression (Equation (1)) (Cruz, et al., 2005; Pavlin, et al., 2002; Wang, et al., 2003):

$$K_{c,p} = K_{ad} \left( \frac{\left( K_p + 2K_{ad} \right) + 2A^3 \left( K_p - K_{ad} \right)}{\left( K_p + 2K_{ad} \right) - A^3 \left( K_p - K_{ad} \right)} \right) \tag{5}$$

In equation (5), $A^3$ and $K_{ad}$ are the volume fraction of particles in the TiO₂-monolayer composite and the electrical conductivity of the adsorbed ions, respectively. At the TiO₂-monolayer interface, it is difficult to know $K_{ad}$, but for an estimate the equivalent

conductivity at infinite dilution of OH⁻ ions, $\lambda^o_{OH^-}$ = 198 S cm² mol⁻¹ (Rossum, 1975), is

used. Therefore, A and $K_{ad}$ are given by equations (6) and (7) respectively:

$$A = \frac{a}{t + a} \,,$$

(6)

$$K_{ad} = \frac{\lambda^o_{OH^-}}{v_{ad} N_A} \,,$$

(7)

where $a$ is the TiO₂ particle radius (13 nm). The problem of calculating an effective

electrical conductivity of nanosuspensions could be approached similarly to that of the

thermal conductivity as proposed by Wang et al. (2003). Following their procedure,

besides the adsorbed monolayer of ions on the TiO₂ particle, another factor that

potentially contributes to the enhancement of the effective electrical conductivity of

nanoscale TiO₂ colloidal suspensions with low ionic strength is the formation of

pathways due to agglomeration. A lognormal distribution function n(r), can be used to

describe the probability that an agglomerate in the liquid has a mean radius $r$ (Wang, et

al., 2003):

$$n(r) = \frac{1}{r\sqrt{2\pi}\,\ln\sigma}\exp\left\{-\left(\frac{\ln(r/r_g)}{\sqrt{2\pi}\,\ln\sigma}\right)^2\right\}$$

(8)

In equation (8), $r_g$ is the geometric mean particle radius (12.5 nm, $r_g = a$), and σ is the

geometric standard deviation (approximately 1.4). In a manner similar to Wang et al

(2003), using Equations (1) and (8), and replacing $K_p$, $a$, and $\phi_{p,v}$ by $K_{c,p}$, $(a+t)$, and

$[(a+t)/a]^3\phi_{p,v}$ respectively; a modified equation for the effective electrical conductivity of

suspensions containing nonconductive particles in a liquid of low ionic strength,

simultaneously undergoing agglomeration is obtained:

$$K_{eff,2} = \frac{1 + \left(K_{c,p}K^* - 1\right)A^{-3}\phi_{p,v}}{1 + \left(K_L K^* - 1\right)A^{-3}\phi_{p,v}}$$

(9)

where,

$$K^* = 3n(r)r\big/(K_{c,p} + 2K_L)$$

(10)

Equation (9) shows that the effective conductivity of a nanoscale colloidal suspension is not only a function of the liquid's conductivity and the volume fraction of nanoparticles, as initially described in Maxwell model, but also a function of the agglomerate size (or particle size) and the thickness of the adsorbed ionic layer onto the particles. Equation (9) was used in the theoretical calculations of K$_{eff}$ and droplet size. In Equation (9), the mean radius of the agglomerate (r) was set between 100 – 120 nm, from microscopy images of dried suspension samples.

### 3.3.4.b. Droplet size calculation

Once an accurate understanding of the effective electrical conductivity is obtained, the values can be used to determine the droplet size generated by the electrospray based on established scaling laws. de la Mora and Loscertales (1994) proposed an expression to calculate the droplet size based on process parameters and liquid properties, indicating that the droplet size varies inversely to the one-third power of the electrical conductivity of the liquid for highly conductive liquids at a given flow rate:

$$D_D = G(\kappa)\left(\kappa\varepsilon_0 Q\big/K_{eff}\right)^{1/3},$$

(11)

where $D_D$ is the droplet size, $\kappa$ is the liquid dielectric constant, Q is the liquid flow rate, $\varepsilon_0$ is the permittivity of vacuum, and $G(\kappa)$ is a function of the dielectric constant, which was determined by Chen and Pui (1997) to be:

$$G(\kappa) = -10.87\kappa^{-\frac{6}{5}} + 4.08\kappa^{-\frac{1}{3}}, \tag{12}$$

Ganan-Calvo and Barrero (1997) proposed a similar expression to calculate the droplet size produced by electrospraying liquids of sufficiently high electrical conductivity and viscosity, which is given by:

$$D_D = 6.646\kappa^{-\frac{1}{6}}\left(\kappa\varepsilon_0 Q/K_{eff}\right)^{\frac{1}{3}} \tag{13}$$

Other authors have developed expressions to calculate droplet size and resulting particle size of a solution containing strong and weak electrolytes in which the nature of the electrolyte strongly affects the electrical conductivity of the solution (Basak et al, 2007). Equations (10) and (12) physically mean that for a constant liquid flow rate, increasing the electrical conductivity of the liquid would result in a smaller droplet size when the electrospray is operated in the cone-jet mode. In calculating the experimental droplet size ($D_{D,exp}$) and the theoretical droplet size ($D_{D,theo}$) with expression (11), the measured conductivity $K_{eff,exp}$ and the modified Maxwell conductivity $K_{eff,2}$ (Equation (9)) were used.


### 3.3.4.c. Calculation of number of particles per agglomerate

The average number of particles per agglomerate $N_{p,agg}$, for electrosprayed suspensions with high $K_L$, was calculated from (Friedlander, 1977):

$$N_{p,agg} = A\left(\frac{R}{a}\right)^{D_f}$$ (14),

where $A$ is a proportionality constant of the order of unity, $R$ is the mean radius of the agglomerate obtained from particle size distribution measurements, $a$ is the primary particle radius, and $D_f$ is the fractal dimension. The value of $D_f = 3$ was used because the electrosprayed agglomerates were nearly spherical formed by ballistic particle-cluster agglomeration (Friedlander, 1977).

## 3.4 Results and Discussion

The electrospray process is highly sensitive to variations in the effective electrical conductivity of a suspension, as seen from the scaling laws in section 3.4.b When the electrospray is operated at constant liquid flow rate, controlling $K_{eff}$ allows tuning of the droplet size, thus controlling the final agglomerate size. In the following sections the effect of the nanoparticle volume fraction on $K_{eff}$ of suspensions with low and high liquid's conductivity (i.e. low and high ionic strength) will be discussed based on a simple modified Maxwell expression. Then the impact of the nanosuspensions' $K_{eff}$ on the calculated droplet size and on the resulting agglomerate size and morphology will be discussed. Finally, effect of the agglomerate size on the performance of water-splitting films will be investigated.

### 3.4.1 Effective Electrical Conductivity ($K_{eff}$) Measurements and Modified Equation

The electrical conductivity of nanoparticle suspensions is a very complex phenomenon involving interparticle interactions as well as their associated kinetics (i.e.

kinetics of particle agglomeration and ion diffusion), thickness of the electrical double layer, competition between ion adsorption and desorption; and it still remains poorly understood. The following discussion attempts to provide some insight into this problem, specifically its relation to the electrospray process parameters.

The measured effective electrical conductivity as a function of volume fraction of particles is shown in Figure 3-2 for various acid additions. Note that the isoelectric point (i.e., the point of zero surface charge) of TiO$_2$ is reported to be approximately 6.0 and the pH values corresponding to each acid addition were below 4.0. Furthermore, TiO$_2$ does not dissolve in HNO$_3$, hence dissolution of TiO$_2$ was out of consideration.
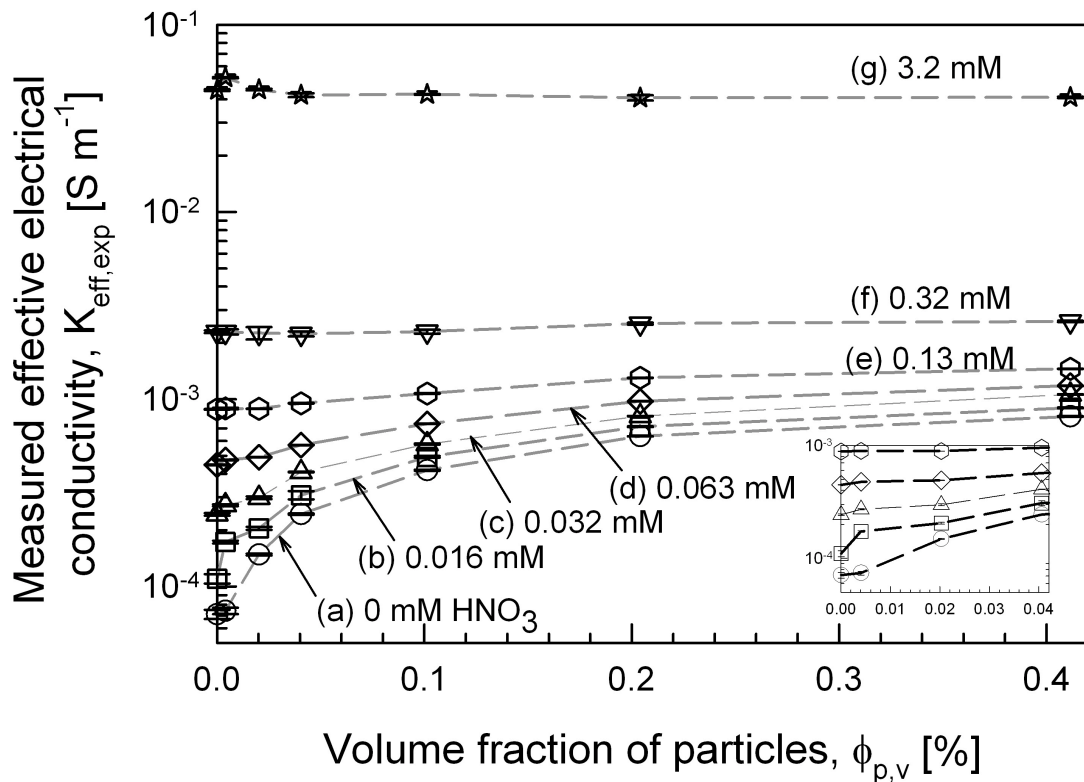


**Figure 3-2:** Effective electrical conductivity of TiO$_2$ nanosuspensions as a function of volume fraction of particles (a) without HNO$_3$, and with (b) 0.016 mM, (c) 0.032 mM, (d) 0.063 mM, (e) 0.13 mM, (f) 0.32 mM, and (g) 3.2 mM HNO$_3$.

For suspensions without, or with very dilute HNO$_3$ (K$_L$ = $10^{-4}$-$10^{-3}$ S m$^{-1}$), the effective electrical conductivity increased with increasing $\phi_{p,v}$. When K$_L$ was in the range $10^{-3}$- $10^{-2}$ S m$^{-1}$, the volume fraction of particles did not have any significant effect on the electrical conductivity of the suspension with K$_{eff}$ only increasing in magnitude with the addition of more HNO$_3$. Increasing the concentration of HNO$_3$ to 3.2 mM increased K$_L$ to >$10^{-2}$ S m$^{-1}$. In that range, conversely to the low K$_L$ range (K$_L$ = $10^{-4}$-$10^{-3}$ S m$^{-1}$), increasing $\phi_{p,v}$ resulted in a decrease in the suspension's electrical conductivity. The inset in Figure 3-2 shows the measured K$_{eff}$ for $\phi_{p,v}$ < 0.004 %; for the small range of $\phi_{p,v}$ it can be observed that K$_{eff}$ increases linearly with $\phi_{p,v}$, as would be predicted by Maxwell theory for conductive particles in a nonconductive solvent (K$_p$ >> K$_L$), which is not the case in the suspensions being studied. In the case of suspensions without acid addition (Curve (a) in Figure 3-2), it is noteworthy to point that even though the TiO$_2$ nanoparticles have very low conductivity, K$_{eff}$ increased about one order of magnitude with increasing $\phi_{p,v}$ from 0 % to 0.4 %. Given that the particles are insulators, one would expect a decrease in K$_{eff}$ with increasing $\phi_{p,v}$ (K$_p$ << K$_L$), as predicted by Maxwell theory. These observations clearly show that K$_L$, K$_p$, and $\phi_{p,v}$ are not the only parameters affecting K$_{eff}$. Our results of suspensions without acid (Figure 3-2, curve (a)) and with 3.2 mM HNO$_3$ (Figure 3-2, curve (g)) are in good agreement with literature reports for alumina particles in water (Cruz et al, 2005), and gold nanoparticles in toluene (Fang and Zhang, 2005). Cruz et al (2005) attributed the increase of K$_{eff}$ with increasing $\phi_{p,v}$, in suspensions with low ionic strength, to the alumina particles' attractive and repulsive interactions, they also reported that when NH$_4$Cl was added to the suspensions (High K$_L$), K$_{eff}$ decreased slightly with increasing $\phi_{p,v}$ (their data correspond to an HNO$_3$ concentration of 3.2 mM of this work).

They argued that because in such a high ionic strength the liquid has much higher conductivity than the particles; on increasing $\phi_{p,v}$ the volume of low conductive particles would increase, thereby resulting in a slight decrease of the effective conductivity. Similarly, Fang and Zhang (2005) reported that when highly conductive gold nanoparticles were dispersed in toluene, a nonopolar and non conductive solvent, $K_{eff}$ increased sharply from $\phi_{p,v} = 0$ % to some critical value, after which $K_{eff}$ increased steadily with increasing $\phi_{p,v}$. Fang and Zhang, however, attributed these phenomena to an increased number of conductive gold nanoparticles with increasing $\phi_{p,v}$ (meaning that the charges are being transported by conduction through the nanoparticles). In those two works, the particles had higher conductivity than the $TiO_2$ nanoparticles used in the present work. Since an increase in the $HNO_3$ concentration decreases the pH of the suspension and increases the number of dissociated species in the liquid, it is reasonable to think that these electrical conductivity phenomena are associated with the ionic double layer surrounding the particles (Cruz, et al., 2005; Janusz *et al.*, 1999; Widegren & Bergstrom, 2002). Thicker ionic layers promote the diffusion of counterions from the ionic layer to the bulk phase simultaneously increasing the counterions number concentration in the bulk. This, in turn, tends to enhance the effective electrical conductivity. Thicker ionic layers, however, may result in a reduced electrophoretic mobility, which tends to decrease the effective electrical conductivity. Additionally, increasing the concentration of $H^+$ may cause a reduction of the zeta potential, due to a compression of the electrical double layer with increasing ionic strength, which then results in the formation of agglomerates by coagulation (Widegren & Bergstrom, 2002). Moreover, the physical contact of particles in agglomerated networks provides new paths

for higher electrical conductivity. Conversely, rapid agglomeration of particles tends to decrease the nanosuspension's effective conductivity because of a reduction in the number density of the particles (Chakraborty & Padhy, 2008).

From our data in Figure 3-2, three regimes of effective electrical conductivity of the suspensions could be identified. In the first regime, because of the low ionic strength and thin electrical double layer, particle agglomeration as well as particle surface charge played a dominant role in the electrical conductivity process. In the second regime, increased liquid ionic strength reduced the agglomeration by thickening the electrical layer around the particles; this also increased the number of ions in the bulk liquid, and thus the effective electrical conductivity was independent of $\phi_{p,v}$. In the third regime, however, increase of the ionic strength caused the compression of the electrical double layer, due to stronger repulsions caused by the double layers of neighboring particles. A thinner electrical double layer in turn enhanced the agglomeration and particle settling processes simultaneously reducing the number density of suspended particles at higher $\phi_{p,v}$ values.

To explain the results, the simple expression (Equation (9)) to predict $K_{eff}$ of nanosuspensions accounting for particle agglomeration and for an ionic layer adsorbed on the particles' surface was used. Figure 3-3, shows the measured $K_{eff,exp}$ and the calculated $K_{eff,2}$ from Equation (9) as a function of $\phi_{p,v}$ for two limiting cases of low $K_L$ (0 mM HNO₃) and high $K_L$ (0.320 mM HNO₃), for comparison $K_{eff,M}$ from Equation (2) is also depicted in the plot. For both cases of $K_L$, Equation (9) fits our experimental data very well, in contrast with Maxwell expression. In successive calculations of theoretical droplet size, expression (9) was used to calculate the theoretical effective electrical

conductivity. The agreement between $K_{eff,exp}$ and $K_{eff,2}$ demonstrate that at low ionic strength particle agglomeration in the suspension play the dominant role in increasing $K_{eff}$ which is also enhanced by the ions adsorbed on the particles' surface, while at high ionic strength the number of ions dissociated in the solution dominate.
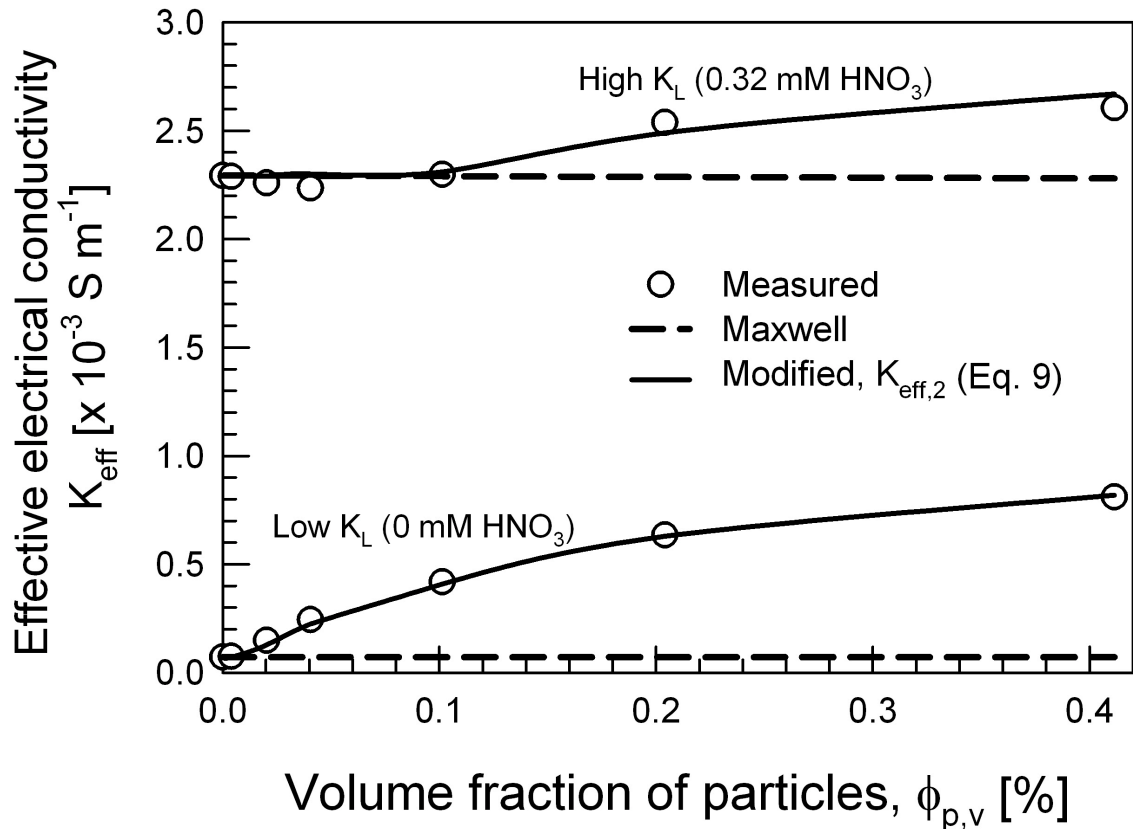


**Figure 3-3:** Comparison between the measured and the calculated effective electrical conductivities for two limiting cases of liquid with low and high $K_L$. The theoretical effective conductivities were calculated with Equations 2 (Maxwell's model for insulating particles) and 9 (modified Maxwell's model). The effect of surface charge of particles on $K_{eff}$ can be observed at low $K_L$.

To investigate the individual contributions of the two effects (i.e., particle ionic layer and agglomeration) incorporated in the modified expression (Equation 9)

calculations were performed accounting only for either the ionic layer effect or the agglomeration effect. The results are shown in Figure 3-4. It was found that at high $K_L$ the ionic layer effect was responsible for increasing the suspension's conductivity while the agglomeration effect of the particles was negligible. Conversely, at low $K_L$ the increase of the suspension's conductivity with $\phi_{p,v}$ resulted from a combination of both phenomena.
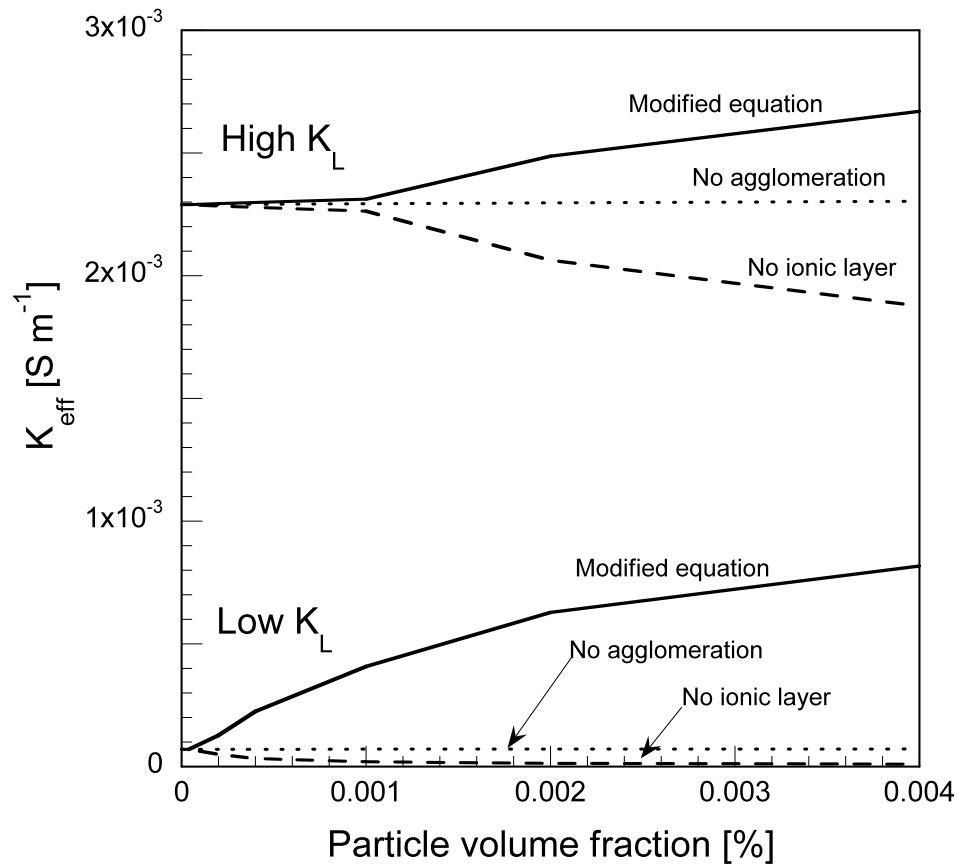


**Figure 3-4:** Contributions of the particle's EDL and agglomeration to the effective electrical conductivity of TiO₂ nanosuspensions (calculated with equation 9). Solid lines show the case when both effects are incorporated, dashed lines show the case when the ionic layer was neglected, and dotted lines show the case when the agglomeration was neglected.

*3.4.1.a. Droplet size ($D_D$)*

The surface charge of the particles during an electrospray process impacts the droplet size calculations. Figure 3-5 shows the calculated $D_D$, using the scaling laws (Equation (11)), as function of $\phi_{p,v}$, for two cases, when the solvent had low $K_L$ (no $HNO_3$ added) and high $K_L$ (0.32 mM $HNO_3$). In calculating $D_D$, the measured $K_{eff,exp}$, the theoretical conductivity from the modified Maxwell expression $K_{eff,2}$, and the $K_{eff,Maxwell}$ from Maxwell model were used. At high $K_L$, the experimental, the modified, and the Maxwell $K_{eff}$ resulted in a mother droplet with nearly constant size of about 1.4 µm independent of $\phi_{p,v}$.
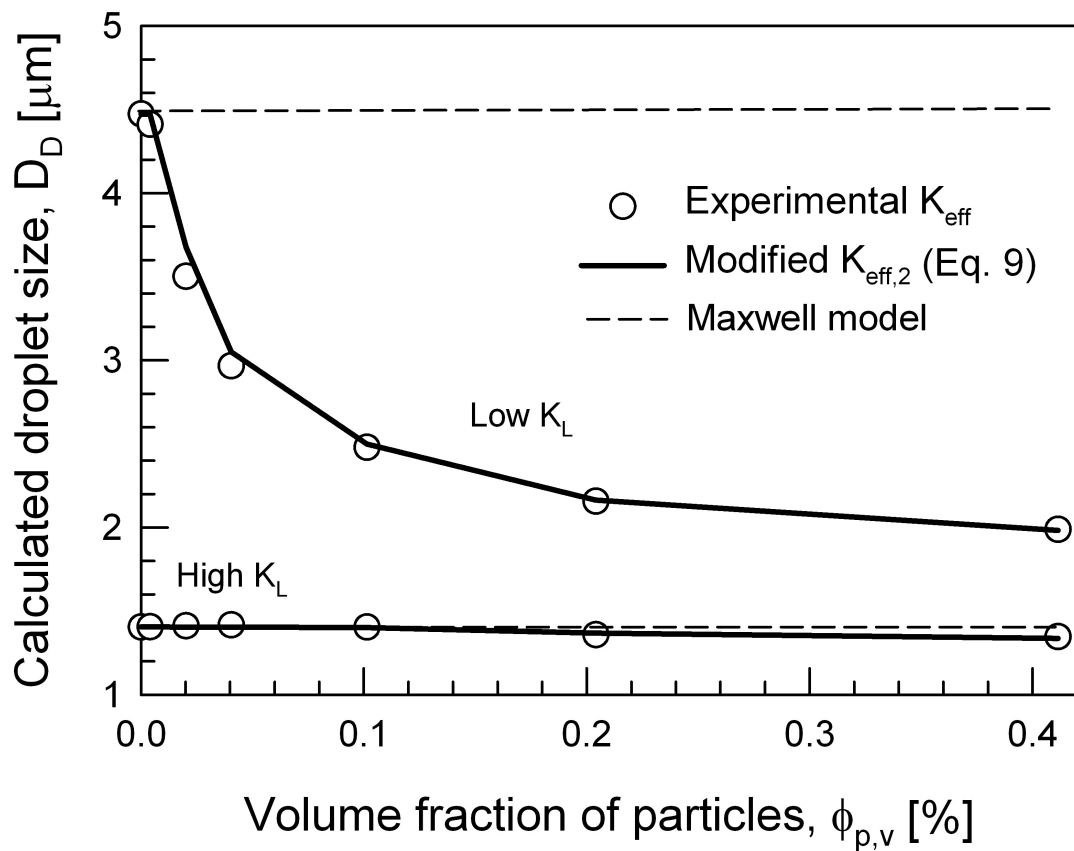


**Figure 3-5:** Droplet size calculations using equation (10) based on experimental $K_{eff}$ and theoretical $K_{eff}$ from equation (2), for the limiting cases of low and high $K_L$.

Although for particle volume fractions larger than 0.3 % the $D_D$ calculated with the Maxwell equation deviated slightly from the $D_D$ obtained with the experimental and the modified $K_{eff}$. At low $K_L$, however, two features related to the surface charge of the particles can be observed. First, the $D_D$ calculated with $K_{eff}$ from Maxwell model remains constant independently of $\phi_{p,v}$ introducing an error of more than 100 % in $D_D$ at $\phi_{p,v} = 0.4$ %. This large difference may have occurred because, as discussed in section 3.1, the Maxwell equation is based strictly on the liquid and the particles conductivities, and on the particles' volume fraction; it does not introduce corrections for the effect of the particles' surface charge and the agglomeration kinetics in the solvent. Second, the droplet sizes obtained from the experimental and modified $K_{eff}$ are in excellent agreement, and they decrease with increasing particle volume fraction in the suspension. The reason is that for a liquid with low $K_L$ (or low ionic strength) the effect of particle surface charge and particle agglomeration on the effective suspension's conductivity is dominant. Thus, increasing $\phi_{p,v}$ increases $K_{eff}$ and decreases $D_D$, from the scaling laws. Figure 3-5 also shows that when the nanosuspension has sufficiently high ionic strength (high $K_L$) the droplet size is independent of the volume fraction of particles, and thus the size of the electrosprayed agglomerates can be readily controlled by adjusting the $\phi_{p,v}$. Precise control of agglomerate size and morphology would allow for a precise control of the agglomerate transport characteristics and the resulting film properties. In the next section the relevance of controlling $D_D$ to generate agglomerates with tailored size and morphology will be addressed.

*3.4.1.b. Particle size distribution measurements*

As discussed in section 4.1, in the electrospray process the electrical conductivity plays a key role in controlling $D_D$. For suspensions with high liquid conductivity, a constant $D_D$ could be readily obtained and the effects of the particles surface charge on the droplet formation dynamics could be suppressed allowing for a relatively simple control of agglomerate size and shape. Conversely, for suspensions with low liquid conductivity, precise control of agglomerate size may not be possible because the droplet size increases with increasing $\phi_{p,v}$. To establish how $K_L$ and $\phi_{p,v}$ may affect the resulting agglomerate size, online particle size distribution measurements were performed. Figure 3-6 shows the particle size distribution of electrosprayed TiO$_2$ nanoparticle suspensions of various $\phi_{p,v}$ of (a) 0.004 %, (b) 0.020 %, (c) 0.040 %, (d) 0.100 %, (e) 0.200 %, and (f) 0.400 % with a constant HNO$_3$ concentration of 0.32 mM (High $K_L$ = 2.3 x 10$^{-3}$ S m$^{-1}$, see Figure 3-3). Thus all the electrosprayed suspensions produced a constant droplet size of 1.4 μm (High $K_L$ in Figure 3-5). A sharp, unimodal peak was obtained by electrospraying the most dilute suspension ($\phi_{p,v}$ = 0.004 %). The measured geometric mean mobility diameter of 26 nm, with a geometric standard deviation of 1.16, was close to the mean primary particle size, indicating that the condition of one-particle per droplet was met (Lenggoro, et al., 2002). In the case of the suspension with $\phi_{p,v}$ = 0.020 % a trimodal distribution was observed, with the first peak corresponding to the primary particle size, while the second and third peaks, around 60 and 100 nm, to doublets and triplets, respectively.
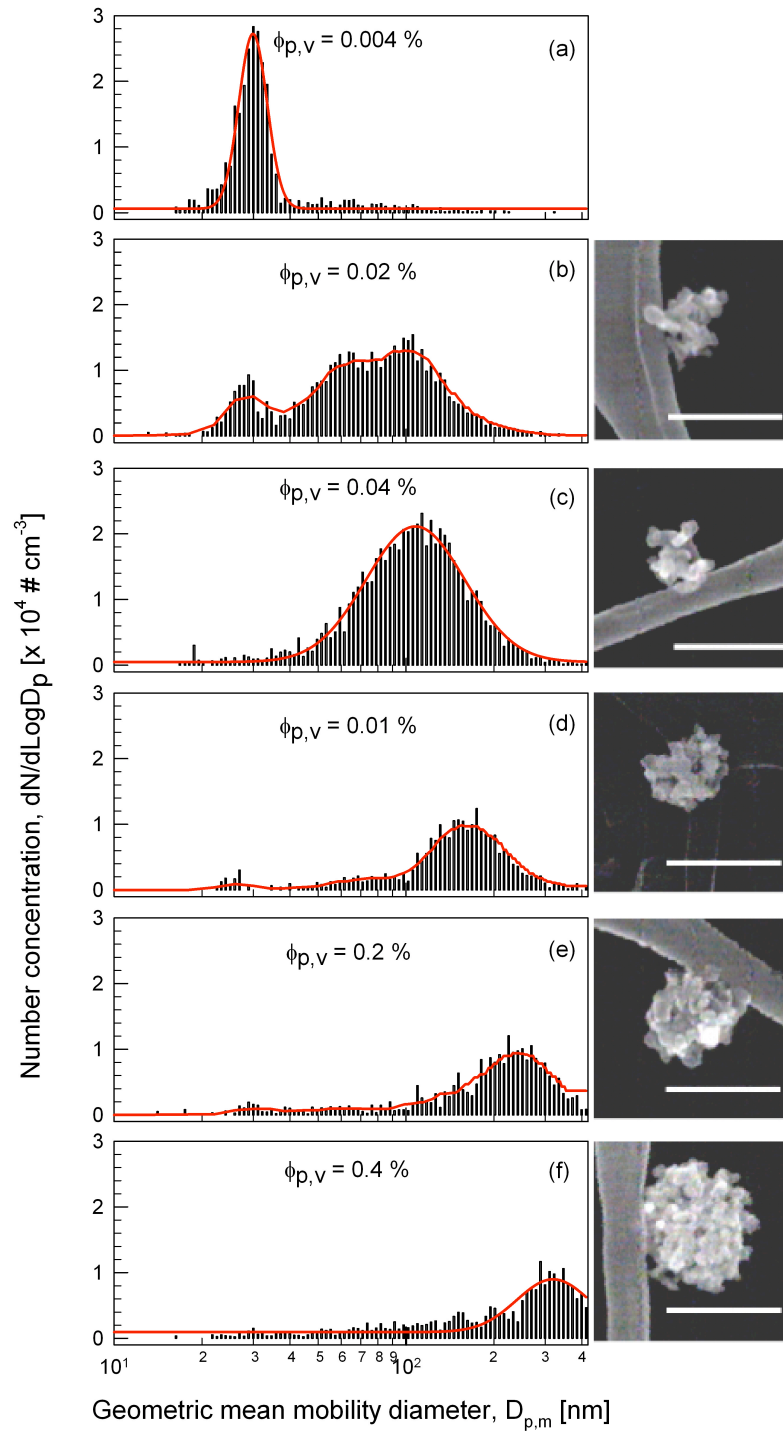
**Figure 3-6:** Particle size distribution of electrosprayed TiO$_2$ suspensions of varying particle volume fraction and constant K$_{eff}$ ~ 2x10$^{-3}$ S m$^{-1}$. The insets show SEM images of dried agglomerates produced by electrospraying the respective suspension. The white bar the represents 300 nm.

In Figure 3-6, increasing $\phi_{p,v}$ clearly shifted the size distribution towards larger sizes simultaneously decreasing the particle number concentration, which indicate the formation of particle agglomerates. The images to the right of the size distributions show SEM micrographs of electrosprayed agglomerates collected on microscopy grids that demonstrate the formation of compact spherical agglomerates for $\phi_{p,v} > 0.04$ %. The spherical agglomerates had a mean particle size of 100 nm, 150 nm, 200 nm, and 300 nm for $\phi_{p,v}$ 0.04 %, 0.01 %, 0.20 %, and 0.400 % respectively. By electrospraying suspensions with sufficiently high $K_L$ (in the range of $10^{-3}$ S m$^{-1}$), in the cone-jet mode, mother droplets can be generated with a size independent of $\phi_{p,v}$. Thus, the agglomerate size can be precisely controlled by tuning the particle volume fraction in the precursor suspension. Note that in that $K_L$ range, the pH of the suspensions was nearly constant (Table 2) and the zeta potential, which is related to the surface charge of the particles, was positive. As evaporation of the droplet takes place, the Rayleigh limit is reached and Coulombic fissions occur. However, due to the high conductivity of the suspensions, the progeny droplets are much smaller than the mother droplet and produced by a Taylor cone type process (de la Mora, 1996; Hunter & Ray, 2009). Furthermore, due to the droplet's high surface conductivity (Hunter & Ray, 2009), the TiO₂ nanoparticles are confined to the center of the droplet and do not escape the mother droplet. Thus, the fine sized progeny droplets merely carry away mass and charge.

It should be noted in Figure 3-6 that the mobility-based particle size distribution is broad, with a geometric standard deviation larger than 1.2, for values $\phi_{p,v}$ higher than 0.020 %. Two factors influence the broadening of the size distribution of electrosprayed TiO₂ agglomerates. First, droplets produced by electrospray may have a distribution of

sizes with a geometric standard deviation varying from 1.05 to 1.35 depending on both the electrospray mode and the liquid viscosity (Hogan & Biswas, 2008b). Second, the number of particles in an electrosprayed droplet from a colloidal suspension has been found to follow a Poisson distribution (Hogan & Biswas, 2008a, 2008b).
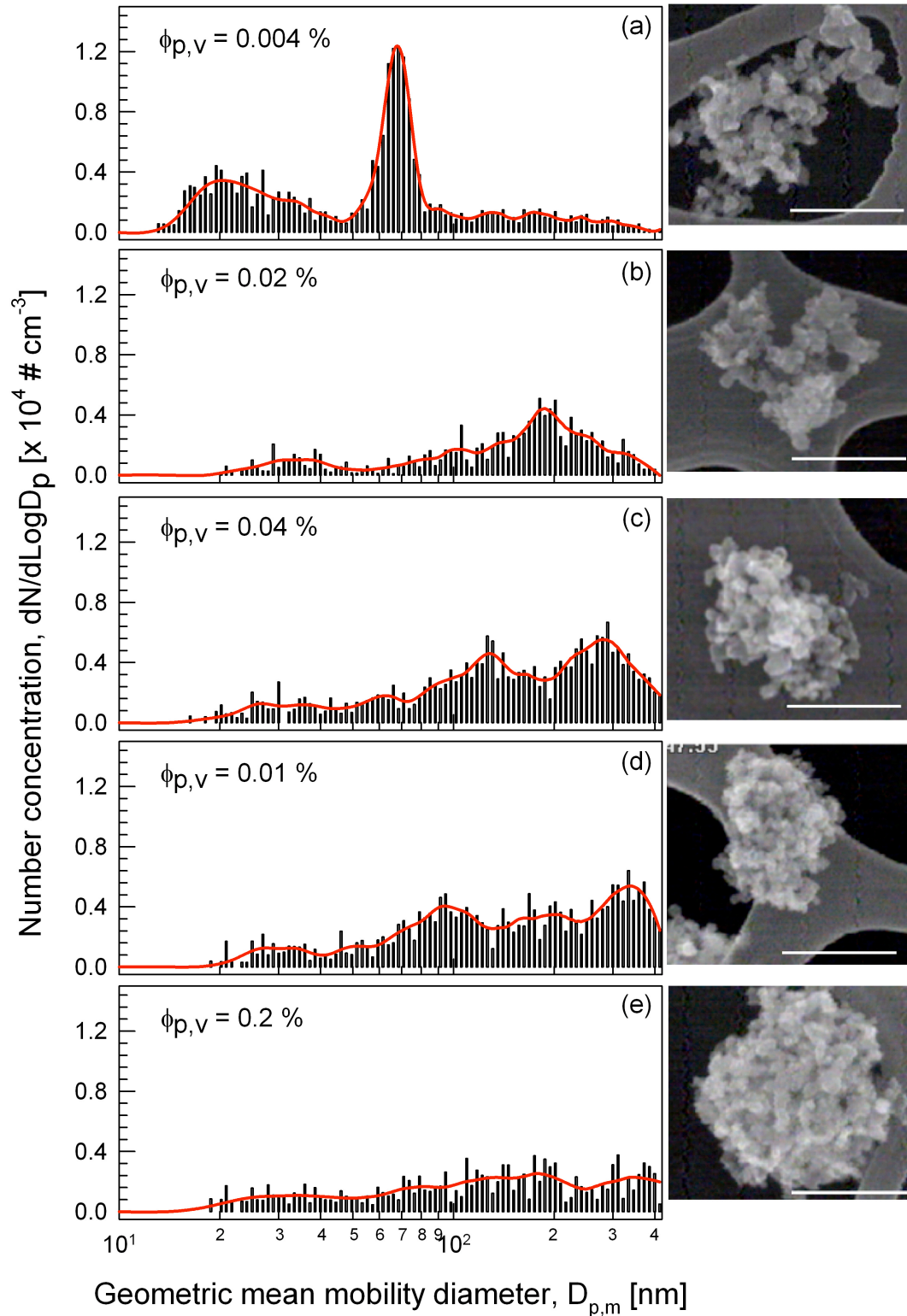
**Figure 3-7:** Particle size distribution of electrosprayed TiO$_2$ suspensions with varying volume fraction, without acid addition. The white bar indicates 300 nm.

To investigate the agglomerate formation in droplets from suspensions with low conductivity, suspensions without acid (curve (a) in Figure 3-2) were also electrosprayed. In those suspensions, the pH decreased with increasing the particle volume fraction (see Table I-1 in Appendix I), indicating that nanoparticles played a dominant role in controlling the conductivity phenomena. The size distributions of suspensions with low $K_L$ are shown in Figure 3-7 for various $\phi_{p,v}$ of (a) 0.004 %, (b) 0.020 %, (c) 0.040 %, (d) 0.100 %, and (e) 0.200 %; the size distribution of the 0.400 % suspension was beyond the limits of the sizing instrument and is not shown. Electrospraying suspensions of lower $K_{eff}$ (no acid added) generated broader multimodal size distributions than those of suspensions of higher $K_{eff}$ (containing $HNO_3$), and the agglomerates' size and morphology were difficult to control as seen from the SEM images. At lower $K_{eff}$, the droplets did not break up via formation of Taylor cone (de la Mora, 1996), but broke into equal fragments. This break up process resulted in mother and progeny droplets both containing $TiO_2$ nanoparticles. Further, the droplet's surface conductivity was not large enough to create strong ballistic forces on the nanoparticles (Hunter & Ray, 2009). Thus, Brownian motion resulted in caused random distribution of nanoparticles within the droplet and resulted in broader distributions of size.

The size and morphology are two key parameters that strongly affect the transport characteristics of the agglomerates, thereby affecting the properties of the resulting products: films, powders, etc. To evaluate such effect on the production of films, $TiO_2$ nanosuspensions with high liquid conductivity (constant $D_D$) were electrosprayed to fabricate water-splitting films; and the results are discussed in the next section.

3.4.2 Application to the Synthesis of Water-splitting Films

*3.4.2.a. Film deposition and characteristics*

The size of the depositing agglomerates strongly influences film thickness, film porosity, and film morphology, because it affects their transport characteristics and the penetration in the film. Figure 3-8 shows cross sectional SEM images of electrospray deposited films from suspensions with $\phi_{p,v}$ of (a) 0.04 %, (b) 0120 %, (c) 0.20 %, and (d) 0.40 %. For constants $K_L$ and $D_D$, and for the same number of deposited particles, a lower $\phi_{p,v}$ resulted in a more compact and thinner film (Figure 3-8(a)). Conversely, an increasing particle volume fraction resulted in a thicker, more porous film, and with a more open structure (Figure 3-8(d)).

**Table 3-2:** Electrosprayed films' physical parameters and measured photocurrent in a water-splitting system. To maintain a constant total mass of deposited particles (0.165 mg) in each film, the deposition time was varied.

| Volume fraction of particles, $\phi_p$ [%] | Average number of particles per agglomerate [#] | Average film thickness [μm] | Air to particle volume ratio, APV [-] | Photocurrent [mA cm⁻²] |
|---|---|---|---|---|
| 0.04 | 64 | 2.82 | 10.1 | 0.1258 |
| 0.10 | 216 | 3.35 | 13.4 | 0.0402 |
| 0.20 | 885 | 3.53 | 14.1 | 0.0246 |
| 0.40 | 1728 | 5.91 | 24.3 | 0.0196 |

Table 3-2 summarizes quantitative results of film porosity, represented as the air to particle volume ratio (APV), and film thickness as a function of the average number of particles per agglomerate $N_{p,agg}$ for suspensions with 0.32 mM $HNO_3$. The deposition of larger agglomerates resulted in the production of thicker and more porous films. The number of particles in an agglomerate is the parameter that most strongly affects the film porosity (Madler, et al., 2006); however, the agglomerate morphology plays an important role. As seen in the SEM images in Figure 3-6, the deposited agglomerates had compact spherical morphology with a high fractal dimension (close to 3.0). In such a case, larger agglomerates hinder the penetration of other agglomerates into the film increasing the film thickness, as shown in Figure 3-8 when a suspension with $\phi_{p,v} = 0.4$ % was electrospray deposited compared to the deposition of a suspension with ten times lower $\phi_{p,v}$. Therefore, control of film thickness and porosity could be achieved by electrospraying suspensions with $K_L$ in the range $10^{-3}$ S m$^{-1}$, by varying the particle volume fraction in the suspension. It is important to emphasize that electrospray of suspensions without acid (Curve (a) in Figure 3-2) resulted in the production of agglomerates with a wide range of size and fractal dimension (data not shown), thus making difficult the control of film properties. The film thickness and film porosity can affect the performance of the films strongly, especially when a certain optimal film morphology is desired (Thimsen, et al., 2008).
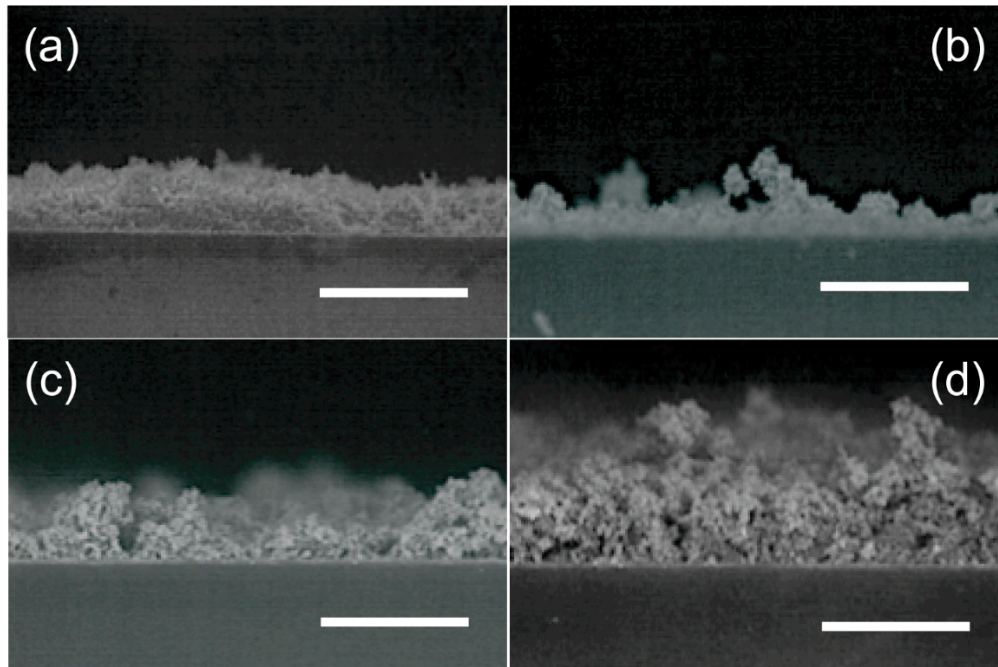
**Figure 3-8:** Cross sectional SEM images of TiO$_2$ films electrospray deposited from suspensions with particle volume fraction of (a) 0.04 %, (b) 0.10 %, (c) 0.20 %, and (d) 0.40 %. The white bar represents 6 μm.

### *3.4.2.b. Film characterization by hydrogen generation in a watersplitting system*

As discussed in the previous section, film morphology is a key factor that affects film performance. To investigate the effect of the size of the electrosprayed agglomerate on film properties, the films were tested in a watersplitting system. Table 3-2 summarizes the measured photocurrent after 10 s of illumination in a watersplitting system (Thimsen, et al., 2008) as a function of the APV of films made by electrospraying suspensions with varying particle volume fraction and constant (high) $K_L$. All films contain the same mass of particles, 0.165 mg (i.e. same number of particles). After 10 s of illumination, the measured photocurrents were 0.21 mA mg$^{-1}$, 0.43 mA mg$^{-1}$, 0.26 mA mg$^{-1}$, and 1.35 mA

mg$^{-1}$ for $\phi_{p,v}$ of 0.40 %, 0.20 %, 0.10 %, and 0.04 % in the precursor suspension, respectively. Electrospraying of smaller agglomerates resulted in the production of less porous and thinner films. Increasing the $\phi_{p,v}$ of the precursor suspension during the electrospray produced more porous films, which yielded lower photocurrent. Thus, the better performance of the 0.040 % film can certainly be attributed to a shorter electron travel time in the thinner and less porous film than the in the more porous film. In the latter, the electron has to follow a larger pathway from the film surface to the substrate because the film is thicker and contain more voids, dramatically decreasing the photocurrent and the hydrogen production rate. These results are in good agreement with the ones reported by Fujimoto et al (2006), in which electrospray deposited films of TiO$_2$ nanoparticle dispersions showed to have more organized pathways for ions transfer than films fabricated by a screen-printing method. Hogan and Biswas (2008b) also showed that electrospray deposition of smaller agglomerates would result in thinner, less porous films, with a lower surface roughness, and with smaller surface area.

## 3.5 Conclusions

Suspensions containing various concentrations of TiO$_2$ nanoparticles were electrosprayed to obtain agglomerates with different characteristics, which were then deposited to produce films with varying morphology, thickness, and porosity. The presence of nanoparticles in the liquid resulted in a significant change in the effective electrical conductivity, when $K_L$ was in the range of 10$^{-4}$ to 10$^{-3}$ S m$^{-1}$, increasing with increasing volume fraction of particles. When $K_L$ was in the range of 10$^{-3}$ to 10$^{-2}$ S m$^{-1}$, however, addition of particles did not have any significant impact on the effective

electrical conductivity. Precise size control of TiO$_2$ nanoparticle agglomerates was achieved by electrospraying suspensions with an initial liquid conductivity of the order of $10^{-3}$ S m$^{-1}$ and by varying the particles volume fraction in the suspension. A higher $K_L$ (i.e. a higher liquid ionic strength) influenced the breakup of agglomerates, formed in the liquid phase, because of an increased number of droplet fissions compared to suspensions with lower $K_L$. Based on the value of the charge relaxation length, droplet fissions during the electrospray occurred trough Coulombic explosions that produced large progeny droplets and resulted in compact spherical agglomerates. Electrospray deposition of smaller agglomerates resulted in a more compact film with lower porosity and showed better watersplitting performance than films made of larger agglomerates, because of a shorter electron travel time in the film. Electrospray in the cone-jet mode proved to be a very useful tool to precisely control agglomerate size during nanostructured film deposition. Hence, electrospray has potential applications in the fabrication of photocatalytic thin films and solar cells. Nevertheless, the low particle throughput with electrospray represents an issue that must be addressed, for instance through the use of multinozzle electrosprays. The methodology described in this work, however, has broader implications in inhalation and drug delivery studies where control of particle size and morphology is critical to assess the deposition location of the particles.


## 3.6 References

Abécassis, B., Cottin-Bizonne, C., Ybert, C., Ajdari, A., & Bocquet, L. (2008). Boosting migration of large particles by solute contrasts. *Nat. Mater.,* **7**, 785-789.

Bach, U., Lupo, D., Comte, P., Moser, J.E., Weissortel, F., Salbeck, J., Spreitzer, H., & Gratzel, M. (1998). Solid-state dye-sensitized mesoporous TiO$_2$ solar cells with high photon-to-electron conversion efficiencies. *Nature,* **395**, 583-585.

Barrero, A., Ganan-Calvo, A.M., Davila, J., Palacios, A., & Gomez-Gonzalez, E. (1999). The role of the electrical conductivity and viscosity on the motions inside Taylor cones. *J. Electrostat.,* **47**, 13-26.

Beckenridge, R.G., & Hosler, W.R. (1953). Electrical properties of titanium dioxide semiconductors. *Phys. Rev.,* **91**, 793-797.

Chakraborty, S., & Padhy, S. (2008). Anomalous electrical conductivity of nanoscale colloidal suspensions. *ACS Nano,* **2**, 2029-2036.

Chen, C.H., Kelder, E.M., & Schoonman, J. (1999). Electrostatic sol-spray deposition (ESSD) and characterisation of nanostructured TiO$_2$ thin films. *Thin Solid Films,* **342**, 35-41.

Chen, D.-R., & Pui, D.Y.H. (1997). Experimental investigation of scaling laws for electrospraying: Dielectric constant effect. *Aerosol. Sci. Tech.,* **27**, 367-380.

Cloupeau, M., & Prunet-Foch, B. (1994). Electrohydrodynamic spraying functioning modes - A critical review. *J. Aerosol Sci.,* **25**, 1021-1036.

Cruz, R.C.D., Reinshagen, J., Oberacker, R., Segadaes, A.M., & Hoffmann, M.J. (2005). Electrical conductivity and stability of concentrated aqueous alumina suspensions. *J. Colloid Interf. Sci.,* **286**, 579-588.

de la Mora, J.F. (1996). On the outcome of the coulombic fission of a charged isolated drop. *J. Colloid Interf. Sci.,* **178**, 209-218.

de la Mora, J.F., & Loscertales, I.G. (1994). The current emitted by highly conducting

    Taylor cones. *J. Fluid. Mech.,* **260**, 155-184.

Fang, F., & Zhang, Y.F. (2005). DC electrical conductivity of Au

    nanoparticle/chloroform and toluene suspensions. *J. Mater. Sci.,* **40**, 2979-2980.

Friedlander, S.K. (1977). *Smoke, dust, and haze : fundamentals of aerosol dynamics*

    (Second ed.). Wiley, New York.

Fujimoto, M., Kado, T., Takashima, W., Kaneto, K., & Hayase, S. (2006). Dye-sensitized

    solar cells fabricated by electrospray coating using TiO$_2$ nanocrystal dispersion

    solution. *J. Electrochem. Soc.,* **153**, A826-A829.

Ganan-Calvo, A.M., Davila, J., & Barrero, A. (1997). Current and droplet size in the

    electrospraying of liquids. Scaling laws. *J. Aerosol Sci.,* **28**, 249-275.

Gratzel, M. (2004). Conversion of sunlight to electric power by nanocrystalline dye-

    sensitized solar cells. *J. Photoch. Photobio. A,* **164**, 3-14.

Hartman, R.P.A., Borra, J.P., Brunner, D.J., Marijnissen, J.C.M., & Scarlett, B. (1999).

    The evolution of electrohydrodynamic sprays produced in the cone-jet mode, a

    physical model. *J. Electrostat.,* **47**, 143-170.

Hogan, C.J., & Biswas, P. (2008a). Monte Carlo simulation of macromolecular ionization

    by nanoelectrospray. *J. Am. Soc. Mass. Spectr.,* **19**, 1098-1107.

Hogan, C.J., & Biswas, P. (2008b). Porous film deposition by electrohydrodynamic

    atomization of nanoparticle sols. *Aerosol. Sci. Tech.,* **42**, 75-85.

Hunter, H.C., & Ray, A.K. (2009). On progeny droplets emitted during Coulombic

    fission of charged microdrops. *Phys. Chem. Chem. Phys.,* **11**, 6156-6165.

Iskandar, F., Nandiyanto, A.B.D., Yun, K.M., Hogan, C.J., Okuyama, K., & Biswas, P. (2007). Enhanced photocatalytic performance of brookite TiO₂ macroporous particles prepared by spray drying with colloidal templating. *Adv. Mater.,* **19**, 1408-1412.

Janusz, W., Sworska, A., & Szczypa, J. (1999). The structure of the electrical double layer at the titanium dioxide ethanol solutions interface. *Colloid. Surface. A,* **152**, 223-233.

Jaworek, A., & Sobczyk, A.T. (2008). Electrospraying route to nanotechnology: An overview. *J. Electrostat.,* **66**, 197-219.

Jiang, J., Chen, D.-R., & Biswas, P. (2007). Synthesis of nanoparticles in a flame aerosol reactor with independent and strict control of their size, crystal phase and morphology. *Nanotechnology,* **18**, 285603-285610.

Kulkarni, P., & Biswas, P. (2003). Morphology of nanostructured films for environmental applications: Simulation of simultaneous sintering and growth. *J. Nanopart. Res.,* **5**, 259-268.

Kulkarni, P., & Biswas, P. (2004). A Brownian dynamics simulation to predict morphology of nanoparticle deposits in the presence of interparticle interactions. *Aerosol. Sci. Tech.,* **38**, 541-554.

Lenggoro, I.W., Xia, B., Okuyama, K., & de la Mora, J.F. (2002). Sizing of colloidal nanoparticles by electrospray and differential mobility analyzer methods. *Langmuir,* **18**, 4584-4591.

Li, K.Y., Tu, H.H., & Ray, A.K. (2005). Charge limits on droplets during evaporation. *Langmuir,* **21**, 3786-3794.

Madler, L., Lall, A.A., & Friedlander, S.K. (2006). One-step aerosol synthesis of
    nanoparticle agglomerate films: simulation of film porosity and thickness.
    *Nanotechnology,* **17**, 4783-4795.

Modesto-Lopez, L.B., Collins, A.M., Blankenship, R.E., & Biswas, P. (2010).
    Electrospray-assisted characterization and deposition of chlorosomes to fabricate
    a light-harvesting biomimetic device. *Energy Environ. Sci.,* **3**, 216-222.

Modesto-Lopez, L.B., Pasteris, J.D., & Biswas, P. (2009). Sensitivity of micro-Raman
    spectrum to crystallite size of electrospray-deposited and post-annealed films of
    iron-oxide nanoparticle suspensions. *Appl. Spectrosc.,* **63**, 627-635.

Pagliaro, M., Palmisano, G., Ciriminna, R., & Loddo, V. (2009). Nanochemistry aspects
    of titania in dye-sensitized solar cells. *Energy Environ. Sci.,* **2**, 805 - 896.

Pavlin, M., Slivnik, T., & Miklavcic, D. (2002). Effective conductivity of cell
    suspensions. *IEEE T. Bio.-Med. Eng.,* **49**, 77-80.

Porter, J.F., Li, Y.G., & Chan, C.K. (1999). The effect of calcination on the
    microstructural characteristics and photoreactivity of Degussa P-25 TiO₂. *J.*
    *Mater. Sci.,* **34**, 1523-1531.

Rietveld, I.B., Kobayashi, K., Yamada, H., & Matsushige, K. (2006). Electrospray
    deposition, model, and experiment: Toward general control of film morphology.
    *J. Phys. Chem. B,* **110**, 23351-23364.

Rossum, J.R. (1975). Checking the accuracy of water analyses through the use of
    conductivity. *J. Am. Water Works Ass.,* **67**, 204-205.

Thimsen, E., & Biswas, P. (2007). Nanostructured photoactive films synthesized by a
    flame aerosol reactor. *AIChE J.,* **53**, 1727-1735.

Thimsen, E., Rastgar, N., & Biswas, P. (2008). Nanostructured TiO$_2$ films with

controlled morphology synthesized in a single step process: Performance of dye-

sensitized solar cells and photo watersplitting. *J. Phys. Chem. C,* **112**, 4134-4140.

Wang, B.X., Zhou, L.P., & Peng, X.F. (2003). A fractal model for predicting the effective

thermal conductivity of liquid with suspension of nanoparticles. *Int. J. Heat Mass

Transf.,* **46**, 2665-2672.

Widegren, J., & Bergstrom, L. (2002). Electrostatic stabilization of ultrafine titania in

ethanol. *J. Am. Ceram. Soc.,* **85**, 523-528.

# Chapter 4: Sensitivity of Micro-Raman Spectrum to Crystallite Size of Iron Oxide Nanostructured Films Made Via Electrospray Deposition of Nanosuspensions

**4.1 Abstract**

This paper demonstrates the sensitivity of the Raman spectra of electrospray-deposited iron-oxide nanoparticle films to their grain size. The grain size in the films was controlled by the temperature of annealing. The position and width of the bands at ~ 225, 612, 660, and 1317 $\Delta cm^{-1}$ were investigated for their sensitivity to both grain size and laser-induced heating, using 532-nm excitation. The parameter most sensitive to grain size was found to be the difference between the band position of the 660 $\Delta cm^{-1}$ LO and 225 $\Delta cm^{-1}$ TO bands ($X_{660}$-$X_{225}$). The distance between the two bands narrowed with increasing annealing temperature of the films, suggesting that, as grain size increases, these two bands become closer. The 660 $\Delta cm^{-1}$ band position was very stable regardless of variation in laser power and, thus, laser-induced heating effects. The films were prepared by electrospray-deposition of a commercial maghemite ($\gamma$-Fe₂O₃) nanoparticle suspension onto a silicon wafer followed by post-annealing in a temperature range of 600-1000 ºC for 15 min in an air atmosphere.

**4.2 Introduction**

Electrospray-deposition, a method of liquid atomization by electrical means, is becoming a common technique to deposit thin films of various materials with functional properties, such as CdS, ZnO, $TiO_2$, FePt and iron-oxides[1-6]. In the electrospray-deposition technique, a liquid that contains a chemical precursor or particles is fed through a metal capillary, which then is biased by a high voltage. The established electric field produces shear stress on the liquid surface, which causes elongation of a jet and its disintegration into charged droplets in the case of a dissolved precursor and of droplets with particles in the case of particle suspensions. In both cases, subsequent solvent evaporation leads to the formation of charged particles, which are accelerated toward a grounded substrate, where they deposit and form a film[7]. Electrospraying has several advantages over conventional methods to synthesize nanostructured films; for example, the generated droplets can be extremely small, down to nanometers, which is preferred for the production of nanostructured thin films. Moreover, the droplets can be monodisperse with a narrow size distribution when the electrospray is operated in the cone-jet mode[8,9], and the charge and size of the droplets can be controlled by adjusting the applied potential and the liquid flow rate.

Although fabrication of particulate films is very common, the number of characterization techniques that provide information about the physical properties of the deposited material is very limited. X-ray diffraction (XRD), transmission electron microscopy (TEM), and scanning electron microscopy (SEM) are some of the most frequently used techniques to analyze particulate thin films. Raman spectroscopy is a powerful experimental technique for probing the vibrational and structural properties of

materials and complements the other techniques[10]. Furthermore, Raman analysis does not require special sample preparation. It can be applied to solids, liquids, and gases, and the analysis can be carried out with a very small amount of material[11] in a relatively short period of time. However, it is known that the high power density from a laser excitation source can excessively heat a sample during a Raman experiment[12]. This is particularly true for micro-Raman experiments of nanomaterials (such as nanoparticles and nanostructured thin films), where laser beams are focused to a spot size with a diameter of only a few micrometers and the minute individual grains of the sample do not dissipate heat well. An increase in the local sample temperature may cause a frequency shift in the Raman bands, or it may cause physical degradation of a sample as the result of effects such as oxidation, recrystallization, order-disorder transitions, phase transition, and decomposition[13].

Thus, one major challenge for micro-Raman spectroscopy of nanostructured thin films is to decouple the band shifts and broadening due to size effects from those due to local heating during laser irradiation, the latter of which may lead to sample transformation. In this work, a systematic approach has been taken to identify the effects of crystallite size on the Raman spectra of electrospray-deposited and post-annealed films and to decouple those from the inherent heating effects due to laser irradiation.

Iron-oxide was chosen as the test material for its relevance to several modern technological applications. The different optical, mechanical, and electronic properties associated with the various crystal structures of iron-oxides have encouraged many practical uses, e.g., in biomedical applications as image-intensifying agents, in nuclear magnetic resonance imaging, in the electronics industry for magnetic recording devices,

in the environmental field as sorbents for heavy metal removal[6,14], in the paint industry as pigments[15, 16], in emerging energy production technologies as watersplitting films[17], and in many other applications that have been highlighted elsewhere[18].

These are some cautions about the application of Raman spectroscopy to ferric oxides. Iron oxides are good absorbers of radiation in the range of wavelengths produced by excitation lasers, necessitating special care about heating when they are used in a Raman experiment[13]. In addition, due to resonance effects, lasers of certain wavelengths can cause additional bands to be detected in the spectra of hematite.

## 4.3 Experimental Procedure

### 4.3.1 Film Preparation

Porous iron-oxide nanoparticle films were prepared by electrospray-depositing an iron-oxide nanoparticle suspension[9]. Commercial maghemite ($\gamma$-Fe₂O₃) nanopowder (Sigma Aldrich, particle size < 50 nm) was dispersed in ethanol, and a small amount of acetic acid (less than 1% vol) was added to keep the nanoparticles dispersed and to increase the electrical conductivity of the liquid. The suspension was fed through a stainless steel capillary nozzle, with an inner diameter of 160 μm, at a flow rate of 1 μL min$^{-1}$ using a syringe pump. A voltage of ~ 4 kV was applied to the nozzle to create a potential gradient with a grounded silicon (Si) wafer used as a substrate. The Si wafer was placed perpendicular to the capillary tip, at a distance of 1 cm. Maghemite nanoparticle suspensions were deposited for 1 h in the cone-jet mode[8, 19], and a digital optical microscope (QX5, Digital Blue, Atlanta, GA, USA) was used to monitor the

cone-jet during deposition experiments. After electrospray deposition, the films were annealed at temperatures of 600 ºC, 700 ºC, 800 ºC, 900 ºC, and 1000 ºC for 15 min in a furnace under air atmosphere. The purpose of annealing was to sinter the deposited particles and increase their apparent grain size.

### 4.3.2 Characterization of Film Morphology

Electrospray-deposited and post-annealed films were characterized using scanning electron microscopy (SEM, Model S-4500, Hitachi Ltd., Japan). Figure 4-1 shows SEM images of the electrospray-deposited iron-oxide nanoparticle films (a) without annealing, and annealed at temperatures of (b) 700 ºC, (c) 800 ºC, (d) 900 ºC, and (e) 1000 ºC. The agglomerates in Figures 4-1(a) and (b) are made of primary particles of the same size as those of the initial nanopowder and inherently contained a great number of particle-particle interfaces. However, as can be observed in the SEM image (Figure 4-1(c)) taken after the film was annealed at 800 ºC, the particles have started sintering; during this process the number of interfaces was dramatically reduced compared to that at 700 ºC. Further increase in annealing temperature (Figures 4-1 (d) and (e)) resulted in an increase in the apparent grain size and a further decrease in the number of interfaces.
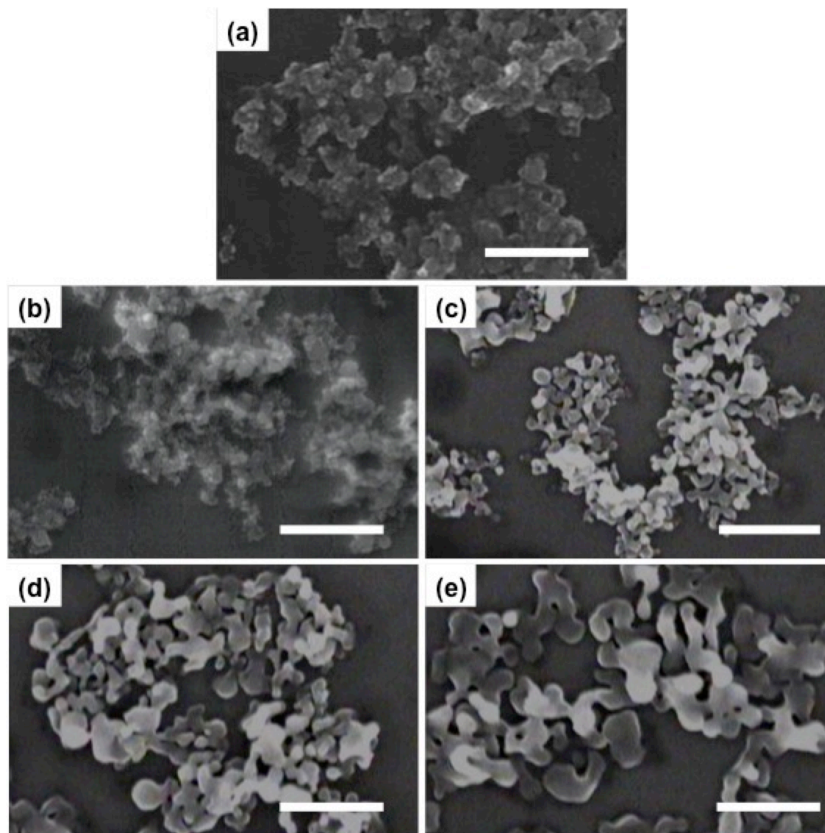
**Figure 4-1:** SEM images of electrospray-deposited iron-oxide nanoparticle films (a) without annealing and post-annealed at (b) 700 ºC, (c) 800 ºC, (d) 900 ºC, and (e) 1000 ºC. The white bar indicates 600 nm.

### 4.3.3 Micro-Raman Measurements

Micro-Raman spectroscopic studies were made with a HoloLab Series Research Raman Spectrometer (Kaiser Optical, Ann Arbor, Michigan) configured with 532-nm laser excitation. The instrument has an f/1.8 Holographic Imaging Spectrograph covering the spectral range of 0 to 4300 $\Delta$cm$^{-1}$ with a resolution of 2.5 cm$^{-1}$. It is configured with a Holoplex Transmission Grating (HPG-532) and an Andor high-resolution, thermoelectrically cooled CCD array detector with 2048 channels. The spectrometer is coupled to a 100-mW, 532-nm, frequency-doubled NdYAG visible laser. An 80x

objective with N.A. = 0.75 was used to focus optically on the sample and to deliver the laser. Each Raman analysis was the average of 32 accumulations at 4 seconds each. The Raman spectra were deconvolved based on a mixed Gaussian-Lorentzian band shape using GRAMS32® software (Galactic Industries, Incorporated; Salem, NH).

The systematic measurement was as follows. Using the microscope, a representative spot of 1 μm in diameter was selected in the film sample. For each sample, four different laser powers, measured as approximately 0.14, 0.23, 0.60, and 1.00 mW at the sample's surface, were used to analyze the same spot on the film (defined as a set of measurements). The laser power was varied by inserting neutral-density filters in the laser path; each laser power was measured prior to the start of the analysis of every film. To test the statistical variation and confirm the reproducibility of the results, four sets of measurements, a total of sixteen Raman analyses, were carried out on every film. Before each of the four sets of measurements at the four laser powers, the laser was defocused and focused again on the same spot. Reflected-light optical microscopy of the samples showed no physical degradation from the laser powers used in this study. During the deconvolution of the spectra, the background in all the films was horizontal; therefore no additional background correction was required.

## 4.4 Results and Discussion

Figure 4-2 compares the Raman spectra of commercial maghemite nanopowder and unannealed electrospray-deposited films with those of films post-annealed at temperatures of 600 to 1000 ºC on the silicon substrates. Note that the Si spectrum (h) is

superimposed on that of each adhering iron-oxide film. No significant differences were

observed between the spectra of the maghemite nanopowder (Figure 4-2(a)) and that of

the electrospray-deposited film without annealing (Figure 4-2(b)), suggesting that

deposition did not cause any physical transformation or degradation of the nanoparticles.
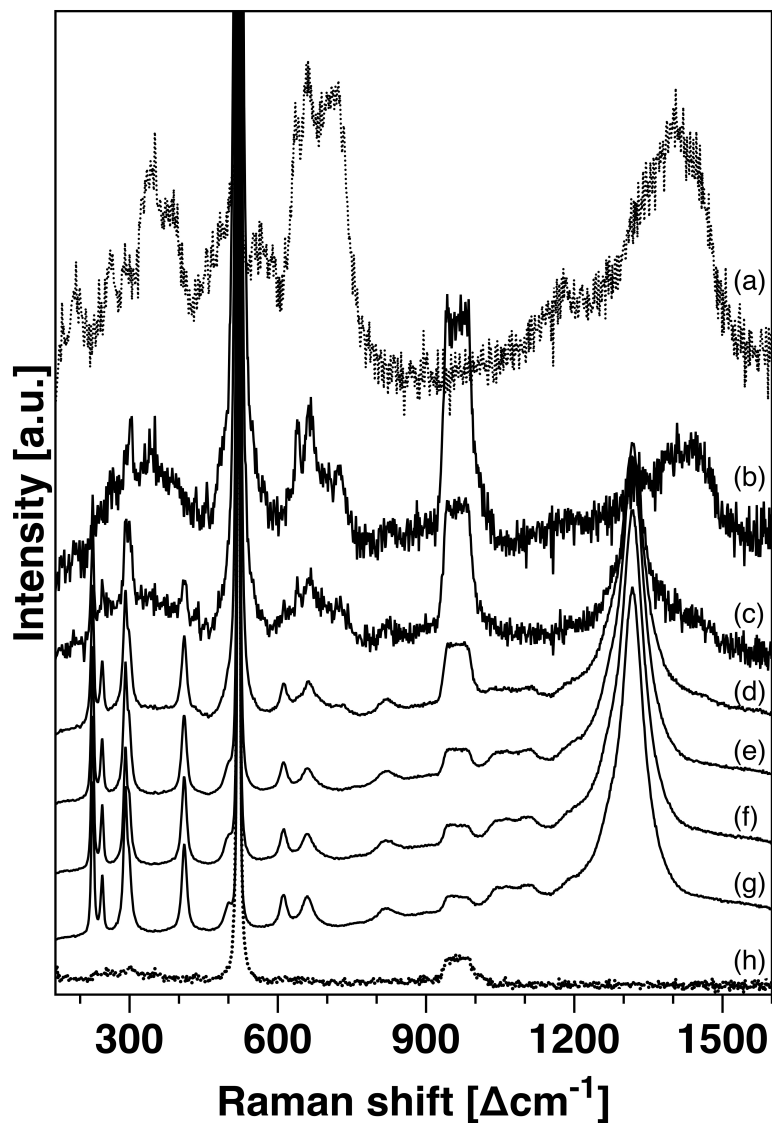


**Figure 4-2:** Raman spectra of (a) maghemite nanopowder, (b) electrosprayed films

without annealing and annealed at (c) 600 ℃, (d) 700 ℃, (e) 800 ℃, (f) 900 ℃, (g) 1000

℃, and (h) the Si wafer used as a substrate for the films. Laser intensity = 0.6 mW.

 The only difference may arise from the amount of material analyzed, which in the electrospray-deposited films was much smaller. The spectra of both the nanopowder and the unannealed film showed three Raman bands characteristic of maghemite identified as 350 (T$_1$), 500 (E), and 700 (A$_1$) $\Delta$cm$^{-1}$ [12, 20]. A change was observed in the micro-Raman spectrum of the sample annealed at 600 ºC, as shown in Figure 2(c). Characteristic bands of the maghemite nanopowder still can be observed, but they occur in addition to those peaks characteristic of hematite ($\alpha$-Fe$_2$O$_3$) at around 225 (A$_{1g}$), 245 (E$_g$), 293 (E$_g$), 298 (E$_g$), 412 (E$_g$), 500 (A$_{1g}$) and 610 (E$_g$) $\Delta$cm$^{-1}$ [12, 15, 18, 20, 21], all identified as transverse optical (TO) modes[18]. Furthermore, annealing at 600 ºC or higher temperature caused the broad 1400 $\Delta$cm$^{-1}$ band in Figures 4-2 (a) and (b) to disappear and a new band to appear at 1317 $\Delta$cm$^{-1}$. Although not many reports of the 1400 $\Delta$cm$^{-1}$ band in nano-maghemite were found in the literature, this band may be significant when distinguishing between the $\alpha$ and $\gamma$ phases of nano iron-oxide[22]. The origin of the 1317 $\Delta$cm$^{-1}$ band is controversial, and it has been identified as either a two-phonon scattering mode[23, 24] or a two-magnon scattering mode[21]. Since it appears at almost double the frequency of the 660 $\Delta$cm$^{-1}$ band, it could be considered as the latter's overtone except for the fact that the 660 $\Delta$cm$^{-1}$ band is only activated by a narrow range of laser wavelengths. For the purpose of this work, it is important to note that the relative intensity of the 1317 $\Delta$cm$^{-1}$ band increased with rising annealing temperature (Figure 4-2). Martin et al.[21] used a 531-nm laser wavelength to study the Raman spectra of hematite, but they did not report the 660 $\Delta$cm$^{-1}$ band. Interestingly, they mentioned that they did not observe an expected band at ~ 800 $\Delta$cm$^{-1}$, although it is allowed by symmetry; in our results, however, we observed a band at about 820 $\Delta$cm$^{-1}$. We have summarized in Table 4-1 previous reports by several

authors on the 660 Δcm$^{-1}$ band.  The data indicate that this band is activated only with certain laser wavelengths; i.e., it shows only moderate intensity with 514-nm[25] and 633-nm[18, 28, 30, 31] laser excitation, and low or very low intensity with other laser wavelengths[12, 23, 27, 32, 35]. Some authors did not observe the 660 Δcm$^{-1}$ band at all with 785-nm laser excitation[33, 34]. Others, using various laser wavelengths, did not mention the 660 Δcm$^{-1}$ band, although it was visible in their published spectra of hematite. In other cases, the presence of the 660 Δcm$^{-1}$ band in the Raman spectra of hematite was attributed to incomplete transformation of magnetite[25, 26, 28]. Our samples, however, were completely oxidized; furthermore, they were annealed in air at the indicated temperature, so we did not consider the presence of magnetite in our films. Noteworthy is the fact that Chernyshova et al.[18], using a 633-nm laser wavelength, observed a shift in the 660 Δcm$^{-1}$ band with varying nanoparticle size of hematite in solution. All the hematite spectra presented in this work (Figure 4-2(c-g)) show the seven characteristic Raman modes already indicated.


### 4.4.1 Effect of Laser Power

Earlier reports indicate that the specific position of a Raman band in oxide nanomaterials (nanoparticles and thin films) is influenced by the number of grain boundaries (compared to coarse materials), the number of surface defects, the phonon confinement effect due to their small size, and heating from the laser during a Raman analysis[36].

**Table 4-1:** Summary of reports on the 660 $\Delta cm^{-1}$ band found in the literature. Notations: VL: very low, L: low, M: moderate, NR: not reported, NO: not observed in spectra, *: observed in published spectra.

| Laser wavelength [nm] | Laser power [mW] | Reported position [$\Delta cm^{-1}$] | Intensity | Comments | Ref. |
|---|---|---|---|---|---|
| 514.5 | 0.5–10 | 664 | M | Glassy material containing hematite oxidized under $CO_2$ atmosphere (band attributed to the presence of magnetite). | 25 |
| | 0.5–10 | 664 | L | Pure hematite. | 25 |
| | 10–20 | 659 | VL | Mineral sample, Raman-inactive, IR-active $E_u$(LO) mode. | 23 |
| | 15 | 664 | VL* | Ancient Greek domestic pottery sherds. | 41 |
| 529 | - | NR* | VL* | Pellet of sintered hematite powder. | 22 |
| 531 | - | NR, NO | NR, NO | Hematite. | 21 |
| 632 | 20 | ~660* | L* | Hematite produced by laser-heated magnetite (band not observed in laser-heated magnetite nanoparticles). | 26 |
| 633 | 5 mW | NR, NO | NR, NO | Synthesized sample of hematite powder (HMS3-R-15999, Pfizer Inc.). | 27 |
| | 0.4 | 662 | M | Mixture of hematite and magnetite. | 28 |
| | 1.6 | - | - | Laser heated magnetite. | 28 |
| | < 0.7 | NR | VL* | Mineral hematite (Minas Gerais, Brazil) | 12 |
| | 0.7 | 662.7 | M | Flame-heated magnetite (Minas Gerais, Brazil). | 12 |
| | 0.8–10 | 660 | VL* | Mineral hematite sample. | 29 |
| | 1.5 | - | - | Hematite synthesized from liquid phase, particle size = 120 nm. | 18 |
| | 1.5 | ~660 | VL, L | Hematite synthesized from liquid phase, particle size = 35 and 7 nm. | 18 |
| | 1.5 | 657.422 | L | 18 nm hematite particles pressed in KBr. | 18 |
| | 1.5 | 659.975 | M | 7 nm hematite particles in suspension. | 18 |
| | 1.5 | 660.816 | M | 18 nm hematite particles dried. | 18 |
| | 1.5 | 656.148 | L | Hematite particles annealed at 400 °C; final particle size = 40 nm. | 18 |
| | 0.1 | ~ 660 | M | Annealed films (500 °C) made by dip coating iron oxide chemical precursor; band attributed to incomplete transformation of magnetite. | 30 |
| 647 | - | 660 | VL, L | Stucco samples from the buildings of Maya classic Copan. | 31 |
| | 5–7 | ~ 660* | L* | Mineral from the United States. | 32 |
| 785 | NR | NR, NO | NR, NO | Mineral hematite sample. | 33 |
| | 20 | NR, NO | NR, NO | Hematite synthesized from liquid phase. | 34 |
| NR | NR | NR | VL* | Sonochemically synthesized, hollow nanohematite, annealed at 450 °C for 2 h. | 35 |

In our approach we have used very low laser power, less than 1.00 mW, to prevent physical transformation or degradation of the samples, and more importantly to minimize the heating effects. Figure 4-3 shows the Raman shift of the bands at approximately 225, 612, 660, and 1317 $\Delta$cm$^{-1}$ as a function of laser power. For the same annealing temperature (i.e., grain size), the positions of the 225 and 660 $\Delta$cm$^{-1}$ bands remained constant with increasing laser power within the uncertainty range. The downshift in the position of the 225 $\Delta$cm$^{-1}$ band for the 700 ºC film measured at 1.00 mW may be caused by traces of maghemite and the large number of grain boundaries; indeed, the SEM images in Figures 4-1(a) and (b) show no significant difference between the appearance of the unannealed film and that annealed at 700 ºC.  Moreover, the position of the 225 $\Delta$cm$^{-1}$ band at each laser power was also essentially the same regardless of annealing temperature. In contrast, at each fixed laser power, the average position of the 660 $\Delta$cm$^{-1}$ band differed significantly among the films annealed at different temperatures. The 612 and 1317 $\Delta$cm$^{-1}$ bands showed a slight down-shift with increasing laser power, which is expected in laser-heated nanomaterials[37]; however, for the 612 $\Delta$cm$^{-1}$ band, the total shift as laser power increases from 0.14 to 1.00 mW is still small compared to what has been reported in the literature for the same band[18, 30].

The effect of laser heating on bandwidth also was investigated. Figure 4-4 shows the full width at half maximum (FWHM) of the 225, 612, 660, and 1317 $\Delta$cm$^{-1}$ bands as a function of laser power. In all the films, the width of the 225 $\Delta$cm$^{-1}$ band shows essentially constant value with increasing laser power, except for the film annealed at 700 ºC; this film shows a width increase of 1.5 $\Delta$cm$^{-1}$ with the large uncertainty of ± 2 $\Delta$cm$^{-1}$ as laser power increased from 0.60 to 1.00 mW. This band broadening, similar to the

down-shift recorded at 1.00 mW laser power (Figure 4-3), may reflect an early stage of the sintering process, in which a large number of particle-particle interfaces and surface defects are predominant.
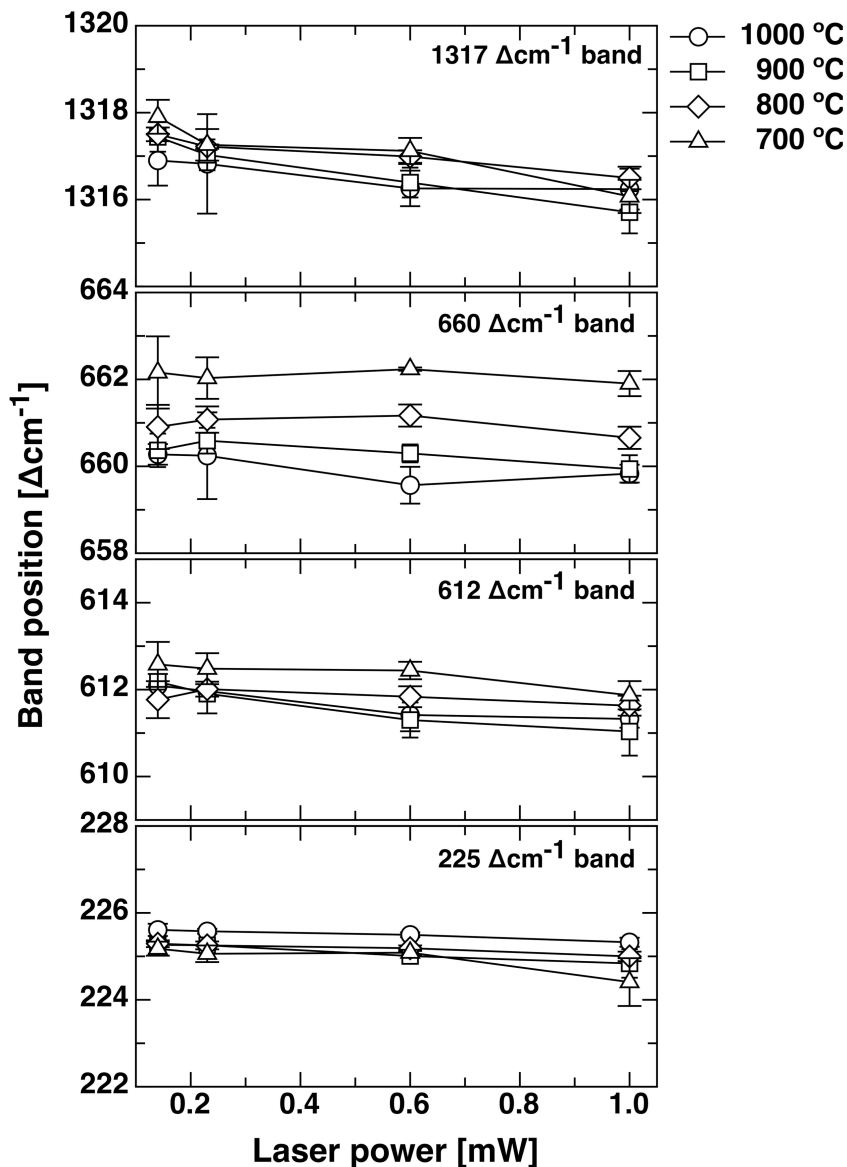


**Figure 4-3:** Band position of the 225, 612, 660, and 1317 $\Delta$cm$^{-1}$ bands as a function of laser power. In each diagram, the vertical axis shows a range of 6 cm$^{-1}$; thus permitting evaluation of the relative sensitivities of the different bands to laser heating and grain-size effects (i.e., annealing temperature).

Broadening is, nevertheless, typical of Raman bands observed in nanomaterials, where wide bands are associated with a low degree of atomic order. Unexpectedly, the 612 $\Delta$cm$^{-1}$ band showed an irregular oscillation of broadening and narrowing with increasing laser power in all the films. This phenomenon may be the result of lattice disorder associated with the crystallinity of hematite. In contrast, the film annealed at 1000 ºC shows a 612 $\Delta$cm$^{-1}$ bandwidth that remains constant with increasing laser power above 0.23 mW. For each film, the 660 $\Delta$cm$^{-1}$ band showed essentially a constant bandwidth across all but the lowest laser power (0.14 mW). The offset in the latter bandwidth may reflect the error introduced by high noise at the lowest laser excitation, thus making deconvolution difficult and preventing an accurate result. Nevertheless, it is important to emphasize that with laser powers above 0.14 mW, broadening of the 660 $\Delta$cm$^{-1}$ band due to increasing laser-induced heating was minimal and the analyses of very high precision, as can be seen in Figure 4-4. In the case of the 1317 $\Delta$cm$^{-1}$ band, all the films showed broadening with increasing laser power, especially the one annealed at 700 ºC, in which the bandwidth increased from about 55 cm$^{-1}$ at 0.14 mW to 63 cm$^{-1}$ at 1.00 mW.
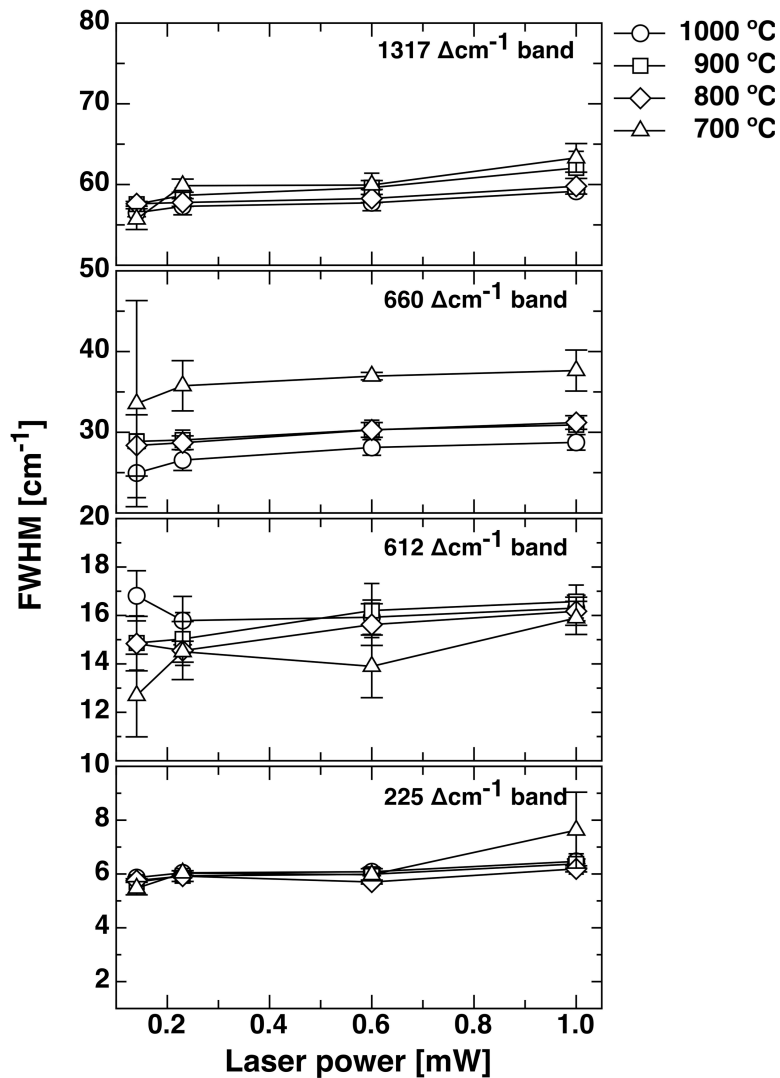
**Figure 4-4:** Full width at half-maximum intensity of the 225, 612, 660, and 1317 $\Delta cm^{-1}$ bands as a function of laser power (i.e., laser induced heating).

To verify whether the band shifts and band broadening observed were permanent the laser power was reduced from 1.00 to 0.14 mW. It was observed that in nearly all the cases the band positions returned to their original values recorded at the beginning of Raman analysis (with 0.14 mW), thus indicating that with the low laser powers used in this study the band positions and bandwidths were not affected permanently.

4.4.2 Effect of Annealing Temperature

Annealing of the samples was expected to increase the grain size and decrease the number of surface defects and grain boundaries. These physical changes can affect the Raman spectrum of a material, especially if its grain size is in the nanoscale range[10, 18]. That is because Raman scattering is highly sensitive to local vibrations of the bonded atoms, including the degree of atomic order. Increasing the annealing temperature would enhance sintering, a solid-state diffusion process, as well as restructuring of the crystallites at their grain boundaries. Slowly cooling the films would decrease the number of surface defects and the degree of internal disorder. In its enhancement of atomic order and its increasing of the length-scale of lattice continuity, annealing is likely to affect the Raman spectra of the films once they have cooled. A procedure to estimate the activation energy for sintering of electrospray deposited films, based on the transient variation of the films' surface area during annealing, is described in details in Appendix I. Figure 4-5 shows the band position of the 225, 612, 660, and 1317 $\Delta$cm$^{-1}$ bands as a function of annealing temperature, where the y-axis displays a range of 6 cm$^{-1}$ in each case. The 225 $\Delta$cm$^{-1}$ band up-shifted by approximately two wavenumbers with a 300 ºC increase in annealing temperature. Interestingly, at a fixed laser power, the positions of the 612 and 1317 $\Delta$cm$^{-1}$ bands remained nearly constant within uncertainties regardless of the annealing temperature. In contrast, the 660 $\Delta$cm$^{-1}$ band showed a well-defined down-shift with increasing annealing temperature, but, for any given annealing temperature, the position was nearly unaffected by laser power. This down-shift of the 660 $\Delta$cm$^{-1}$ band was unexpected. Typically it has been observed that Raman bands in oxide materials up-shift with increasing particle size[18], although Xu et al.[38] also observed an up-shift with

decreasing particle size of $TiO_2$ nanoparticles when they were coated with an organic acid, and Yang et al.[39] reported a down-shift of the 638 $\Delta cm^{-1}$ $E_{2g}$ mode of $TiO_2$ films when the thickness of the film synthesized by an aerosol route was reduced from 1 μm to 20 nm.
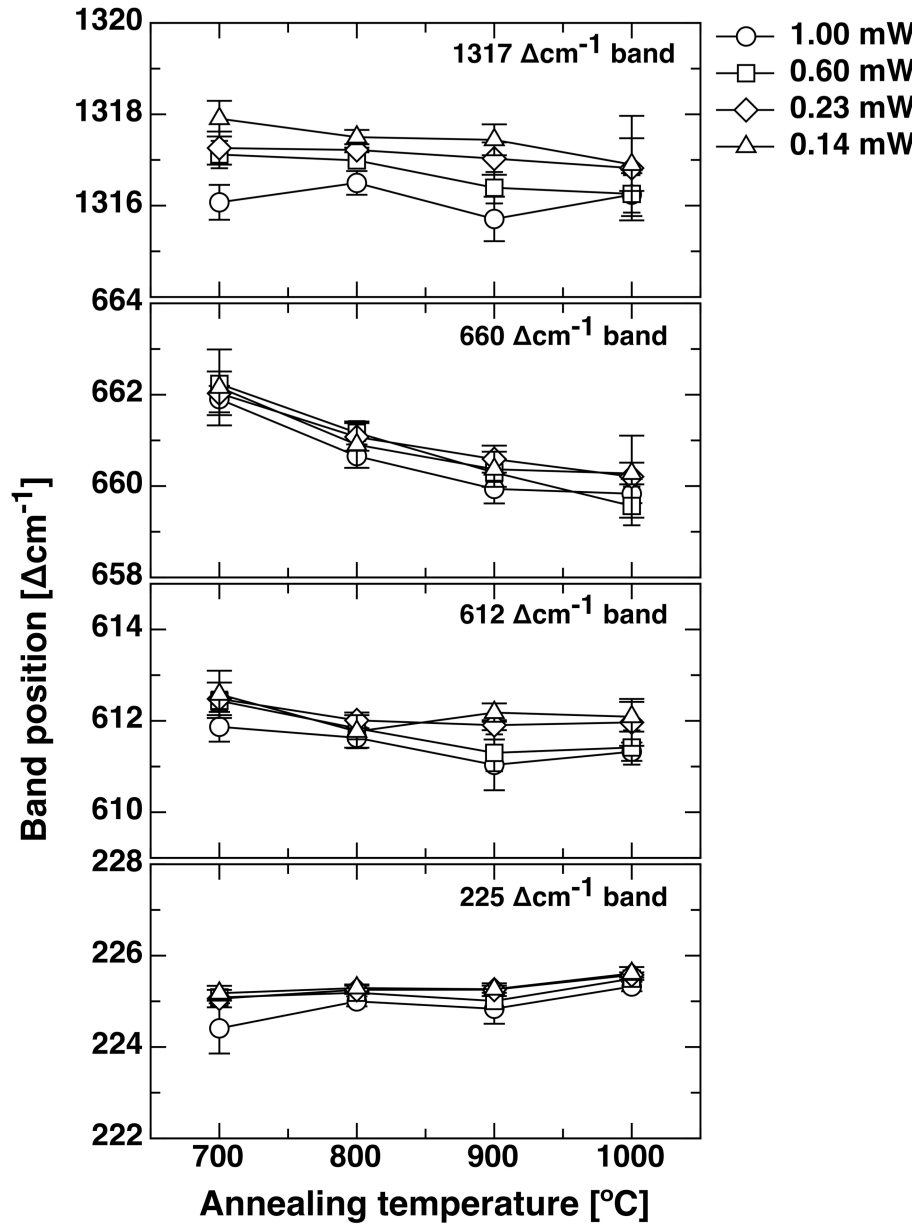


**Figure 4-5:** Band position of the 225, 612, 660, and 1317 $\Delta cm^{-1}$ bands as a function of annealing temperature (i.e., grain size).

The 660 $\Delta$cm$^{-1}$ band itself may be unusual. One, but only one paper, by Chernyshova et al.[18] reported this band as a longitudinal optical (LO) E$_u$ mode; and they attributed its origin to an extrinsic mechanism through disorder-induced break-down of the symmetry properties for the scattering LO phonon. Further, in their paper, Chernyshova and coauthors[18] discussed the variation in intensity of this band with particle size, and reported a down-shift due to heating by the laser. In their study, however, a down-shift was clearly indicated only with a reported laser power of 3.7 mW; with lower laser power, noisy spectra were obtained and a shift was difficult to identify. In our work, as shown in Figure 4-3, the position of the 660 $\Delta$cm$^{-1}$ band remains unaffected by laser powers up to 1.00 mW within the uncertainty interval, although the band position clearly depends on the annealing temperature. This fact is demonstrated again in Figure 4-5. In addition, even with the low laser power used in our Raman analyses, the 660 $\Delta$cm$^{-1}$ band was clearly distinguished as shown in Figure 4-2.
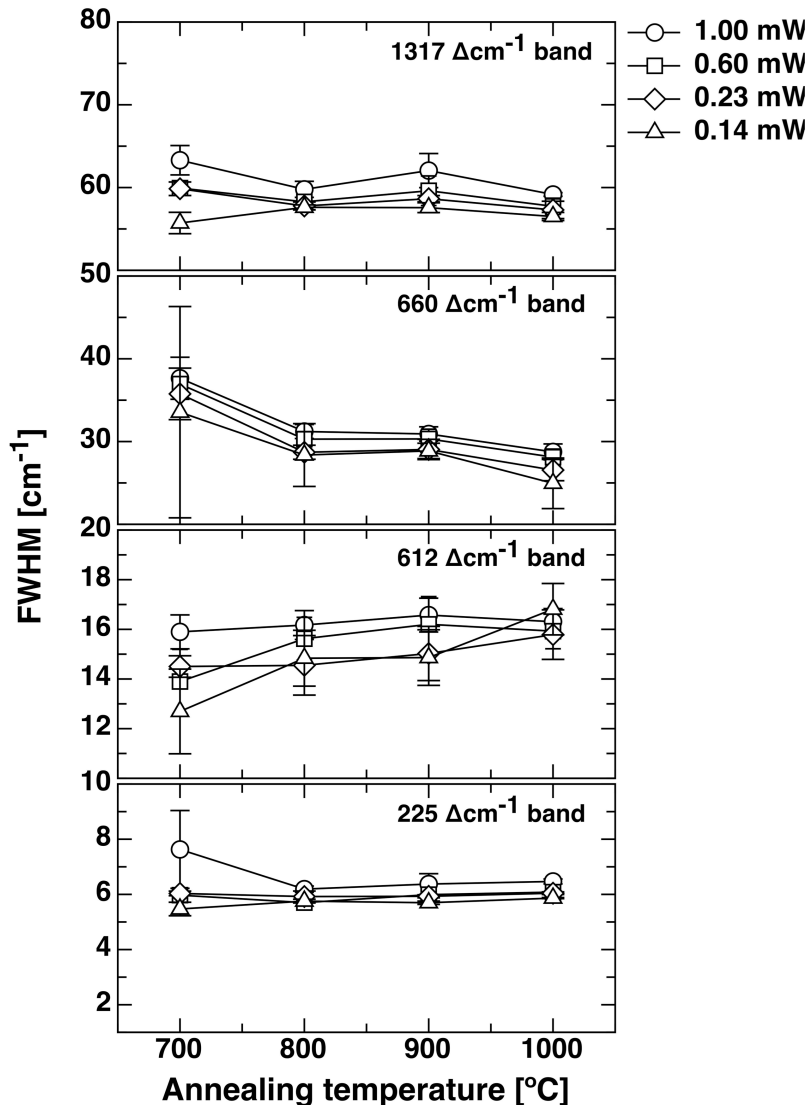
**Figure 4-6:** Full width at half-maximum intensity of the 225, 612, 660, and 1317 $\Delta cm^{-1}$ bands as a function of annealing temperature (i.e., grain size).

Figure 4-6 shows the FWHM of the 225, 612, 660, and 1317 $\Delta cm^{-1}$ bands as a function of annealing temperature. It can be observed that the 225 $\Delta cm^{-1}$ band does not broaden with decreasing annealing temperature, except under a laser power of 1.00 mW. In this case, broadening of approximately two wavenumbers was observed in the 700 ºC annealed film compared to the widths at other temperatures. This apparent broadening

may be an artifact, the result of recording a range in peak positions for the presumably polydisperse nanoparticle population that still exists at only 700 ºC. Although the 612 $\Delta cm^{-1}$ band broadens slightly with rise in annealing temperature, it shows some dependence on the laser power, as does the 1317 $\Delta cm^{-1}$ band. This dependence can be observed more readily in Figure 4-4. An increase in bandwidth with increasing annealing temperature (as for the 612 $\Delta cm^{-1}$ band) is unexpected, since band broadening typically occurs when crystallite size is reduced, especially down to the nanometer scale; in other words, coarsely crystalline materials typically show narrow Raman bands. The fact that only the films annealed at 700 ºC show a large increase in bandwidth with laser power (compare Figure 4-6 with Figure 4-4) suggests that laser-induced heating is the reason for the band broadening.

### 4.4.3 Successful Isolation of Sensitivity to Crystallite Size

In that Raman scattering results when a sampling beam interacts with bonded atoms and increases their vibrational energy, it is reasonable to think that some Raman bands will be more sensitive than others to these interactions. To study crystallite size effects on the Raman spectra of nanomaterials, it is necessary to identify the Raman bands that respond to these effects. Table 4-2 summarizes our results on spectral sensitivity.

**Table 4-2:** Sensitivity to annealing temperature and laser heating of different Raman bands of the iron-oxide films. H = high, M = moderate, L = Low, VL = Very low.

| Bands ($\Delta cm^{-1}$) | 225 | | 612 | | 660 | | 1317 | |
|---|---|---|---|---|---|---|---|---|
| Band parameter | position | width | position | width | position | width | position | width |
| Sensitivity to grain size, i.e., annealing temperature | L-M | VL | M | M | H | M-H | L-M | L-M |
| Sensitivity to laser heating | L | L | L | L | L | M | M-H | L-M |

The 225 $\Delta cm^{-1}$ band is a transverse optical (TO) mode and the 660 $\Delta cm^{-1}$ is a longitudinal optical (LO) mode[18]. Optical modes are the result of individual atomic vibrations, which are influenced by the neighboring atoms. White[40] pointed out that narrowing of the spectral separation between LO and TO modes is one phenomenon that has been observed when particle size is reduced beyond a certain limit. Our own data have shown that the 225 and 660 $\Delta cm^{-1}$ bands may provide information about the size of the crystallite. The difference in band position between the 225 and 660 $\Delta cm^{-1}$ bands, namely $X_{225}$ and $X_{660}$ respectively, is the parameter most sensitive to variations in the crystallite size.
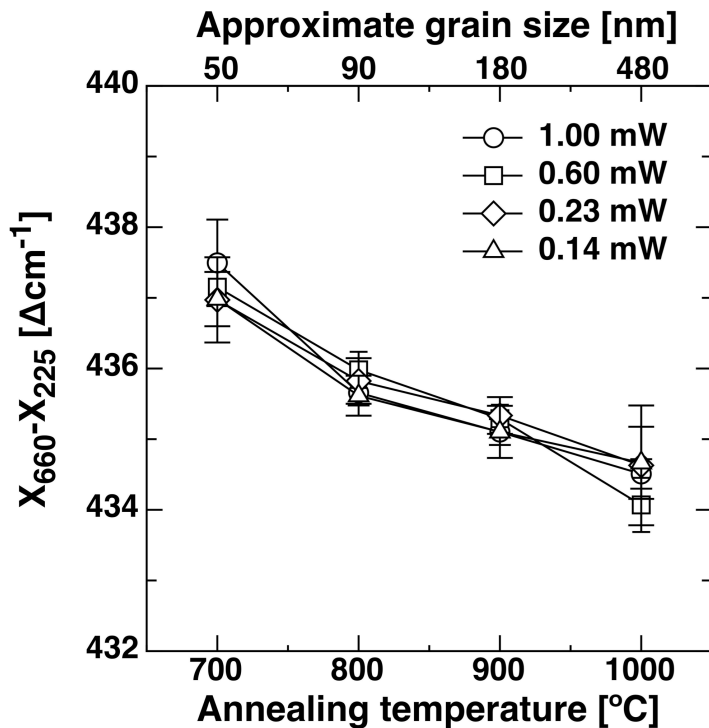
**Figure 4-7:** Difference between the positions of the 660 $\Delta cm^{-1}$ and the 225 $\Delta cm^{-1}$ bands as a function of annealing temperature. The approximate grain sizes corresponding to each annealing temperature are indicated along the upper horizontal axis.

Figure 4-7 shows this difference in band position, $X_{660} - X_{225}$, as a function of annealing temperature. It is clear that as annealing temperature was increased (thus increasing crystallite size) from 700 to 1000 ºC, the spectral separation between these two bands narrowed by about 3 $\Delta cm^{-1}$. This change in spectral peak separation is small, but analytically robust, as seen in the error bars. For particles of the same initial diameter, the time required for sintering 1) scales with the fourth power of the initial diameter and 2) exponentially decreases with increasing temperature. All of our films began with the same particle size (very small range). Thus, the sintering rate (or sintering efficiency for a fixed amount of time) depended only on the annealing temperature. The small amount

of spectral change reflects the change of only 300 ºC in annealing temperature (for which only at 800-1000 ºC was sintering actually documented). Certainly, additional variability was introduced by the deconvolution of the spectra when assigning the position of the bands, which would add an uncertainty to the band shifts as a function of annealing temperature. However, such uncertainty was countered by the number of analyses performed on each film. The data from these deconvolved spectra reflect the statistical reproducibility of the peak positions. Furthermore, spectral separation between two bands was used as the reference parameter rather than the absolute position of a single band, which eliminates some uncertainty. SEM images of the films showed that the films annealed at 600 ºC and 700 ºC had a mean grain size (or particle size) of about 50 nm, very close to the original particle size of the maghemite nanopowder, indicating that only minimal sintering had occurred. Films annealed at 800 ºC, 900 ºC, and 1000 ºC had a mean grain size of 89 nm, 178 nm, and 477 nm respectively. It is important to note that those values of mean grain size are a rough estimation, because it is difficult to identify the limits of the grains (grain boundaries) on the SEM images (see Figure 4-1). These values also are only a measure of an increase in visible grain size with increasing annealing temperature, whereas the Raman spectral parameters are sensitive to the actual length-scale of lattice continuity in the ultimate crystallites. Because the crystallites cannot exceed the size of the grains that contain them, however, the approximate size values shown on Figure 4-7 place an upper bound on the crystallite sizes at those annealing temperatures. The statistical distribution of grain sizes at each annealing temperature, which is an important factor for any future spectral calibration of nanoparticle size, have not been explicitly addressed.
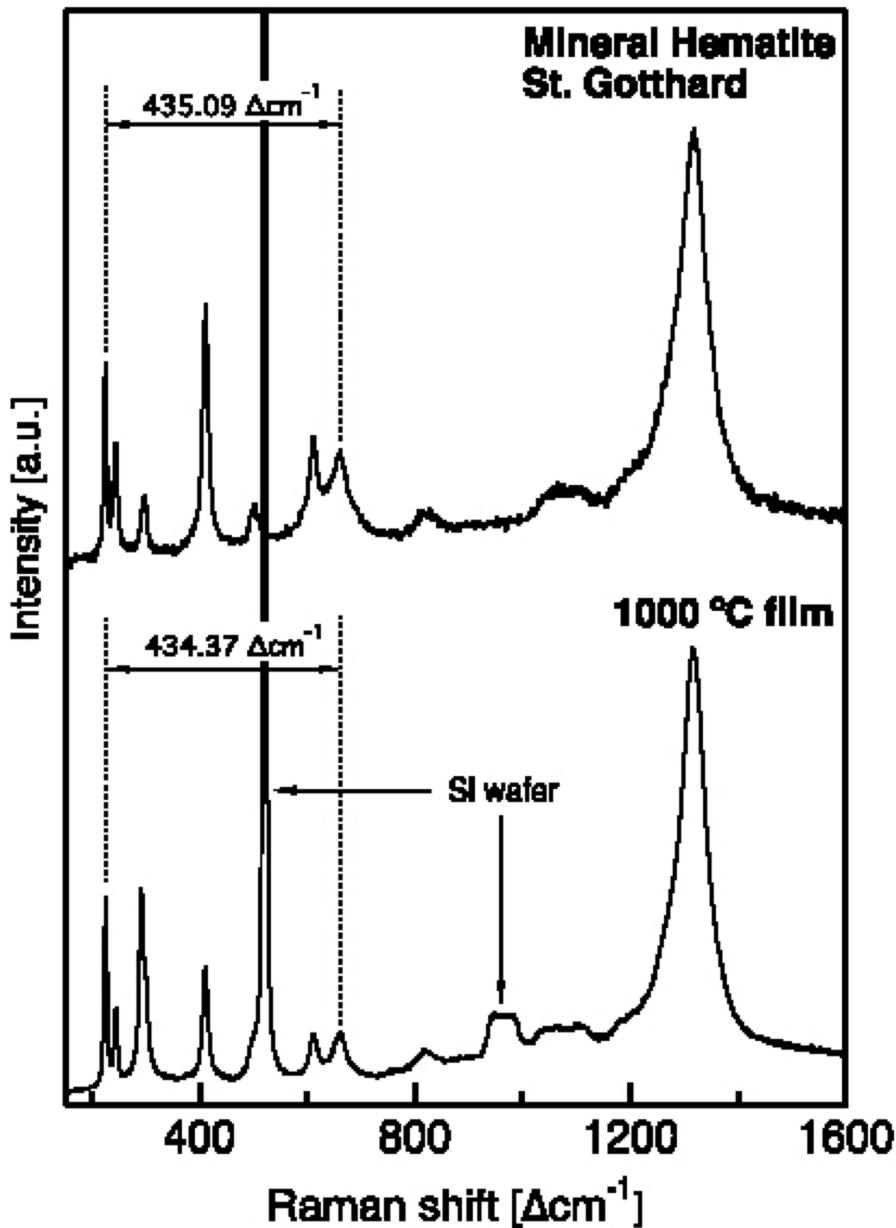
**Figure 4-8:** Comparison between the Raman spectra of natural hematite from St. Gotthard, Switzerland, and the film annealed at 1000 ºC.

The spectral separation for a natural hematite (St. Gotthard) is 435.09 $\Delta$cm$^{-1}$, indicating a relatively large crystallite size (Figure 4-8). The spectral parameters of natural hematite are not directly comparable to those of our own pure Fe$_2$O$_3$ films, however, due to the presence of trace contaminants in natural geological samples. Note

that the Raman spectrum of the hematite film is stronger (higher signal to noise ratio) than that of coarsely crystalline hematite, which is known to be a poor Raman scatterer. We infer that this difference in spectral intensity is due to the opaqueness of hematite. The Raman signal obtained from both the nanostructured films and the geologic sample arises only from the surface of each sample (little optical depth of penetration). Because the nanoparticles offer much more surface area (or surface roughness) to the laser beam than the relatively smooth geologic hematite, the spectra of the nanostructured films are markedly stronger.

## 4.5 Conclusions

Commercial maghemite nanoparticle films were produced by the electrospray deposition technique and converted into hematite by post-annealing the deposits. Complete phase transformation from maghemite to hematite was observed at an annealing temperature of 700 ºC. The 532-nm activated 660 $\Delta$cm$^{-1}$ LO mode in both its band position and width proved to be very sensitive to the annealed particle size of the hematite. Decrease in bandwidth of the 660 $\Delta$cm$^{-1}$ band showed that annealing indeed increased the length scale of atomic ordering and not just the apparent grain size. The spectral separation between the 225 $\Delta$cm$^{-1}$ LO band and the 660 $\Delta$cm$^{-1}$ TO band proved to be an especially useful parameter for future calibration of the crystallite size in the electrospray-deposited, post-annealed hematite films. The parameter is reasonably sensitive to crystallite size, but insensitive to laser power up to 1 mW. Moreover, the use of the difference in position between two bands rather than the absolute position of one band removes much of the instrument-dependent uncertainty due to differences in

spectral calibration among laboratories. The $X_{660}$-$X_{225}$ parameter's correlation with crystallite size should be transferable among laboratories. As the crystallite becomes larger, spectral separation decreases. Application of this approach to a natural hematite mineral sample showed that our results of decreasing spectral separation with increasing grain size were in reasonable agreement.

## 4.6 References

1. B. Su and K. L. Choy, Thin Solid Films, **359**, 160 (2000).

2. K. L. Choy, Mater. World **6**, 3, 144 (1998).

3. C. H. Chen, M. H. J. Emond, E. M. Kelder, B. Meester, and J. Schoonman, J. Aerosol Sci. **30**, 7, 959 (1999).

4. C. H. Chen, E. M. Kelder, and J. Schoonman, Thin Solid Films **342**, 35 (1999).

5. H. M. Lee, S. G. Kim, I. Matsui, T. Iwaki, F. Iskandar, I. W. Lenggoro, and K. Okuyama, J. Magn. Magn. Mater. **313**, 1, 62 (2007).

6. S. Basak, D.-R. Chen, and P. Biswas, Chem. Eng. Sci. **62**, 1263 (2007).

7. A. Jaworeck, J. Mater. Sci. **42**, 266 (2007).

8. J. Rosell-Llompart, and J. Fernández de la Mora, J. Aerosol Sci. **25**, 6, 1093 (1994).

9. C. J. Hogan Jr. and P. Biswas, Aerosol Sci. Tech. **42**, 75 (2008).

10. G. Gouadec and P. Colomban, J. Raman Spectrosc. **38**, 598 (2007).

11. K. Ajito and K. Torimitsu, Appl. Spectrosc. **56**, 4, 541 (2002).

12. D. L. A. de Faria, S. Venancio Silva, and M.T. de Oliveira, J. Raman Spectrosc. **28**, 873 (1997).

13. O. N. Shebanova and P. Lazor, J. Raman Spectrosc. **34**, 845 (2003).

14. S. Basak, K. S. Rane, and P. Biswas, Chem. Mater. **20**, 15, 4906 (2008).

15. J. Wang, W. B. White, and J. H. Adair, J. Am. Ceram. Soc. **88**, 12, 3449 (2005).

16. R. A. Goodall, J. Hall, R. J. Sharer, L. Traxler, L. Rintoul, and P. M. Fredericks, Appl. Spectrosc. **62**, 1, 10 (2008).

17. A. Duret, and M. Gratzel, J. Phys. Chem. B **109**, 17184 (2005).

18. I.V. Chernyshova, M. F. Hochella Jr, and A. S. Madden, Phys. Chem. Chem. Phys. **9**, 1736 (2007).

19. M. Cloupeau and B. Prunet-Foch, J. Aerosol Sci. **25**, 6, 1021 (1994).

20. I. Chamritski and G. Burns, J. Phys. Chem. B **109**, 4965 (2005).

21. T. P. Martin, R. Merlin, D. R. Huffman, and M. Cardona, Solid State Commun. **22**, 9, 565 (1977).

22. M. A. G. Soler, G. B. Alcantara, F. Q. Soares, W. R. Viali, P. P. C. Sartoratto, J. R. L. Fernandez, S. W. da Silva, V. K. Garg, A. C. Oliveira, and P. C. Morais, Surf. Sci. **601**, 3921 (2007).

23. K. F. McCarty, Solid State Commun. **68**, 8, 799 (1988).

24. S.-H. Shim, and T. S. Duffy, Am. Mineral. **87**, 318 (2002).

25. M. E. Minitti, M. D. Lane, and J. L. Bishop, Meteorit. Planet. Sci. **40**, 1, 55 (2005).

26. F. J. Owens, and J. Orosz, Solid State Commun. **138**, 95 (2006).

27. A. Wang, K. E. Kuebler, B. L. Jolliff, and L. A. Haskin, Am. Mineral. **89**, 665 (2004).

28. I. Chourpa, L. Douziech-Eyrolles, L. Ngaboni-Okassa, J.-F. Fouquenet, S. Cohen-Jonathan, M. Soucé, H. Marchais, and P. Dubois, Analyst **130**, 1395 (2005).

29. N. J. Foster, M. J. Burchell, J. A. Creighton, M. J. Cole, and The United Kingdom Stardust Consortium, Lunar and Planetary Science **XXXIX**, 1759 (2008).

30. D. Bersani, P. P. Lottici, and A. Montenero, J. Raman Spectrosc. **30**, 355 (1999).

31. R. A. Goodall, J. Hall, H. G. M. Edwards, R. J. Sharer, R. Viel, and P. M. Fredericks, J. Archaeol. Sci. **34**, 666 (2007).

32. S. K. Sharma, P. G. Lucey, M. Ghosh, H. W. Hubble, and K. A. Horton, Spectrochim. Acta A **59**, 2391 (2003).

33. A. Wang, L. A. Haskin, and B. L. Jolliff, Lunar and Planetary Science **XXIX**, 1819 (1998).

34. W. Wang, J. Y. Howe, and B. Gu, J. Phys. Chem. C **112**, 9203 (2008).

35. J. H. Bang, and K. S. Suslick, J. Am. Chem. Soc. **129**, 2241 (2007).

36. M. X. Gu, L. K. Pan, B. K. Tay, and C. Q. Sun, J. Raman Spectrosc. **38**, 780 (2007).

37. N. J. Everall, J. Lumsdon, and D. J. Christopher, Carbon **29**, 2, 133 (1991).

38. C. Y. Xu, P. X. Zhang, and L. Yan, J. Raman Spectrosc. **32**, 862 (2001).

39. G. Yang, P. Biswas, P. Boolchand, and A. Sabata, J. Am. Ceram. Soc. **82**, 10, 2573 (1999).

40. W. B. White, J. Ceram. Process. Res. **6**, 1, 1 (2005).

41. B. Wopenka, R. Popelka, J. D. Pasteris, and S. Rotroff, Appl. Spectrosc. **56**, 10, 1320 (2002).

# Chapter 5: In-flight Charging of Natural Light-Harvesting Complexes by Aerosol Methodologies

**5.1 Abstract**

Natural photosynthetic antenna complexes have remarkable energy collection efficiencies and the capability of absorbing light in the near infrared regime; hence they have potential applications in photovoltaics. Researchers have characterized the size and shape of the antennae with microscopy techniques, which often need additional sample preparation procedures. Aerosol scientists routinely disperse highly charged particles into the gas-phase for sequential size characterization, if the charge is reduced, and for film fabrication, if an electrode is placed in the path of a charged aerosol. However, the efficacy of such aerosol methods has not been demonstrated with natural photosynthetic antenna complexes. Here we present for the first time size and charge distribution measurements on three different light harvesting (LH) complexes that range widely in size and solubility with standard aerosol techniques, electrospray and nebulization. While electrospray is known for generating highly charged particles, we found that aerosols of antenna complexes produced with nebulization carried multiple charges. Our approaches for generating charged aerosols of photosynthetic antenna complexes have applicability in the sequential deposition of components for designing nanostructured biohybrid photovoltaic devices.

**5.2 Introduction**

Green and purple bacteria have pigment-protein complexes to efficiently harvest sunlight even in environments with low-illumination and relative high temperature conditions. For instance, in green bacteria such complexes are self-assembled into an antenna-like configuration, which collect the energy from the photons and funnel it, by a fluorescence resonance energy transfer (FRET) mechanism, to a reaction center embedded in the cytoplasmic membrane, where the energy is stored and charge separation occurs[1,2]. Developments in the understanding of the light-harvesting processes occurring in bacteria[3-10] has bolstered the use of natural photosynthesis as the blueprint for designing more efficient photovoltaic devices[11]. The efficiency of energy transfer in LH complex relies on an intricate balance of pigment orientation and spatial organization to minimize excitation losses by radiative pathways before they are stored.

The characterization of natural photosynthetic antenna complexes is key to decipher the energy transfer process within the antennae and to effectively implement them in functional nanostructures. Biologists and chemists perform size and morphological characterizations of natural light-harvesting complexes mainly with microscopy techniques[12-18]. While these methodologies provide a graphical description of the light-harvesting complexes, they require several steps in preparing the sample to avoid physical degradation or chemical transformation during the analyses. Moreover, in microscopy methods the particle size distribution has to be obtained by counting the number of antennae in several images. Aerosol scientists use electrical mobility analysis[19-21] as a standard tool to measure the particle size distribution of aerosols with sizes in the nanometer and submicrometer ranges. The procedure requires three

sequential steps, 1 - generating an aerosol of the sample, 2 - passing the aerosol particles through a neutralizer, and 3 - classifying the neutralized particles on the basis of their electrical mobility (Figure 5-1).
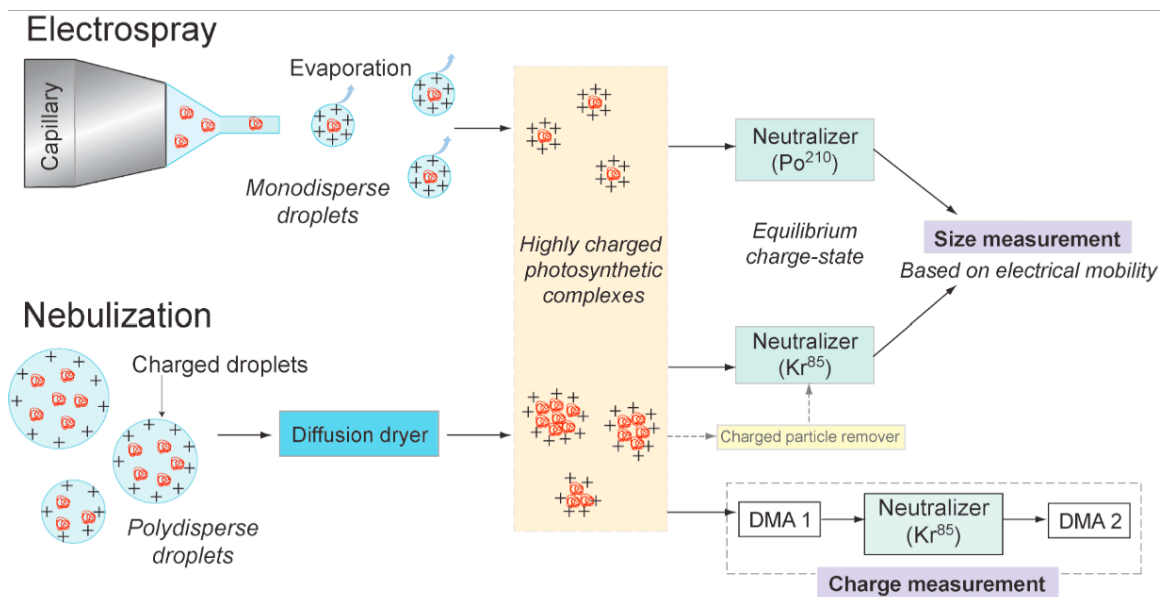


**Figure 5-1:** Aerosolization, charging, and characterization of photosynthetic antenna complexes.

The aerosolization step may be performed with various techniques including electrospray and nebulization. In electrospray a liquid is fed through a capillary connected to a high voltage source, which creates an electric field gradient between the capillary and a grounded counter electrode. As we increase the electric potential, the liquid at the capillary tip takes a conical shape, a Taylor cone, and emits a liquid jet that later breaks into charged droplets because of viscous instabilities in the liquid. The charged droplet undergoes evaporation and a series of fissions that generate smaller droplets[22]. This evaporation-fission cycle repeats until the solvent evaporates completely.

Electrospray has the particularity of generating highly charged, monodispersed droplets with controllable size in the submicrometer range[23]. In nebulization, an air jet collides with a liquid stream that breaks the liquid into droplets, and then an air flow carries smaller droplets away while larger droplets are collected in a reservoir and recirculated. In contrast to electrospray, which involves electrical and mechanical forces, nebulization is purely a mechanical process that generates polydisperse droplets in the micrometer range[24,25]. The second step, neutralization, is needed because aerosolization methods produce multiply charged droplets, which then transfer the charge to the particles enclosed in them. Because the electrical mobility technique performs better with singly charged particles, we need to expose charged particles to a bipolar ion environment, generated with $Kr^{85}$ or $Po^{210}$ sources, where they acquire a theoretically known equilibrium charge-state. In such equilibrium charge-state a Boltzmann distribution function describes the probability that a particle of a given size carries charge, and the chances are higher for singly charged particles. In the third step, we classify particles on the basis of their electrical mobility ($Z_p$), which is a function of the particle size and charge-state[26]; $Z_p = neC_c/3\pi\mu D_p$, where $n$ is the number elementary charges on a particle, $e$ is the electron elementary charge, $C_c$ is the slip correction factor, $\mu$ is the viscosity of the gas, and $D_p$ is the particle mobility diameter. For spherical or low-aspect ratio (< 2) particles, the mobility diameter is the same as the sphere diameter. If we know the particle electrical mobility and the charge-state (i.e., singly charged) we can readily calculate the particle size. In aerosol science, we typically use a differential mobility analyzer (DMA) to classify particles based on their electrical mobilities. The DMA is analogous to a mass spectrometer but using electrical mobility instead of mass and details

of its functioning have been described elsewhere[19]. While size distribution measurements require charge neutralization, the retention of high charging of light-harvesting complexes could be an advantage for collecting them onto substrates, with electric fields, and forming functional films[11,27].

In-flight charging of natural photosynthetic antenna complexes has potential applications for designing nanostructured biohybrid photovoltaic devices. The deposition method, however, must facilitate immobilization of light-harvesting structures onto substrates with functional and sometimes complex morphologies including rod-like, columns, and porous structures[11,27,28]. Thus, the random Brownian motion of particles must be suppressed to manipulate the particles and target a specific deposition location. While liquid-phase deposition techniques such as spin or dip coatings are flexible and simple[29,30], they are not suitable to fabricate multi-layered structures when a solvent is incompatible with a previously deposited material[11,31]. Alternatively, we may deposit dried, charged materials using electric fields driven by electrophoresis, which is a process used by aerosol scientists to synthesize porous nanostructured films[27,32,33], to collect powders from flame and furnace reactors[34,35], to sample particulate matter in the atmosphere[36], and to remove particulate pollutants from the gas-phase[24,37]. The procedure is a one-step method that involves aerosolization, charging and drying in-flight, and deposition.

The present work investigated the aerosol characteristics of three natural antenna complexes namely, chlorosomes from the green filamentous bacterium *Chloroflexus aurantiacus*, the Fenna-Matthews-Olson (FMO) antenna complex from the green sulfur bacterium *Chlorobium tepidum*, and the light-harvesting 2 (LH2) complex from purple

bacterium *Rodobacter sphaeroides* (Figure 5-1). Chlorosomes are supramolecular structures made of a lipid envelope containing bacteriochlorophyll (BChl) *c* molecules self-assembled into rod-like oligomers and a baseplate, located at the bottom of the chlorosome body[2,3]. The baseplate links the chlorosome with the reaction center in the cytoplasmic membrane. The FMO protein is a water-soluble antenna complex from green-sulfur bacteria[38-40]. The LH2 complex constitutes a membrane bound, peripheral light-harvesting antenna of purple bacteria[41,42]. We first aerosolized the LH complexes with two standard techniques, electrospray and nebulization, and then measured the size and charge-state of the aerosols of antenna complexes with electrical mobility analysis.

## 5.3 Materials and Methods

### 5.3.1 Materials

Chlorosomes from *Chloroflexus aurantiacus* were prepared as described previously[15]. FMO was purified from *Chlorobium tepidum* as described by Wen et al[38]. LH2 complexes were prepared from *Rhodobacter sphaeroides*. Briefly, whole membranes were solubilized by the addition of lauryldimethylamine-oxide (LDAO) to 1% with stirring for 60 minutes at 4 ˚C. The mixture was centrifuged at 200,000 x g for 1 hour. The supernatant was loaded to an Q-sepharose ion-exchange chromatography column and eluted with a linear gradient of NaCl. Appropriate fractions, as judged by the absorption spectrum, were pooled and concentrated and finally loaded to a superdex S200 gel filtration column that was equilibrated with 0.1% LDAO and 200 mM NaCl. Phosphate buffer solution (PBS) and hexanol saturated-PBS were prepared as described in Zhu et al[43]. For electrospray experiments all the antennae suspensions were diluted in a

20 mM ammonium acetate solution to increase the electrical conductivity and facilitate the electrospray in the cone-jet mode. For nebulization experiments, the antenna suspensions were diluted in pure water.

### 5.3.2 Electrospray experiments

Electrospray was performed with a commercial electrospray aerosol generator (EAG, TSI Inc., Model 3480). A 100 μm (inner diameter) silica fused capillary was used for suspensions of chlorosomes, and a 40 μm capillary was used for suspensions of the FMO and LH2 complexes. The EAG uses a total gas flow rate of 1.1 L min$^{-1}$ (i.e., 1.0 L min$^{-1}$ air + 0.1 L min$^{-1}$ $CO_2$) to carry the highly charged aerosol particles from the electrospray zone to a neutralization chamber. In the neutralization chamber highly charged aerosol particles were exposed to a bipolar ion environment, generated by a 5 mCi Po$^{210}$ neutralizer, with the objective of reducing their charge-state to the so-called Boltzmann equilibrium charge-state. Following charge neutralization, aerosol particles were sent to the sizing instrument to obtain the size distribution.

### 5.3.3 Nebulization experiments.

Suspensions of the photosynthetic antenna complexes were aerosolized using a bio aerosol nebulizing generator (BANG) unit[24,25] (CH Technologies Inc., USA). The BANG pulls out liquid from a container and impinges it with an air stream to generate droplets. Smaller droplets are carried out of the container by the air flow and large droplets fall back to the container. The airflow rate was set to 1.5 L min$^{-1}$. The liquid in

the container was recirculated by an external pump at 0.5 mL min$^{-1}$. The droplets were then passed through a diffusion dryer to evaporate the solvent, then the dried antenna complex aerosols were sent to the sizing instrument for size and charge characterization.

### 5.3.4 Size distribution measurements.

A scanning mobility particle sizer (SMPS) composed of an electrostatic classifier platform (TSI Inc., model 3080), a differential mobility analyzer (DMA, TSI Inc.), and a condensation particle counter (CPC, TSI Inc., model 3776) was used to obtain the particle size distributions. Note that the platform has a 2 mCi Kr$^{85}$ neutralizer built-in, and in electrospray experiments the Kr$^{85}$ source was bypassed because the EAG has one Po$^{210}$ neutralizer incorporated. A DMA model 3081 was used for size distribution measurements of chlorosomes and a model 3085 for FMO and LH2 complexes. The aerosol and sheath flow rates in the 3081 DMA were set at 0.3 L min$^{-1}$ and 6 L min$^{-1}$, respectively; and in the 3085 DMA they were set at 1.5 L min$^{-1}$ and 20 L min$^{-1}$. Particle size distribution data was acquired with a commercial software (TSI Inc.).

### 5.3.5 Charge distribution measurements

Two DMAs, with their respective platforms, were connected in series (tandem DMA). The first DMA was used to select particles of a specific electrical mobility (i.e., a specific diameter), by selectively varying the applied voltage, and the second DMA was used to scan over a range of electrical mobilities and obtain a distribution. In these

experiments, the aerosol particles were passed through a bipolar ion environment, generated with a $Kr^{85}$ neutralizer that was placed between the two DMAs.

## 5.4 Results and Discussion

### 5.4.1 Single units of light-harvesting complexes isolated with an electrospray

We measured the size of the natural photosynthetic antenna complexes by isolating single units in charged droplets. The generated aerosol particles of the three complexes were passed through a $Po^{210}$ neutralizer to reduce their charge-state to the Boltzmann equilibrium state (see Figure 5-1). We detected size variation of chlorosomes induced by the solvent chemistry, identified the size of the FMO complex, and measured the size of the single LH2 complex. The corresponding particle size distributions are shown in Figure 5-2. We suspended chlorosomes in a phosphate buffer solution (PBS) and in hexanol-saturated PBS following a procedure by Zhu et al[43] to identify size variation of chlorosomes induced by alcohol chains. For these experiments we generated charged droplets with an initial diameter of 3.4 μm, as calculated with the scaling laws of electrospray[22,23,44,45]. We found the average width of the chlorosomes electrosprayed from PBS to be 24 nm. Such value matched the result of our previous work on chlorosomes suspended in pure water[11] using the same aerosol technique and the reports by other authors using microscopy techniques[3,12,15,46,47]. In contrast to chlorosomes in PBS, the mean mobility diameter of chlorosomes electrosprayed from hexanol-saturated PBS increased from 24 nm to approximately 60 nm. However, when we added fresh PBS to chlorosomes suspended in hexanol-saturated PBS (post-hexanol) and measured their

size in the aerosol, we observed a decrease in the particle diameter from 60 nm to 30 nm. The size distribution showed a small peak at approximately 20 nm, which most probably originated from phosphate buffer residues in droplets that did not contain chlorosomes. In electrospray of solutions, the ultimate particle size depends on the solute concentration and the droplet fission dynamics. These residual particles did not appear in the size distribution of chlorosomes in hexanol saturated-PBS after addition of fresh PBS most probably because the concentration of chlorosomes was lower compared with the phosphate buffer concentration. Thus, the residuals formed larger particles that did not appear in the spectra. Our findings follow the same trend observed by Zhu et al[43] using microscopy and dynamic light scattering techniques. Hexanol penetrates through the lipid layer of the chlorosomes and disrupts the pigment-pigment interactions that hold the BChl *c* oligomers together. The formation of bacteriochlorophyll *c* monomers enlarged the chlorosomes, and after treatment with fresh PBS their size decreased to its original size[43].
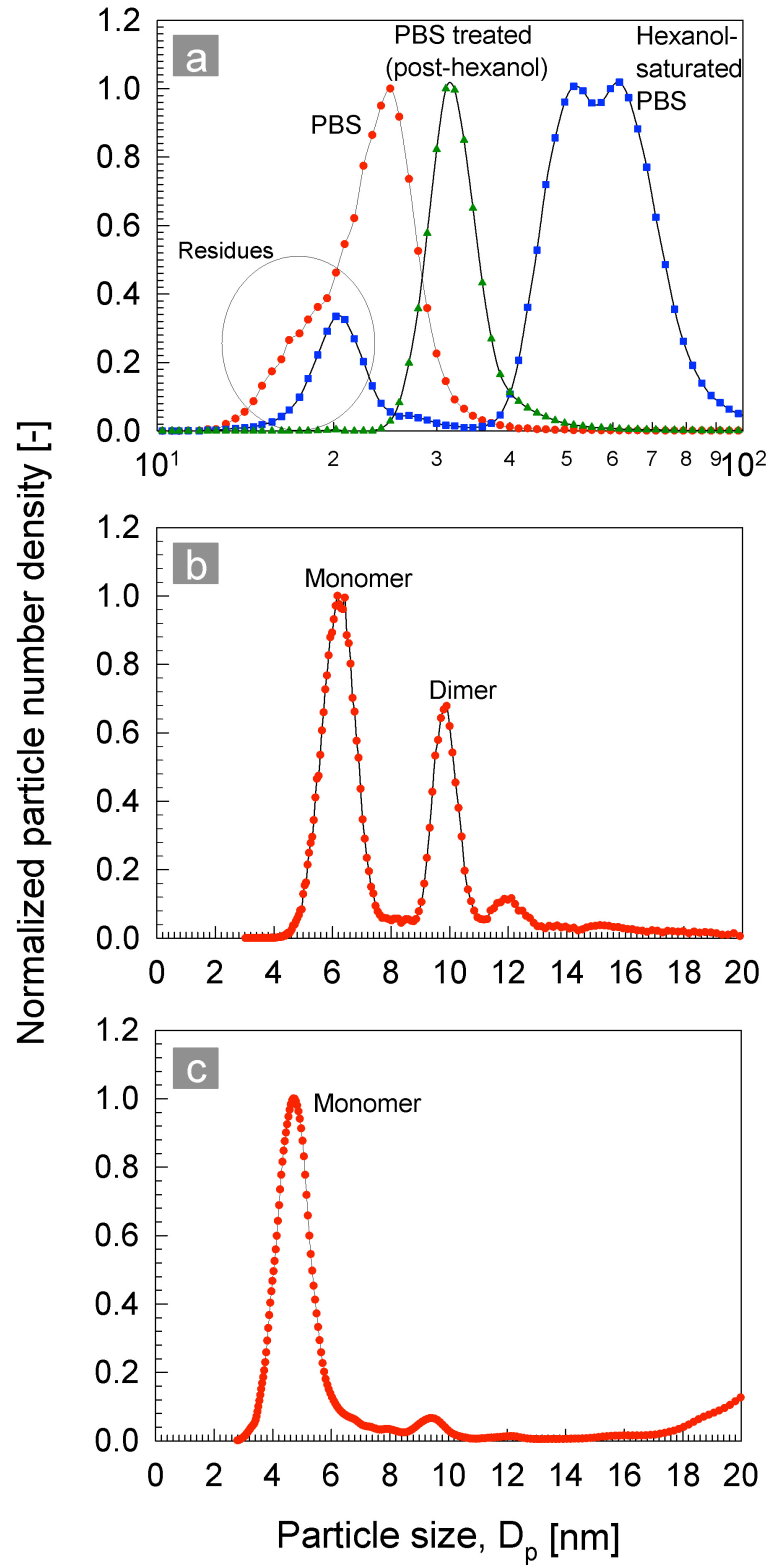
**Figure 5-2:** Size of single antenna units aerosolized with electrospray. (a) chlorosomes,

(b) FMO complex, and (c) LH2 complex.

The UV-visible light absorption spectra of the chlorosome suspensions (Figure 5-3) was also recorded and the characteristic peaks of the BChl *c* oligomers at 740 nm in PBS and BChl *c* monomers at 670 nm in hexanol saturated-PBS were observed. However, after treatment with fresh PBS, the light absorption spectra showed both a prominent peak of BChl *c* oligomers and small peak of Bchl *c* monomers. These results confirm that BChl *c* oligomers formed monomers upon dispersion in hexanol saturated-PBS, but the effect was reversable. Thus, they recovered their native light-harvesting properties after addition of fresh PBS. Nevertheless, the re-assembly did not occur completely and some monomers remained uncoupled in the chlorosome envelope, which seems to agree with the particle size measurements in which the width of the post-hexanol chlorosomes was slightly larger than in the native state. In addition, our measurements indicate that chlorosomes maintained their physical characteristics from the liquid-phase even after we dispersed them into aerosols.
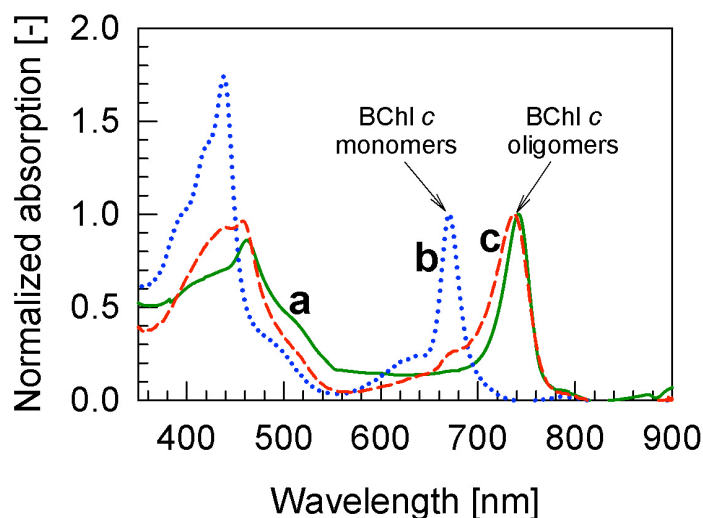


**Figure 5-3:** UV-visible absorption spectra of chlorosomes (a) in a phosphate buffer solution (PBS), (b) in hexanol-saturated PBS, and (c) in hexanol saturated-PBS after treatment with fresh PBS.

We then generated droplets with an initial mean diameter of 200 nm to disperse the FMO and the LH2 complexes into the gas-phase, because these two complexes have sizes significantly smaller than the chlorosomes. The FMO complex is a disc-like particle with a low aspect ratio of 1.6 composed by three identical subunits, arranged with a C3 symmetry axis perpendicular to the disc plane[38], and it is highly soluble in water. The minor and major axis diameters of a single FMO complex are 5 nm and 8 nm as measured by a crystallographic technique (PDB code: 3ENI, Figure 5-4). Thus the FMO mobility diameter was expected to fall within that range, likely close to 5 nm, because for low aspect ratio particles the mobility diameter is reported to be equivalent to the smaller diameter of the spheroid[11,48]. Here we identified the mobility diameter of a single FMO complex unit (i.e., a monomer of the complex unit) to be approximately 6.2 nm, slightly larger than the minor axis diameter (Figure 5-2). However, it is possible that in the highly charged, nanometer-sized droplet either water molecules adsorbed to the FMO protein given its high solubility in water or some of the tris-buffer precipitated around the complex, increasing its size. We also identified a second peak at 9.8 nm. We assigned the 9.8-nm peak to the agglomerates formed by two FMO complex units (i.e., a dimer of the complex unit). The height ratio of dimer to monomer peaks indicates that ~ 2/3 of the FMO complexes in the liquid dynamically interact with each other. The LH2 complex is a hollow cylinder with an outer diameter of 7 nm and a height of 4.5 - 5 nm (PDB code: 1NKZ, Figure 5-4). The particle size distribution of the LH2 complex (Figure 5-2) showed a single peak at ~ 4.6 nm, which is nearly the height of the hollow cylinder. These results demonstrate that electrospray facilitated the generation of individual units of the light-harvesting complexes, while still maintaining their physical characteristics.
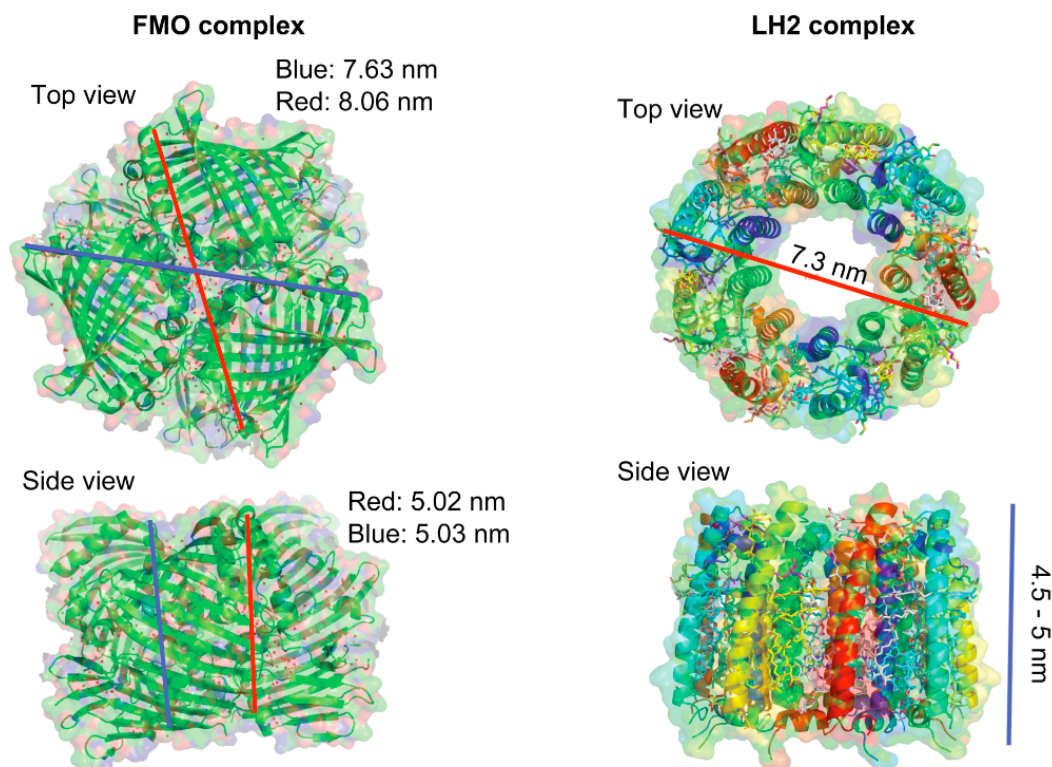
**Figure 5-4:** Morphology and dimensions of the FMO and LH2 complexes determined by crystallographic methods (PDB code: 3ENI and PDB code: 1NKZ, respectively).

Moreover, electrospray is an effective tool to generate multiply charged nanoparticles in a single-step. We found the number of elementary charges carried by the electrosprayed antennae[11,49], before neutralization with Po[210], to be +334, +8, +17, and +4 for the chlorosomes, the single FMO complex, the FMO complex dimer, and the LH2 complex, respectively. Those are remarkable charge values, difficult to obtain with other aerosol methods such as diffusion charging (i.e., the main charging mechanism of aerosol nanoparticles). Note that although other researchers have applied the electrospray and electrical mobility techniques to characterize viruses and proteins[48,50], this is the first report on the size of natural light-harvesting complexes using an aerosol technique. The charged light-harvesting complexes generated with an electrospray could also be

deposited ballistically targeting a specific deposition location, by suppressing the Brownian motion of particles, onto functional metal oxide semiconductor films to design biohybrid photovoltaic devices[11].

### 5.4.2 Multiple charging of light-harvesting complexes with nebulization

Multiple charged light-harvesting complexes were dispersed into the gas-phase with a standard nebulization technique.[24] Their size and charge distributions were measured with electrical mobility analysis. Droplets generated with a nebulizer have diameters in the micrometer range. Thus, they contain several units of the light-harvesting complexes per droplet. The particle size distributions of the nebulized LH complexes were measured after they reached the Boltzmann equilibrium charge-state in the $Kr^{85}$ neutralizer, labeled as total in Figure 5-5. In addition, we passed the LH complex aerosols through a charged particle remover (CPR) prior to charge neutralization. Thus, the size distributions measured after the CPR correspond to complexes carrying no charge (labeled as 0 charge).
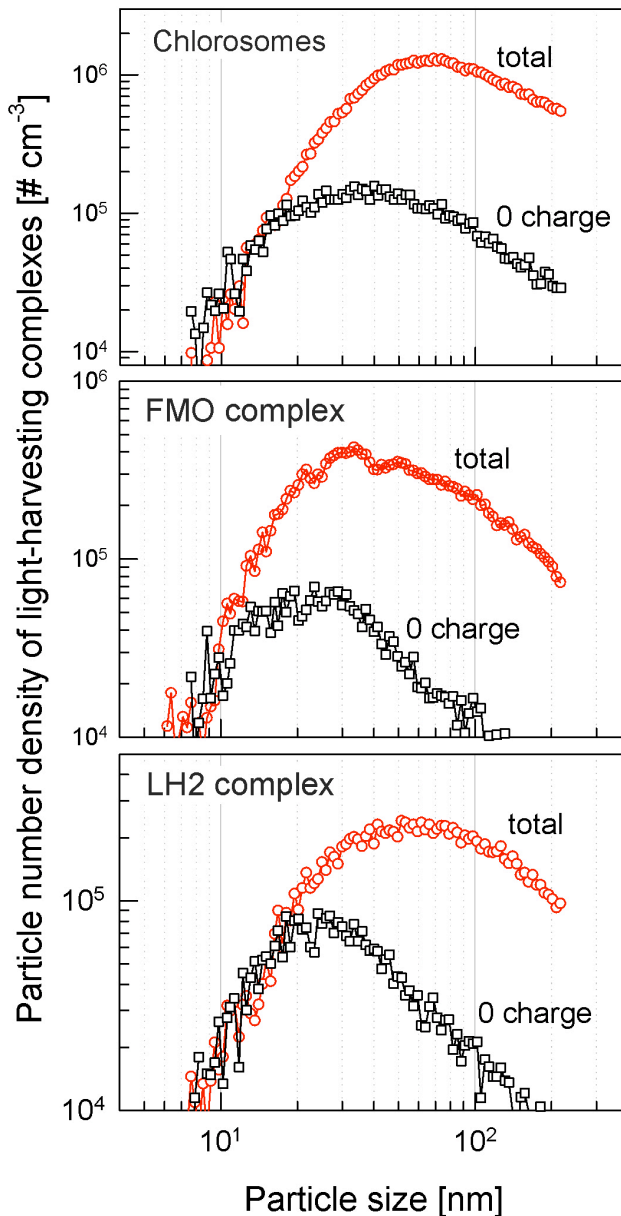
**Figure 5-5:** Particle size distribution of chlorosomes, FMO complexes, and LH2 complexes nebulized from aqueous suspensions.

The size range of the LH complexes aerosolized with the nebulizer had a geometric standard deviation of 2.0, indicating the polydisperse nature of the aerosols, and the geometric mean mobility diameters were approximately 60 nm, 40 nm, and 55 nm for chlorosomes, the FMO, and the LH2 complexes, respectively. Figure 5-5 also indicates

that clusters of chlorosomes, FMO, and LH2 smaller than 17 nm, 10 nm, and 18 nm, respectively were not charged because, below those diameters, particle number densities of the total aerosols match that of the 0-charge aerosols. Additionally, if we subtract the particle number density of the uncharged aerosols to that of total aerosols and divide it by the total number density at a particular size, we find that the total fraction of charged particles is higher at larger particle sizes. We expect more charges on bigger particles because they have more surface area available to allocate a larger number of elementary charges. Note that no electric field is involved in the aerosolization or drying processes. The charge on nebulized LH complexes may arise from two mechanisms. First, particles suspended in a liquid develop an electrical double layer around them, originated by both the surface charge of the particles and the ions present in the liquid. Second, when droplets are generated with a nebulizer, the mechanical forces that break the liquid surface induce charge on the droplets; this charge is then transferred to the light-harvesting complexes enclosed in the droplets. Thus, the charge on nebulized light-harvesting complexes is a contribution of both the particle electrical double layer in the liquid-phase and the aerosolization process. Our group and other authors[24,25] have observed charging of biological particles such as bacteria and viruses during nebulization. Mainelis et al[25] reported that micrometer-sized bacteria carried more than $1 \times 10^4$ charges, as a result of a nebulization process, and such value was higher than inorganic (NaCl) particles of comparable size. They attributed the higher number of charges to multiple protonation sites available on the surface of the bacteria, because the bacteria are composed of proteins and lipids[25]. Our data clearly indicates that the nebulized LH

complexes carry charge; however, Figure 5-5 does not show precisely what is the fraction of particles of a specific size carrying a certain number of elementary charges.

To quantify the number of charges carried by clusters of chlorosomes, FMO complexes, and LH2 complexes as a result of the aerosolization process, we measured the particle charge distribution using the electrical mobility technique with a tandem DMA system (i.e., two DMAs connected in series). Briefly, we selected particles with a given electrical mobility by fixing the voltage in the first DMA. However, since the electrical mobility is a function of particle size and charge (i.e., recall $Z_p = neC_c/3\pi\mu D_p$) it is possible that larger particles carrying multiple charges are classified at the mobility selected with DMA 1. To discern particles with varying size and charge but with the same $Z_p$ we need to pass the LH complex aerosols from DMA 1 through a $Kr^{85}$ neutralizer, where they acquire the Boltzmann equilibrium charge state. In the equilibrium charge-state it is reasonable to assume that most of the aerosol particles carry one charge, therefore their size can be readily differentiated with a second DMA. Thus the size distribution obtained with DMA 2 corresponds to particles having initially the same electrical mobility but not necessarily the same size and charge. For instance, to determine the fraction of singly charged 50-nm LH complexes, directly out of the nebulizer, we fix the voltage in DMA 1 to classify particles with an electrical mobility of 9.52 x $10^{-8}$ $m^2$ $V^{-1}$ $s^{-1}$ (corresponding to 50-nm particles with +1 charge); we then pass the aerosol particles through the $Kr^{85}$ source and finally we scan over ranges of electrical motilities with DMA 2. We then divide the particle number density at the 50-nm peak, in the distribution obtained with DMA 2, by the total number density of 50-nm particles (i.e., measured with one DMA as in Figure 5-5). To obtain the fraction of doubly charged

50-nm particles we now fix the voltage in DMA 1 to classify particles with an electrical

mobility of 1.9 x 10 $^{-7}$ m$^2$ V$^{-1}$ s$^{-1}$  (corresponding to 50-nm particles with +2 charges).

Again, we divide the number density of the 50-nm peak in the distribution from DMA 2

by the total number density of 50-nm particles. We repeated this procedure for LH

complex aerosol particles in the range of 25 nm to 200 nm carrying +1 to +4 elementary

charges. A detailed description on how to obtain the charge distribution of aerosols with

an electrical mobility technique has been reported elsewhere[20]. The charge distributions

of clusters of chlorosomes, the FMO complex, and the LH2 complex are shown in Figure

5-6.
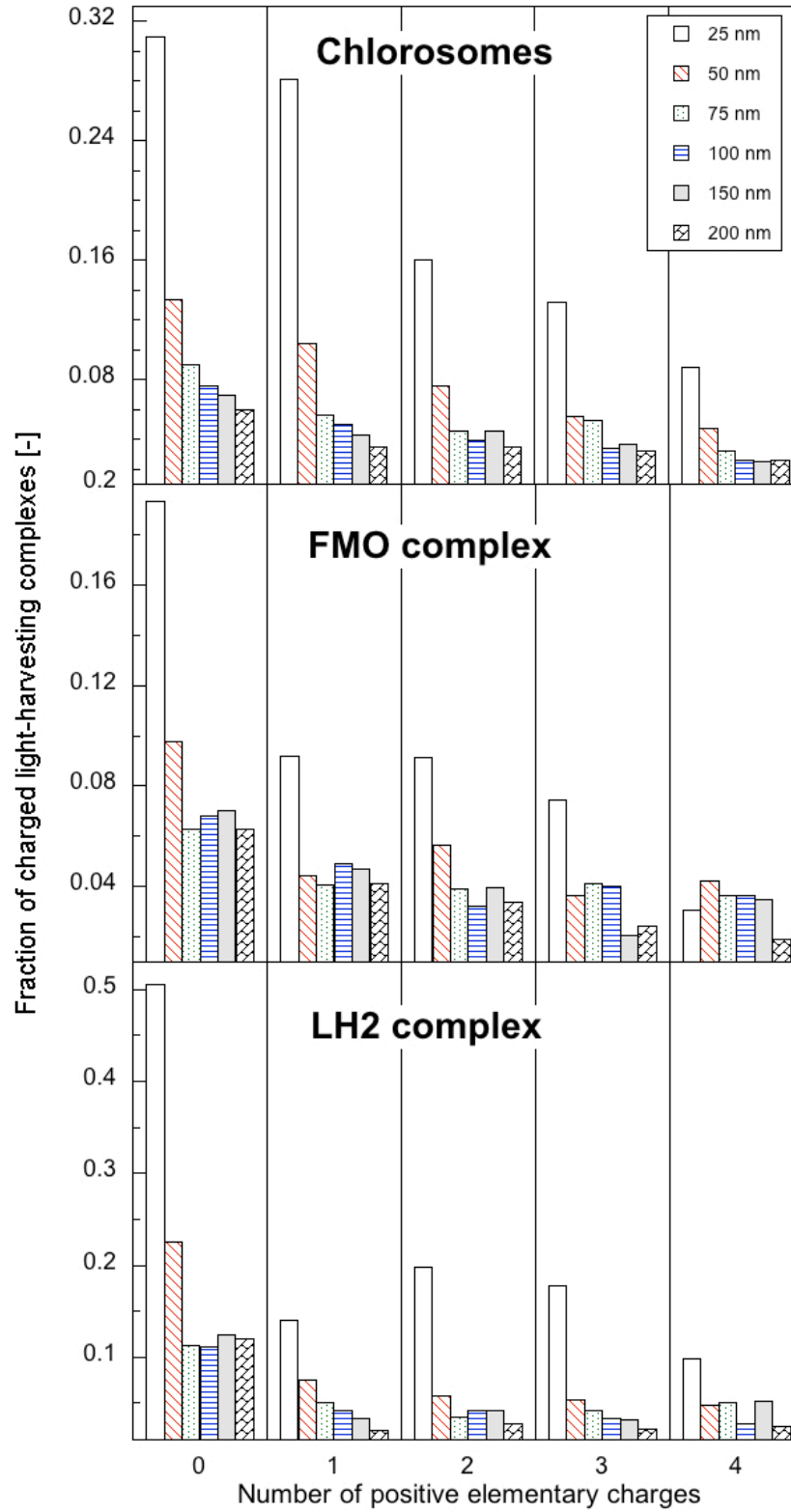
**Figure 5-6:** Charge distributions of antenna complex clusters measured with a tandem DMA system.

In the case of chlorosomes, the fraction of uncharged clusters decreased significantly from 0.30 at 25 nm to 0.13 at 50 nm and then it decreased gradually to 0.06 at 200 nm. The fraction of charged chlorosomes with +1 to +4 elementary charges decreased gradually with increasing the cluster size. Chlorosome clusters larger than 75 nm had a nearly constant fraction of +2 to +4 charges. Unlike chlorosomes where the trend of decreasing charge fraction as the clusters get bigger was clear, the FMO complex clusters showed an irregular charging pattern. The fraction of uncharged FMO complex was the highest at 25 nm, and it sharply decreased by more than half beyond that size and it remained constant at ~ 0.065 for clusters of 75 or larger. For charged FMO complexes, again 25-nm clusters had the highest fraction for +1 to +3 elementary charges compared with clusters of larger sizes. Charged FMO clusters with +1 to +4 charges showed a loose trend of decreasing fraction of charged complexes with increasing cluster size. Nevertheless, it appears as though the fractions of FMO clusters with +1 to +4 charges in the size range 50 nm - 150 nm remain constant. The fraction of charged 200-nm FMO clusters, however, decreases with increasing number of elementary charges. In the case of uncharged LH2 complexes, clusters of 25 nm had the highest fraction compared with clusters of larger sizes. The fraction of LH2 clusters carrying +1 to +3 charges decreased with increasing cluster size. The fraction of +4 charge seemed to be independent of cluster size. The irregular charging characteristics of the three LH complexes during the nebulization process may be associated with their surface characteristics. Chlorosomes are made of an envelope of lipid chains, with a hydrophilic head group and a hydrophobic hydrocarbon chain, thus they have well defined particle boundaries. Conversely, FMO and LH2 complexes are composed of proteins with loosely defined boundaries and

morphologies (see Figure 5-4); hence their surface area may vary significantly. Additionally, because those complexes do not have well defined boundaries they may interact with neighboring complexes in droplets.

The importance of aerosolization and charging in-flight of a variety of natural photosynthetic complexes resides in that the methodology does not damage the structure or functionality of biological complexes[11,24,50] and in that the charged complexes may be collected onto a number of substrates using electric fields. Having a strong electric field may effectively suppress the Brownian motion of particles, particularly in the nanometer regime[26,33], where such effect is predominant.

## 5.5 Conclusions

Standard aerosolization techniques combined with electrical mobility analysis allowed us to generate multiple charged aerosols of photosynthetic antenna complexes and to measure their size and charge-state.  The dimensions of the aerosolized LH complexes in the aerosols reflected their native state in the liquid-phase. We detected a three-fold enlargement in the width of chlorosomes from 24 nm to 60 nm, induced by the monomerization of the BChl *c* rod-like oligomers in hexanol-saturated PBS, and confirmed that BChl *c* molecules re-assembled into oligomers upon treatment with fresh PBS, which decreases the chlorosome size to ~ 30 nm, nearly their native state. We isolated individual units of the FMO and LH2 complexes in submicrometer-sized droplets, which allowed us to determine the size of single FMO and LH2 complexes and dimers of the FMO complex. We employed a conventional nebulization method to generate clusters of the antennae, which carried multiple charges. Knowledge of the

charge distribution of LH complexes is critical for functional film deposition by electrophoresis-driven methods. For instance, if we place a functional film with columnar or rod-like morphology in an electric field and feed charged LH complex aerosol particles perpendicularly onto the film, we may control the coating characteristics by tuning the potential gradient. More specifically, multiply charged particles would deposit on the top of the columns, because of their higher electrical mobility, while singly charged particle may deposit on the bottom part of the columns. The aerosolization and charging methodologies developed in this work can be readily generalized to other antenna complexes. Our approaches open the possibility to explore the design of functional light-harvesting films using natural antenna complexes, by sequential aerosolization, drying and charging in-flight, and deposition. Deposition of particles using electric fields is an effective method to suppress Brownian motion of particles and target a specific deposition location.

## 5.6 References

1.      Scholes, G. and Rumbles, G. Excitons in nanoscale systems. *Nat. Mater.* **5** (9), 683-696 (2006).

2.      Blankenship, R. E. *Molecular Mechanisms of Photosynthesis*. (Blackwell Science, Oxford, 2002).

3.      Blankenship, R. E., Olson, J. M., and Miller, M., in *Anoxygenic Photosynthetic Bacteria*, edited by R. E. Blankenship, M. T. Madigan, and C. E. Bauer (Kluwer Academic, Dordrecht, 1995), pp. 399-435.

4.    Bahatyrova, S. et al. The native architecture of a photosynthetic membrane. *Nature* **430** (7003), 1058-1062 (2004).

5.    Engel, G. S. et al. Evidence for wavelike energy transfer through quantum coherence in photosynthetic systems. *Nature* **446** (7137), 782-786 (2007).

6.    Fetisova, Z. G., Freiberg, A. M., and Timpmann, K. E. Long-range molecular order as an efficient strategy for light harvesting in photosynthesis. *Nature* **334** (6183), 633-634 (1988).

7.    Kuhlbrandt, W., Wang, D. N., and Fujiyoshi, Y. Atomic model of plant light-harvesting complex by electron crystallography. *Nature* **367** (6464), 614-621 (1994).

8.    Li, X. P. et al. A pigment-binding protein essential for regulation of photosynthetic light harvesting. *Nature* **403** (6768), 391-395 (2000).

9.    Peers, G. et al. An ancient light-harvesting protein is critical for the regulation of algal photosynthesis. *Nature* **462** (7272), 518-U215 (2009).

10.   Wilm, M. et al. Femtomole sequencing of proteins from polyacrylamide gels by nano-electrospray mass spectrometry. *Nature* **379** (6564), 466-469 (1996).

11.   Modesto-Lopez, L. B., Thimsen, E., Collins, A. M., Blankenship, R. E., and Biswas, P. Electrospray-assisted characterization and deposition of chlorosomes to fabricate a biomimetic light-harvesting device. *Energy Environ. Sci.* **3**, 216-222 (2010).

12.   Feick, R., Fitzpatrick, M., and Fuller, R. Isolation and characterization of cytoplasmic membranes and chlorosomes from the green bacterium Chloroflexus aurantiacus. *J. Bacteriol.* **150** (2), 905-915 (1982).

13.   Golecki, J. R. and Oelze, J. Quantitative relationship between bacteriochlorophyll content, cytoplasmic membrane-structure and chlorosome size in chloroflexus-aurantiacus. *Arch. Microbiol.* **148** (3), 236-241 (1987).

14.   Miller, M., Gillbro, T., and Olson, J. M. Aqueous aggregates of bacteriochlorophyll-c as a model for pigment organization in chlorosomes. *Photochem. Photobiol.* **57** (1), 98-102 (1993).

15.   Psencik, J. et al. Structure of chlorosomes from the green filamentous bacterium Chloroflexus aurantiacus. *J. Bacteriol.* **191** (21), 6701-6708 (2009).

16.   Qian, P. et al. A reaction center-light-harvesting 1 complex (RC-LH1) from a Rhodospirillum rubrum mutant with altered esterifying pigments. *J. Biol. Chem.* **278** (26), 23678-23685 (2003).

17.   Saga, Y., Shibata, Y., Itoh, S., and Tamiaki, H. Direct counting of submicrometer-sized photosynthetic apparatus dispersed in medium at cryogenic temperature by confocal laser fluorescence microscopy: Estimation of the number of bacteriochlorophyll c in single light-harvesting antenna complexes chlorosomes of green photosynthetic bacteria. *J. Phys. Chem. B* **111** (43), 12605-12609 (2007).

18.   Scheuring, S., Reiss-Husson, F., Engel, A., Rigaud, J. L., and Ranck, J. L. High-resolution AFM topographs of Rubrivivax gelatinosus light-harvesting complex LH2. *EMBO J.* **20** (12), 3029-3035 (2001).

19.   Knutson, E. O. and Whitby, K. T. Aerosol classification by electric mobility: Apparatus, theory, and applications. *J. Aerosol Sci.* **6**, 443-451 (1975).

20.    Kim, S. H., Woo, K. S., Liu, B. Y. H., and Zachariah, M. R. Method of measuring charge distribution of nanosized aerosols. *J. Colloid Interf. Sci.* **282** (1), 46-57 (2005).

21.    Tsai, D. H., Pease, L. F., Zangmeister, R. A., Tarlov, M. J., and Zachariah, M. R. Aggregation kinetics of colloidal particles measured by gas-phase differential mobility analysis. *Langmuir* **25** (1), 140-146 (2009).

22.    de la Mora, J. F. On the outcome of the coulombic fission of a charged isolated drop. *J. Colloid Interf. Sci.* **178** (1), 209-218 (1996).

23.    Rosell-Llompart, J. and de la Mora, J. F. Generation of monodisperse droplets 0.3 to 4 μm in diameter from electrified cone-jets of highly conducting and viscous-liquids. *J. Aerosol Sci.* **25** (6), 1093-1119 (1994).

24.    Kettleson, E. M. et al. Airborne virus capture and inactivation by an electrostatic particle collector. *Environ. Sci. Technol.* **43** (15), 5940-5946 (2009).

25.    Mainelis, G. et al. Electrical charges on airborne microorganisms. *J. Aerosol Sci.* **32** (9), 1087-1110 (2001).

26.    Hinds, W. C. *Aerosol Technology*. (John Wiley & Sons, New York, 1999).

27.    Modesto-Lopez, L. B., Pasteris, J. D., and Biswas, P. Sensitivity of micro-Raman spectrum to crystallite size of electrospray-deposited and post-annealed films of iron-oxide nanoparticle suspensions. *Appl. Spectr.* **63** (6), 627-635 (2009).

28.    An, W.-J., Thimsen, E. J., and Biswas, P. Aerosol-chemical vapor deposition method for synthesis of nanostructured metal oxide thin films with controlled morphology. *J. Phys. Chem. Lett.* **1** (1), 249-253 (2010).

29.    Ogi, T., Modesto-Lopez, L. B., Iskandar, F., and Okuyama, K. Fabrication of a large area monolayer of silica particles on a sapphire substrate by a spin coating method. *Colloids Surf. A* **297** (1-3), 71-78 (2007).

30.    Iskandar, F., Iwaki, T., Toda, T., and Okuyama, K. High coercivity of ordered macroporous FePt films synthesized via colloidal templates. *NANO Lett.* **5** (7), 1525-1528 (2005).

31.    Sridharan, A., Muthuswatriy, J., LaBelle, J. T., and Pizziconi, V. B. Immobilization of functional light antenna structures derived from the filamentous green bacterium Chloroflexus aurantiacus. *Langmuir* **24** (15), 8078-8089 (2008).

32.    Hogan, C. J. and Biswas, P. Porous film deposition by electrohydrodynamic atomization of nanoparticle sols. *Aerosol Sci. Tech.* **42** (1), 75-85 (2008).

33.    Kulkarni, P. and Biswas, P. Morphology of nanostructured films for environmental applications: Simulation of simultaneous sintering and growth. *J. Nanopart. Res.* **5** (3-4), 259-268 (2003).

34.    Basak, S., Rane, K. S., and Biswas, P. Hydrazine-assisted, low-temperature aerosol pyrolysis method to synthesize gamma-Fe2O3. *Chem. Mater.* **20** (15), 4906-4914 (2008).

35.    Karthikeyan, J. et al. Nanomaterial powders and deposits prepared by flame spray processing of liquid precursors. *Nanostruc. Mater.* **8** (1), 61-74 (1997).

36.    Dixkens, J. and Fissan, H. Development of an electrostatic precipitator for off-line particle analysis. *Aerosol Sci. Tech.* **30** (5), 438-453 (1999).

37.    Zhuang, Y., Kim, Y. J., Lee, T. G., and Biswas, P. Experimental and theoretical studies of ultra-fine particle behavior in electrostatic precipitators. *J. Electrostat.* **48** (3-4), 245-260 (2000).

38.    Wen, J. Z., Zhang, H., Gross, M. L., and Blankenship, R. E. Membrane orientation of the FMO antenna protein from Chlorobaculum tepidum as determined by mass spectrometry-based footprinting. *P. Natl. Acad. Sci. USA* **106** (15), 6134-6139 (2009).

39.    Li, Y. F., Zhou, W. L., Blankenship, R. E., and Allen, J. P. Crystal structure of the bacteriochlorophyll a protein from Chlorobium tepidum. *J. Mol. Biol.* **271** (3), 456-471 (1997).

40.    Tronrud, D. E., Wen, J. Z., Gay, L., and Blankenship, R. E. The structural basis for the difference in absorbance spectra for the FMO antenna protein from various green sulfur bacteria. *Photosyn. Res.* **100** (2), 79-87 (2009).

41.    Hong, X., Weng, Y., and Li, M. Determination of the topological shape of integral membrane protein light-harvesting complex LH2 from photosynthetic bacteria in the detergent solution by small-angle X-ray scattering. *Biophys. J.* **86** (2), 1082-1088 (2004).

42.    Moulisová, V. et al. Low light adaptation: energy transfer processes in different types of light harvesting complexes from Rhodopseudomonas palustris. *Biophys. J.* **97** (11), 3019-3028 (2009).

43.    Zhu, Y. W., Ramakrishna, B. L., vanNoort, P. I., and Blankenship, R. E. Microscopic and spectroscopic studies of untreated and hexanol-treated

chlorosomes from Chloroflexus aurantiacus. *Biochim. Biophys. Acta* **1232** (3), 197-207 (1995).

44.    Chen, D.-R., Pui, D., and Kaufman, S. Electrospraying of conducting liquids for monodisperse aerosol generation in the 4 nm to 1.8 μm diameter range. *J. Aerosol Sci.* **26** (6), 963-977 (1995).

45.    Chen, D.-R. and Pui, D. Y. H. Experimental investigation of scaling laws for electrospraying: Dielectric constant effect. *Aerosol Sci. Tech.* **27** (3), 367-380 (1997).

46.    Martinez-Planells, A. et al. Determination of the topography and biometry of chlorosomes by atomic force microscopy. *Photosyn. Res.* **71** (1-2), 83-90 (2002).

47.    Mimuro, M. et al. Excitation energy transfer in the green photosynthetic bacterium Chloroflexus aurantiacus: A specific effect of 1-hexanol on the optical properties of baseplate and energy transfer processes. *Photosyn. Res.* **48** (1-2), 263-270 (1996).

48.    Allmaier, G., Laschober, C., and Szymanski, W. Nano ES GEMMA and PDMA, new tools for the analysis of nanobioparticles—protein complexes, lipoparticles, and viruses. *J. Am. Chem. Soc. Mass Spectrom.* **19** (8), 1062-1068 (2008).

49.    Suh, J., Han, B., Okuyama, K., and Choi, M. Highly charging of nanoparticles through electrospray of nanoparticle suspension. *J. Colloid Interf. Sci.* **287** (1), 135-140 (2005).

50.    Hogan, C. J., Kettleson, E. M., Ramaswami, B., Chen, D. R., and Biswas, P. Charge reduced electrospray size spectrometry of mega- and gigadalton

complexes: Whole viruses and virus fragments. *Anal. Chem.* **78** (3), 844-852 (2006).

# Chapter 6: Electrospray-Assisted Characterization and Deposition of Chlorosomes to Fabricate a Biohybrid Photovoltaic Device

**6.1 Abstract**

Photosynthesis is an efficient process by which solar energy is converted into chemical energy. Green photosynthetic bacteria such as *Chloroflexus aurantiacus* have supramolecular antenna complexes called chlorosomes attached to their cytoplasmic membrane that increase the cross section for light absorption even in low-light conditions. Self-assembled bacteriochlorophyll pigments in the chlorosome interior play a key role in the efficient transfer and funneling of the harvested energy. In this work it was demonstrated that chlorosomes can be rapidly and precisely size-characterized online in real time using an electrospray-assisted mobility-based technique. They can be electrospray-deposited onto $TiO_2$ nanostructured films with columnar morphology to fabricate a novel biomimetic device and effectively harvest sunlight. It was shown that the presence of chlorosomes in the device had a 30-fold increase in photocurrent.

**6.2 Introduction**

Solar energy is a plentiful resource distributed over the surface of the earth and it is already used to generate electricity through photovoltaic devices. In recent years, dye-sensitized solar cells (DSSCs) based on a metal oxide film[1], typically a titanium dioxide ($TiO_2$) nanostructured thin film, have been increasingly investigated to overcome the high-cost of fabrication of silicon-based photovoltaic devices. Key challenges for these DSSCs reside in increasing the photon collection efficiency over a broad spectrum of wavelengths in the visible regime, and in retarding the charge recombination process. In our previous studies, a $TiO_2$ nanostructured film with columnar morphology[2] was observed to be more efficient both in preventing the electron-hole recombination process and in enhancing the electron transport across the film than a granular morphology in a DSSC. A $TiO_2$ film made of vertically aligned nanostructured columns results in higher interfacial area between the hole carrier (an electrolyte or a conductive polymer) and the electron acceptor ($TiO_2$) materials with highly-efficient electron transport properties.

When it comes to solar energy harvesting, nature provides valuable knowledge of the materials, of their functionality, and of the assembly mechanisms to produce efficient light-harvesting structures such as the ones found in plants and photosynthetic bacteria. A novel approach to develop light-harvesting devices to generate electricity, based on the concept of biomimetics, is to combine engineered nanostructured $TiO_2$ films having an efficient electron transport morphology, nano-columns or nano-wires, with robust natural light-harvesting supramolecular structures. The concept for the fabrication of a biomimetic light-harvesting device, which uses chlorosomes extracted from the green

photosynthetic bacterium *Chloroflexus aurantiacus* as light-harvesting supramolecular structures, is illustrated in Figure 6-1(a).
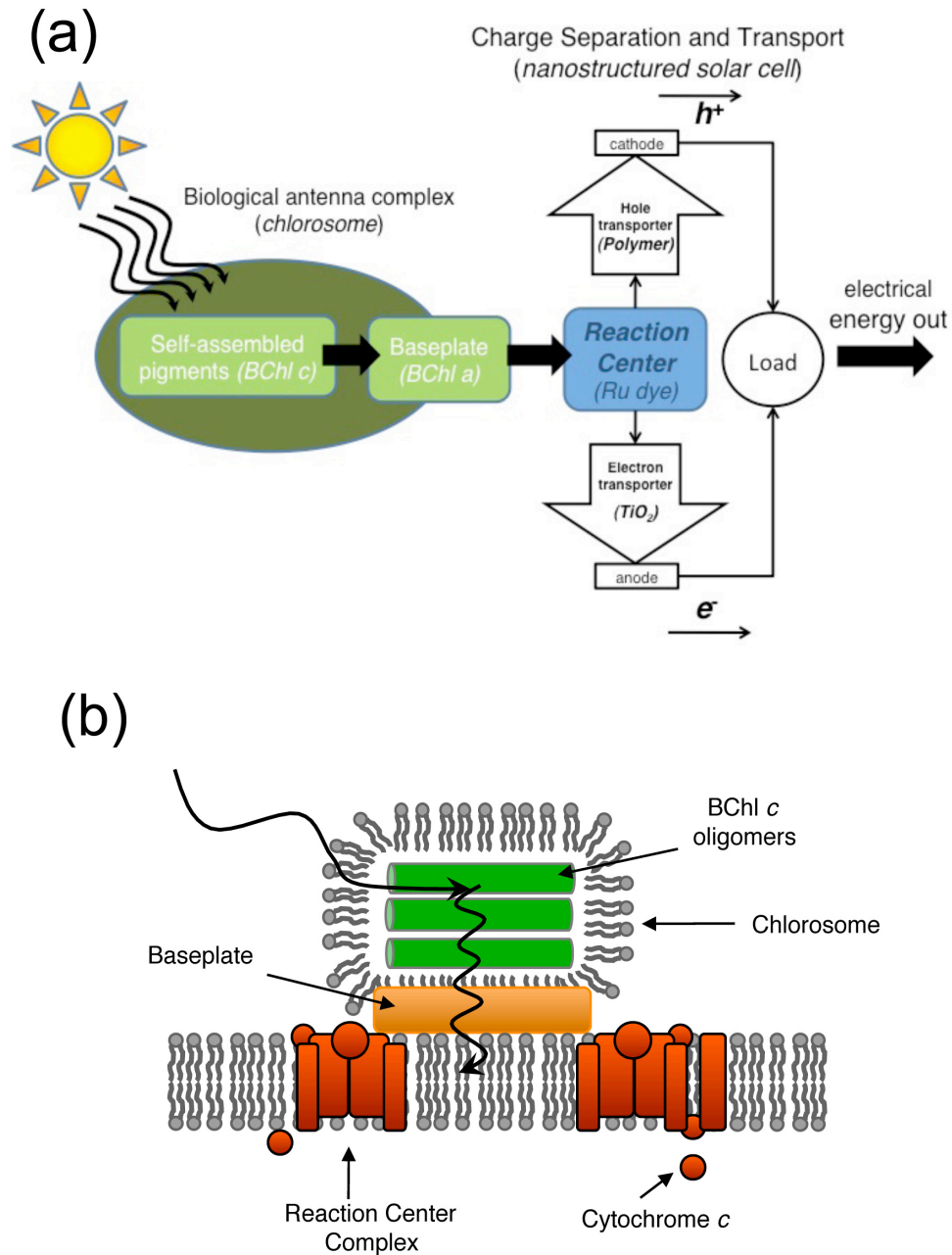


**Figure 6-1:** (a) Illustration of the concept of a biomimetic hybrid device to harvest sunlight and structure of the chlorosome. (b) Cartoon showing the structure of chlorosomes in the green photosynthetic bacteria.

Chlorosomes are large ellipsoidal bodies made of an envelope of proteins and lipids that enclose both carotenoids and oligomers of self-assembled bacteriochlorophyll (BChl) *c* molecules (Figure 6-1(b)). Chlorosomes are attached to the cytoplasmic cell membrane by the so-called baseplate complex, which contains BChl *a* pigments and it also serves as an intermediary in energy transfer between BChl *c* oligomers in the chlorosome and the membrane. Excitation absorbed by the chlorosome is ultimately used by a reaction center (RC) to facilitate electron transfer and generate a proton gradient across the membrane. Chlorosomes have drawn attention for applications in photovoltaics because of the effective natural organization of bacteriochlorophylls in the antenna, which provides optimal light collection and energy funneling[3, 4]. When chlorosomes are extracted from the organism, however, the RC remains in the membrane[5]. A dye molecule that absorbs light in the same range as the BChl *a* in the natural RC (absorbance = 865 nm) could be used as a substitute to promote excitonic energy transfer and subsequent charge separation in the nanostructured solar cell. In the biomimetic light-harvesting device proposed in this work (see Figure 6-1(a)) photons are absorbed by the chlorosomes, which are deposited onto a dye-chemisorbed $TiO_2$ film by an noninvasive method, and funneled by a fluorescence resonance energy transfer (FRET) mechanism to the dye molecule that serves as an artificial reaction center. When the excitonic energy reaches the dye, charge separation occurs that results in the injection of electrons into $TiO_2$ nanostructured columns and holes into a conductive polymer film, thereby resulting in the generation of electricity.

The diffusion length of the electron-hole pair, or exciton, in chlorosomes strongly depends on their size and on the amount of BChl *c* content[6]. Therefore, size

characterization of chlorosomes is an important aspect for the effective application of these antenna complexes in photovoltaics. Current microscopy techniques for characterization often require complex protocols and the size distribution is generally obtained by visual inspection and direct count of the chlorosomes in several images. An attractive alternative for a rapid and precise size characterization of chlorosomes is the charge-reduced electrospray mobility analysis [7-9]. By electrospraying, a method of liquid atomization that generates multiply charged particles, single chlorosomes can be aerosolized and after adequate charge neutralization, their size distribution can be precisely measured online, in real time, using an electrical mobility-based technique [10]. Furthermore, the electrospray is an elegant solvent-free deposition technique that allows for a one-step deposition method of chlorosomes (and other bio-particles), without modifying their structure or functionality [7, 8], onto a grounded substrate with near 100 % deposition efficiency [11]. For the fabrication of the biomimetic device the electrospray-deposition technique is highly preferred to avoid undesired contact of solvents with the components of the device. Since the presence of water in which the chlorosomes are dispersed may cause the dye to desorb from the surface of the $TiO_2$ columns, it is essential to deposit the chlorosomes by a method that allows the water to evaporate without making contact with the dye. Furthermore, because the electrosprayed chlorosomes are multiply charged, they can be deposited ballistically allowing penetration to the lower part of the $TiO_2$ columns by overcoming the hindrance effect caused by the columns themselves as in other aerosol deposition methods where Brownian motion and chlorosome-column interactions may dominate. Subsequently, a hole-carrier polymer must be deposited onto the chlorosomes to enhance charge

separation and prevent electron-hole recombination, and this step must be solvent-free to prevent the BChl *c* oligomers from denaturing when they come into contact with the organic solvent.

In this work, the size distribution of chlorosomes from *C. aurantiacus* was investigated by electrospray-assisted mobility analysis. Furthermore, the use of electrospray to deposit intact chlorosomes and a conductive polymer onto a $TiO_2$ nanostructured film with columnar morphology was studied. Finally, a biomimetic light-harvesting device was fabricated by incorporating intact chlorosomes into a DSSC.

## 6.3 Experimental Section

### 6.3.1 Materials

Chlorosomes were extracted[12] from the green bacterium *Chloroflexus aurantiacus* and dispersed in pure water and in a buffer solution for size distribution and deposition experiments, respectively. A 0.33 mM solution of tris(isothiocyanato)-ruthenium(II)-2,2':6',2"-terpyridine-4,4',4"-tricarboxylic acid, tris-tetrabutylammonium salt (Black dye; 620-1H3TBA, Solaronix, Aubonne, Switzerland) was prepared in anhydrous ethanol. Conductive p-type polymer poly(3-octylthiophene-2,5-diyl) (P3OT) was obtained from Sigma-Aldrich (St. Louis, MO, USA) and dissolved in toluene to a concentration of 10 mg/mL. Indium tin oxide (ITO)-coated glass slides were purchased from Delta Technologies (Stillwater, MN, USA) and used after cleaning them with ethanol.

6.3.2 Electrospray-Assisted Characterization of Chlorosomes

A syringe pump was used to feed a chlorosome suspension through a stainless steel capillary needle with an inner diameter of 160 μm at a flow rate of 1 μL min$^{-1}$. A high-voltage power supply was connected to the capillary, and a positive potential of > 4 kV was applied for cone-jet formation at the capillary outlet [11]. The needle was set inside a closed chamber, and particle-free $CO_2$ gas was introduced at a rate of 0.3 L min$^{-1}$. The $CO_2$ gas was used to prevent the formation of corona discharge at the tip of the capillary needle, due to the high surface tension of water, and to carry the aerosol particles to the sizing instrument. After the electrospray generation, the highly charged aerosol particles were passed through a bipolar neutralizer ($Po^{210}$) to reduce the number of charges and bring them to an equilibrium charging state. The neutralizer was placed at the exit of the chamber to minimize loss of chlorosomes due to deposition onto system walls by the external electric field. Mobility-based real-time particle size distribution measurements were carried out using an electrostatic classifier (TSI Inc., Model 3080) and a long differential mobility analyzer (DMA, TSI Inc., Model 3081), which classifies particles according to their electrical mobility, coupled with an ultrafine condensation particle counter (UCPC, TSI Inc., Model 3025A), which gives the number concentration of particles classified by the DMA. The particles' electrical mobility is dictated by the particle size and charge; a more detailed description of the principle of functioning of the DMA can be found elsewhere [10].

6.3.3 Biomimetic Device Fabrication

Columnar $TiO_2$ nanostructured film was deposited on an ITO-coated glass using a flame aerosol reactor in a single step process as described in previous publications from our group[2]. The columns were single crystals of approximately 2 μm height. A monolayer of black dye was chemisorbed on the surface of $TiO_2$ columnar films by immersing the films in the 0.33 mM dye solution overnight. After the chemisorption procedure the films were rinsed with anhydrous ethanol several times to remove excess dye. Following the dye chemisorption procedure, an aqueous chlorosome suspension, containing a small amount of ammonium acetate to increase the effective electrical conductivity of the suspension and facilitate the formation of the cone-jet, was electrosprayed in a similar setup as the one used to carry out the size distribution measurements. For these deposition experiments, however, the substrate ($ITO/TiO_2/dye$) was placed perpendicular to the capillary needle a distance of less than 5 mm from the chamber, to form an exit for the $CO_2$ gas. To enhance the hole transport and to prevent electron-hole recombination, hole-carrier P3OT conductive polymer solution was electrospray-deposited on an $ITO/TiO_2/dye/chlorosomes$ substrate. For polymer deposition, no chamber and $CO_2$ gas were required, making the deposition procedure even simpler. A needle with an inner diameter of 1 mm was used instead of the capillary needle to avoid clogging. The substrate was placed perpendicular to the needle at a distance of 1 cm.

### 6.3.4 UV-visible Absorption Measurements

Light absorption measurements of films deposited on ITO-coated glass were carried out with a Varian Cary UV-Visible spectrophotometer (Series II). A certified reflectance standard (Labsphere) provided by the spectrophotometer manufacturer was used during the measurement of the films. These measurements were done under ambient conditions.

### 6.3.5 Fluorescence Measurements

All fluorescence measurements were made on a fluorometer (Photon Technology International, Inc.) equipped with a Xe light source under ambient conditions. For measurements of nano-structured films, a 45° geometry between excitation and detection was used. The fluorescence spectra of chlorosomes shown in Figure 6-3(b) were recorded with 440 nm excitation.

### 6.3.6 Photon-to-Current Quantum Efficiency Measurements

The photocurrent action spectra were acquired using a modified spectrofluorimeter (Spex Tau 2). The active area of the devices was approximately 0.2 cm$^2$. The short-circuit photocurrent was measured as a function of wavelength using an electrometer (Keithley 6514). The raw photocurrent spectrum per active area of device was divided by the relative photon flux spectrum, obtained from the measured lamp profile; and this is the corrected photocurrent action spectrum of each sample reported in

Figure 6-5(b). Note that the reported photocurrent action spectra are not actual incident photon to current conversion efficiency (IPCE) measurements.

## 6.4 Results and Discussion

### 6.4.1 Electrospray-Assisted Online Real Time Characterization of Chlorosomes

Chlorosomes from the green bacterium *C. aurantiacus* suspended in water were electrosprayed to generate single chlorosome particles. As shown in Figure 6-2(a), the size distribution is bimodal with a sharp mode mobility diameter ($D_m$) at 24 nm and a smaller peak at 80 nm. The first peak represents the width of the chlorosomes, which is in good agreement with the reported value of 30 nm from microscopy images for chlorosomes from *C. aurantiacus* [4, 12, 13]. The second peak most probably represents chlorosome agglomerates and impurities of cell fragments left over from the isolation procedure. The chlorosomes are known to have an aspect ratio (β) of approximately 3.0 [4, 12, 14], and thus $D_m$ represents a diameter equivalent to a spherical particle with the same electrical mobility as the chlorosomes. Nevertheless, because the β of the chlorosomes is relatively low and the electric field in the DMA was less than 1000 V cm$^{-1}$ the chlorosomes, which are ellipsoidal particles, were thought to be randomly oriented in the DMA [9]. Therefore the measured $D_m$ most probably corresponds to the width of the chlorosomes. These findings are supported by the results of Allmaier et al. [7] and Kim et al. [9], who using a similar electrospray-assisted mobility-based technique and electron microscopy, demonstrated that the $D_m$ of cylindrical-shaped virus fragments (β= 4.2) corresponded directly to the diameter of the viruses and that of cylindrical nanowires (β <

8.0) corresponded to their projected area diameter, respectively. In an ancillary experiment the same suspension used in the electrospray-assisted size distribution measurement was analyzed with dynamic light scattering (DLS), and the resulting size distribution measurement is shown in Figure 6-2(b). The mode hydrodynamic diameter ($D_h$) was 40 nm. For prolate spheroids, Perrin's formula, which introduces a correction factor for non-spherical particles and end effects, should be used to calculate the size. However, for spheroids with small aspect ratios (< 3) Perrin's formula approaches the Stokes-Einstein expression. Defining an effective spherical diameter as $D_h = (ab^2)^{1/3}$ as done by Wang et al. [15], where $a$ and $b$ are the short and long axes of the spheroid, and taking $b = 24$ nm (from the electrical mobility measurement), gives a chlorosome length of 111 nm. The dimensions of the chlorosomes obtained with the electrospray-assisted and DLS techniques, without the implementation of microscopy images, are in very good agreement with previous literature reports [4, 6, 13, 14, 16].
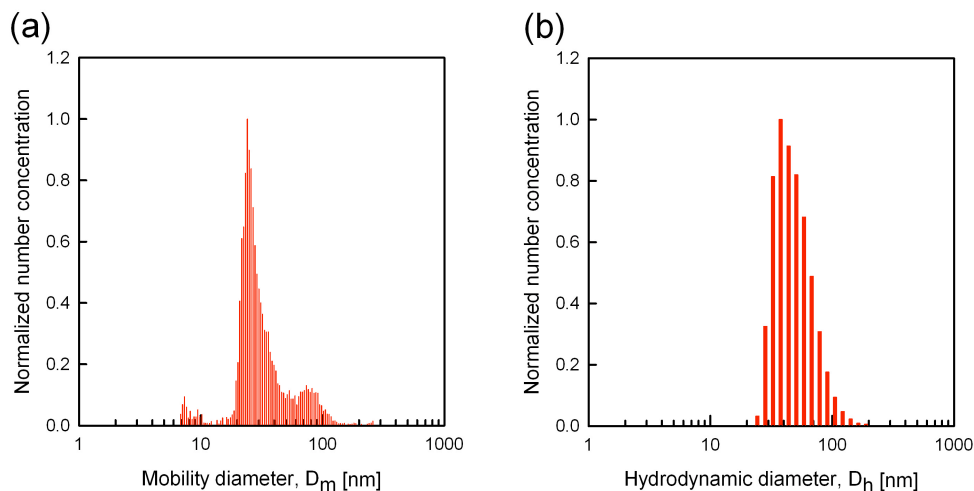


**Figure 6-2:** (a) Normalized particle size distribution of single chlorosomes aerosolized with an electrospray and classified with a DMA. (b) Normalized particle size distribution of chlorosomes suspended in deionized water measured with dynamic light scattering.

Both methods, which complement other techniques, can be coupled in the size characterization of non-spherical biological particles. Furthermore, the average number of elementary charges carried by electrosprayed spherical particles is known to scale with the square of the particle size[17], which is proportional to the particle surface area. The chlorosomes electrosprayed in this study, having a mean surface area of 5725 nm$^2$ were found to carry 334 elementary charges before the charge neutralization and one elementary charge after they were passed through the bipolar neutralizer for the size distribution measurements. This charging of chlorosomes by electrospray enhances their effective deposition onto films with complex morphology as will be discussed later. The implementation of electrospray-deposition facilitates the fabrication of such devices because it simplifies the deposition step as compared to a layer-by-layer deposition technique[14], a multiple step procedure that uses surfactants to generate electrostatic interactions to attach the chlorosomes to the substrate, and which would require further steps to remove undesired surfactant.

To assess any structural damage of chlorosomes during their electrospraying the UV-visible absorption spectra of drop-casted and electrospray-deposited chlorosomes on ITO-coated glasses were measured and plotted in Figure 6-3(a). The inset in Figure (a) shows the UV-visible absorption spectra of chlorosomes dispersed in water; the presence of a small amount of monomeric BChl *c* in the original suspension can be observed at 660 nm. The spectra were normalized at the 740 nm peak to compare the key features of the absorption spectra of chlorosomes. The inset depicts the UV-visible absorption spectra of the chlorosome suspension used for the film fabrication. The characteristic peak at 740 nm in the spectra of both films indicates the presence of oligomers of BChl *c*,

suggesting that the electrospray-deposited chlorosomes maintained their integrity and that no significant physical transformation nor degradation occurred during the electrospray-deposition.

**(a)**                                                    **(b)**
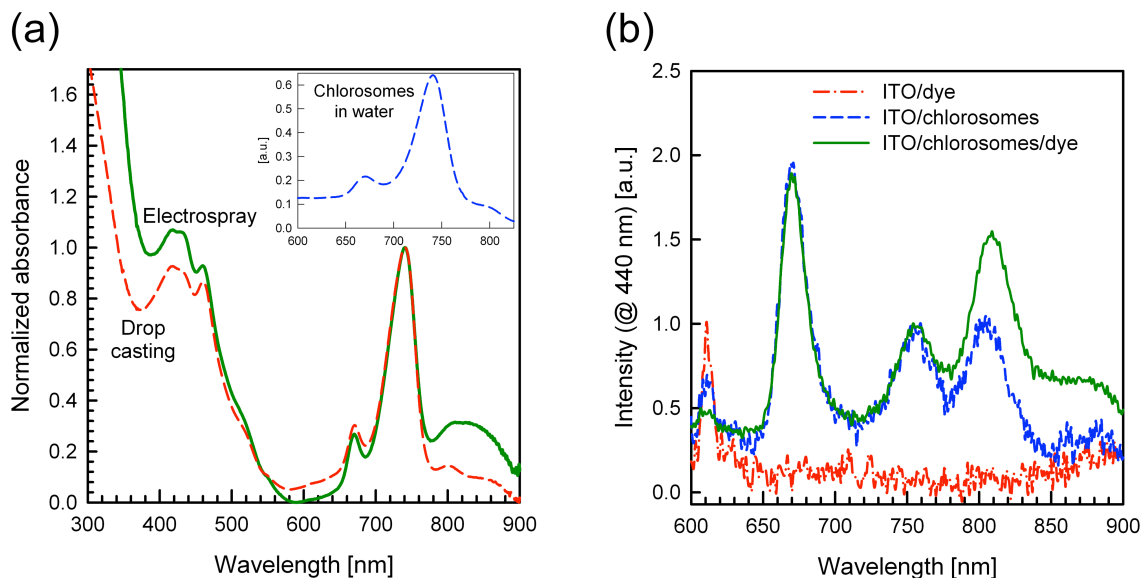


**Figure 6-3: (a)** UV-visible absorption spectra of chlorosomes deposited on ITO-coated glass by drop-casting and by electrospray. (b) Fluorescence spectra of chlorosomes, dye, and dye/chlorosomes deposited onto an ITO-coated glass.

Figure 6-3(a) also indicates that the observed monomeric BChl *c* peak at about 666 nm is not due to the electrospray-deposition, since it appears in the spectra of both films and in the spectrum of chlorosomes in water, but it may arise from partially damaged chlorosomes during the isolation from the bacterium, as shown in the inset where a small amount of monomeric BChl *c* can be observed in the absorption spectra of chlorosomes in water. Other authors [18] artificially assembled porphyrin films, to mimic the naturally self-assembled BChl *c* rods of chlorosomes, onto $TiO_2$ electrodes. The films were fabricated by spin-coating from a porphyrin solution onto the $TiO_2$ electrode, followed by

heat treatment [18]. However, the authors reported that monomers of BChl were formed on the surface of the porphyrin stacks upon annealing. Furthermore, they concluded that although a more efficient charge separation occurs in the monomeric BChl, the exciton transfer from an oligomer to a monomer is energetically unfavorable thus decreasing the electron injection rate into the $TiO_2$ [18]. The difficulty in linking the BChl *c* oligomers to the surface of the semiconductor material makes the electrospraying of whole chlorosomes a potentially useful approach to avoid both the formation of a large amount of monomeric BChl *c* during deposition and the need for surfactant removal [14, 19].

6.4.2 Characteristics of Chlorosome-Dye Interactions

The first step for the fabrication of a biomimetic light-harvesting device is to study the chlorosomes-dye energy transfer, because ultimately an interaction between those two components is critical for the functioning of the device. To study the chlorosome-dye interaction, an anhydrous ethanol solution of black dye was electrospray-deposited onto chlorosomes that were drop-casted onto an ITO-coated glass. The dye was electrosprayed to avoid contact of ethanol with the chlorosomes and thus prevent formation of BChl *c* monomers in the chlorosome envelop. Figure 6-3(b) shows the fluorescence spectra, with 440 nm excitation, of chlorosomes, of black dye, and of black dye/chlorosomes deposited onto ITO-coated glasses. The characteristic peaks of monomeric and polymeric BChl *c*, and the BChl *a* (baseplate) in the ITO/chlorosomes film appeared at 660 nm, 760 nm, and 805 nm, respectively as observed earlier by us and other authors [4, 20]. Note that the film with black dye/chlorosomes showed higher

fluorescence intensity (805 nm) than the films with only chlorosomes at the baseplate peak, while the intensities of the 660 nm and the 760 nm peaks remained unchanged. Furthermore, a slight shift was observed in the baseplate peak from 805 nm in the ITO/chlorosomes film to 809 nm in the ITO/chlorosomes/dye film. It is important to highlight that similar results were obtained from fluorescence measurements of black dye/chlorosomes in water (data not shown), implying that the increase in the fluorescence of the baseplate peak was neither a product of the electrospray deposition nor an artifact of the measurements. However, a precise reason could not be elucidated and further studies are needed to understand an excitation energy transfer mechanism from the chlorosome to the dye.

### 6.4.3 Fabrication and Performance of a Biomimetic Light-Harvesting Device

As the second step in the device fabrication, chlorosomes were electrosprayed onto columnar $TiO_2$ nanostructures, which had chemisorbed dye on the surface. The $TiO_2$ nanostructured columns synthesized by a flame aerosol reactor are shown in the image in Figure 6-4(a), and the chlorosomes electrospray-deposited onto the $TiO_2$ film are shown in Figure 6-4(b). The image in Figure 6-4(b) corresponds to the lower part of a column, confirming the effective deposition of chlorosomes over the entire film, even in parts difficult to reach by other aerosol techniques such as atomization or nebulization. The deposition at the bottom of the columns along their long axis is a result of the multiple charging of chlorosomes during electrospray. The established electric field between the capillary needle and the grounded substrate forced the highly charged

chlorosomes (having about 330 elementary charges) to penetrate deeper into the columns, by ballistic deposition, overcoming the effect of Brownian motion. Note that the values of 24 nm and 111 nm for the width and length of the chlorosomes, respectively, obtained with the electrospray-assisted mobility-based technique agree well with the dimensions of the chlorosomes observed in Figure 6-4(b).
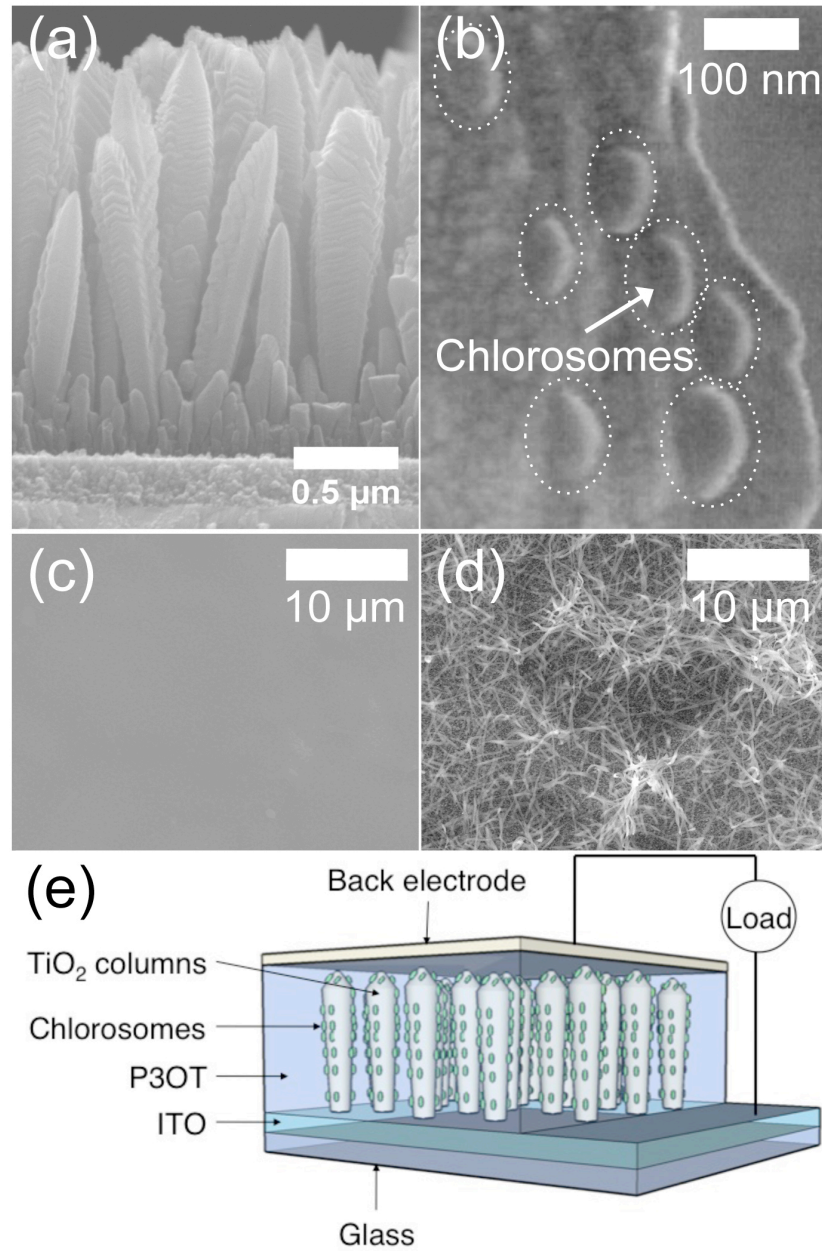
**Figure 6-4:** (a) A TiO$_2$ nanostructured film with columnar morphology deposited onto an ITO-coated glass by a flame aerosol reactor. (b) Microscopy image of chlorosomes electrospray-deposited onto a columnar TiO$_2$ nanostructured film. Images of P3OT polymer film at spray distances of (c) 1.0 cm and (d) 1.7 cm. (e) Schematic cartoon of a novel biomimetic light-harvesting hybrid device that incorporates whole chlorosomes (without a natural RC) and nanostructured TiO$_2$ columns.

For the third step of device fabrication, P3OT polymer was electrosprayed onto an ITO-coated glass and the film morphology was analyzed with electron microscopy. The polymer film morphology, which plays a role in the hole transport and in preventing charge recombination, can be controlled by simply adjusting the spray distance[21] (the distance between the tip of the capillary needle and the substrate). A smooth film (Figure 6-4(c)) was obtained at a spray distance of 1.0 cm while a ribbon-like morphology was obtained at 1.7 cm (Figure 6-4(d)). At a longer spray distance, the toluene evaporated completely, leaving small particles of P3OT that grew on the substrate in a ribbon-like morphology. Conversely, at a shorter spray distance toluene evaporated only partially, but presumably its volume was small enough not to damage the integrity of the BChl *c* aggregates in the chlorosomes, as indicated by the spectra in Figure 6-5(a), and upon collision of the toluene-P3OT droplet with the substrate, the polymer extended and reorganized on the substrate into a smooth layer[21]. In the following deposition experiments, the smooth morphology was preferred because it allowed a unidirectional hole transport and suppressed short circuiting during back contact formation.

(a)

(b)
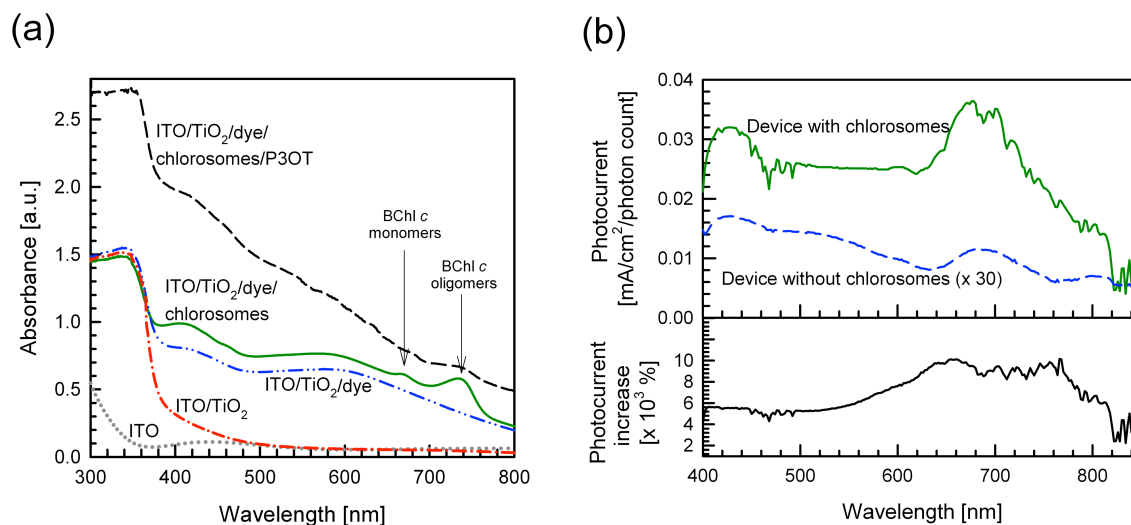


**Figure 6-5:** (a) UV-visible absorption spectra of the biomimetic device at different steps of the fabrication; ITO-coated glass; ITO/TiO$_2$ nanocolumns, ITO/TiO$_2$ nanocolumns/dye, and ITO/TiO$_2$ nanocolumns/dye/chlorosomes/P3OT. (b) Measured photocurrent in biomimetic devices with and without chlorosomes. The photocurrent of the device without chlorosomes was increased 30 times for plotting purposes. The bottom figure shows the percentage increase in photocurrent.

Finally, a complete biomimetic light-harvesting hybrid device was constructed as shown in the cartoon in Figure 6-4(e). The device consisted of the following layers of materials from the bottom to the top, glass/ ITO /nano-columnar TiO$_2$/ black dye monolayer/ chlorosomes/ P3OT polymer/ Pt back electrode. The UV-visible absorption spectra of the device at each fabrication step are shown in Figure 6-5(a) where the contribution of the individual components to the spectra can be appreciated. The characteristic peaks of monomers and oligomers of BChl *c* in the ITO/TiO$_2$/dye/chlorosomes film were in good agreement with the spectra in Figure 6-3(a), implying again that the chlorosome deposition process did not damage the structure

of the BChl *c* oligomers to any significant extent. Furthermore, a small peak of the BChl *c* oligomers can be observed in the spectra after the P3OT deposition that implies the presence of the efficient light-harvesting structures in the complete device. The photocurrent action spectra of devices with and without chlorosomes, and the photocurrent increase in a device with chlorosomes are shown in Figure 6-5(b) top and bottom, respectively. The photocurrent increase was calculated from %P increase = 100 x $(P_{chlorosomes} - P_{dye\ only})/P_{dye\ only}$, where P denotes photocurrent. Clearly, an interaction between the dye and chlorosomes enhanced the current generation in the nanostructured solar cell by several times over the entire range of wavelengths measured. In the device containing chlorosomes there is a remarkable photocurrent increase, particularly at longer wavelengths, from 640 nm to the near-infrared regime where BChl *c* oligomers and BChl *a* in the baseplate have their absorption maxima (Figure 6-5(b) bottom). Indeed, it appears as though the ratio of the peak at 680 nm to the peak at 430 nm increases from 0.67 in the dye-only case, to 1.13 in the dye-chlorosome case, a 168% increase. Chlorosome-containing bacteria are able to survive under extreme low light conditions. Success of these organisms is due, in part, to the large cross-sectional area of the chlorosome as well as its high energy transfer efficiency, and to its ability of harvesting near-infrared radiation that does not originate from the sun, even at more than 2300 m oceanic depth near a volcanic vent [22].


## 6.5 Conclusions

This study represents the first attempt to build a complete biomimetic light-harvesting device that incorporates intact whole chlorosomes from green bacteria, based

on the concept of biomimetics. The electrospray technique was successfully applied to aerosolized intact chlorosomes to measure their particle size distribution online in real-time and to deposit them onto a $TiO_2$ nanostructured film. The use of chlorosomes with naturally self-assembled pigments rather than artificially self-assembled bacteriochlorophyll pigments[18] takes advantage of the efficient organization of the pigments in the antenna and prevents the formation of large amounts of undesired monomeric BChl *c* on the surface of the oligomers that hinder the electron transport to the $TiO_2$ film as occurred in artificially assembled rods of BChl *c*[18]. Note, that some BChl *c* monomers may form during the chlorosomes isolation procedure. However, the electrospray-deposition seemed not to affect the structure of the rods. The presence of the chlorosomes in the device increased the photocurrent as a function of wavelength over thirty times. The results presented here are encouraging. Nevertheless, additional studies must be carried out to elucidate the interactions of chlorosomes with the black dye, and perhaps with other dyes, and to assess the stability of the components in the long term with the aim of improving the efficiency of such devices.

**6.6 References**

1 . S. Ito, S. Zakeeruddin, R. Humphry-Baker, P. Liska, R. Charvet, P. Comte, M. Nazeeruddin, P. Péchy, M. Takata, H. Miura, S. Uchida, and M. Grätzel, *Adv. Mater.*, 2006, **18**(9), 1202-1205.

2 . E. Lancelle-Beltran, P. Prené, C. Boscher, P. Belleville, P. Buvat, and C. Sanchez, *Adv. Mater.*, 2006, **18**(19), 2579-2582.

3 . U. Bach, D. Lupo, P. Comte, J. E. Moser, F. Weissortel, J. Salbeck, H. Spreitzer, and M. Gratzel, *Nature*, 1998, **395**(6702), 583-585.

4 . Y. Bai, Y. Cao, J. Zhang, M. Wang, R. Li, P. Wang, S. Zakeeruddin, and M. Grätzel, *Nat. Mater.*, 2008, **7**(8), 626-630.

5 . P. Wang, S. M. Zakeeruddin, J. E. Moser, M. K. Nazeeruddin, T. Sekiguchi, and M. Gratzel, *Nat. Mater.*, 2003, **2**(6), 402-407.

6 . I. Gonzalez-Valls and M. Lira-Cantu, *Energy Environ. Sci.*, 2009, **2**, 19-24.

7 . M. Pagliaro, G. Palmisano, R. Ciriminna, and V. Loddo, *Energy Environ. Sci.*, 2009, **2**(8), 805 - 896.

8 . E. Thimsen and P. Biswas, *AIChE Journal*, 2007, **53**(7), 1727-1735.

9 . E. Thimsen, N. Rastgar, and P. Biswas, *J. Phys. Chem. C*, 2008, **112**(11), 4134-4140.

10 . J. Barber and B. Andersson, *Nature*, 1994, **370**(6484), 31-34.

11 . R. E. Blankenship, J. M. Olson, and M. Miller, in *Anoxygenic Photosynthetic Bacteria*, eds. R.E. Blankenship, M.T. Madigan, and C.E. Bauer, Kluwer Academic, Dordrecht, 1995, pp. 399-435.

12 . T. P. Causgrove, D. C. Brune, and R. E. Blankenship, *J. Photochem. Photobiol. B*, 1992, **15**(1-2), 171-179.

13 . T. P. Causgrove, D. C. Brune, J. Wang, B. P. Wittmershaus, and R. E. Blankenship, *Photosyn. Res.*, 1990, **26**(1), 39-48.

14 . G. Scholes and G. Rumbles, *Nat. Mater.*, 2006, **5**(9), 683-696.

15 . R. G. Feick, M. Fitzpatrick, and R. C. Fuller, *J. Bacteriol.*, 1982, **150**(2), 905-915.

16 . Z. Fetisova, A. Freiberg, V. Novoderezhkin, A. Taisova, and K. Timpmann, *FEBS Lett.*, 1996, **383**(3), 233-236.

17 . G. Allmaier, C. Laschober, and W. Szymanski, _Journal of the American Society for Mass Spectrometry_, 2008, **19**(8), 1062-1068.

18 . C. J. Hogan, E. M. Kettleson, B. Ramaswami, D. R. Chen, and P. Biswas, _Anal. Chem._, 2006, **78**(3), 844-852.

19 . S. L. Kaufman, _J. Aerosol Sci._, 1998, **29**(5/6), 537-552.

20 . S. H. Kim, G. W. Mulholland, and M. R. Zachariah, _J. Aerosol Sci._, 2007, **38**(8), 823-842.

21 . E. O. Knutson and K. T. Whitby, _J. Aerosol Sci._, 1975, **6**, 443-451.

22 . C. J. Hogan and P. Biswas, _Aerosol Sci. Technol._, 2008, **42**(1), 75-85.

23 . L. B. Modesto-Lopez, J. D. Pasteris, and P. Biswas, _Appl. Spectr._, 2009, **63**(6), 627-635.

24 . S. G. Sprague, L. A. Staehelin, M. J. Dibartolomeis, and R. C. Fuller, _J. Bacteriol._, 1981, **147**(3), 1021-1031.

25 . Y. W. Zhu, B. L. Ramakrishna, P. I. vanNoort, and R. E. Blankenship, _Bba-Bioenergetics_, 1995, **1232**(3), 197-207.

26 . A. Sridharan, J. Muthuswatriy, J. T. LaBelle, and V. B. Pizziconi, _Langmuir_, 2008, **24**(15), 8078-8089.

27 . Z. Y. Wang, G. Marx, M. Umetsu, M. Kobayashi, M. Mimuro, and T. Nozawa, _Bba-Bioenergetics_, 1995, **1232**(3), 187-196.

28 . M. Mimuro, T. Nozawa, N. Tamai, K. Shimada, I. Yamazaki, S. Lin, R. S. Knox, B. P. Wittmershaus, D. C. Brune, and R. E. Blankenship, _J. Phys. Chem._, 1989, **93**(21), 7503-7509.

29 . J. Suh, B. Han, K. Okuyama, and M. Choi, *J. Colloid Interf. Sci.*, 2005, **287**(1), 135-140.

30 . A. Huijser, P. Marek, T. Savenije, L. Siebbeles, T. Scherer, R. Hauschild, J. Szmytkowski, H. Kalt, H. Hahn, and T. S. Balaban, *J. Phys. Chem. C*, 2007, **130**(8), 2485-2492.

31 . Y. Saga, T. Y. Kim, T. Hisai, and H. Tamiaki, *Thin Solid Films*, 2006, **500**(1-2), 278-282.

32 . Z. G. Fetisova, A. M. Freiberg, and K. E. Timpmann, *Nature*, 1988, **334**(6183), 633-634.

33 . M. Mimuro, Y. Nishimura, I. Yamazaki, M. Kobayashi, Z. Y. Wang, T. Nozawa, K. Shimada, and K. Matsuura, *Photosyn. Res.*, 1996, **48**(1-2), 263-270.

34 . I. B. Rietveld, K. Kobayashi, H. Yamada, and K. Matsushige, *J. Phys. Chem. B*, 2006, **110**(46), 23351-23364.

35 . J. T. Beatty, J. Overmann, M. T. Lince, A. K. Manske, A. S. Lang, R. E. Blankenship, C. L. Van Dover, T. A. Martinson, and F. G. Plumley, *P. Natl. Acad. Sci. USA*, 2005, **102**(26), 9306-9310.

# Chapter 7: Summary and Future Directions

**7.1 Summary**

The studies conducted as part of this dissertation addressed fundamental aspects of the electrospray of suspensions for applications in nanoparticle characterization and deposition, including the use of a soft X-ray photoionizer to create a bipolar ion environment and reduce the charge-state of electrosprayed bioparticles, the generation of monodisperse agglomerates electrosprayed from $TiO_2$ nanoparticle suspensions, the production of uniform nanostructured iron oxide films followed by micro-Raman spectroscopic analyses, the characterization and deposition of natural light-harvesting complexes, and the charge distribution of a variety of light-harvesting complexes nebulized from aqueous suspensions. Here, the major outcomes of this work are summarized:

i.  Demonstrated the efficacy of photoionization with soft X-rays to create a bipolar ion environment, with high ion number density, and to reduce the charge-state of electrosprayed bioparticles. The soft X-ray charger could be incorporated into an electrospray and the combined system may be employed for size characterization of a variety of nanoparticles on the basis of their electrical mobility.

ii. Proposed a modified equation to calculate the effective electrical conductivity of $TiO_2$ nanoparticle suspensions accounting for both particle surface charge and particle agglomeration effects. These nanoparticle effects were more remarkable in liquids with low ionic strength, where a dependency on nanoparticle volume

fraction in the suspension was also found. At an intermediate liquid ionic strength, the contribution from the particle electrical double layer to the electrical conductivity was minimized by a high ion number density in the liquid. This was the first study that reports on the influence of the effective electrical conductivity of nanosuspensions on the electrospray process. The outcome of this study has broad applicability in the generation of agglomerates to form thin films of photocatalytic materials and to conduct inhalation and airborne-drug delivery studies.

iii. Proposed a parameter to estimate the crystallite size of electrospray-deposited iron oxide films based on the spectral separation of transverse and longitudinal optical modes present in the micro-Raman spectra of the films. The appearance of the two modes in the Raman spectra is dependent on the wavelength of the laser used for the analyses. The methodology may be applicable to films of other materials, so long as Raman modes sensitive to crystallite size are discernible and the appropriate laser wavelength is used.

iv. Demonstrated the applicability of the electrospray to fabricate films of natural photosynthetic complexes by simultaneous drying and charging in flight followed by deposition. More specifically, the electrospray was used to proof the concept of a novel nanobio hybrid photovoltaic device, which incorporated highly efficient light-harvesting chlorosomes. The chlorosomes maintained their light-

harvesting properties even after being exposed to a strong electric field during electrospray-deposition.

v.  Measured the size of single units of light-harvesting complexes from photosynthetic bacteria, by isolating the complexes in highly charged, submicrometer-sized droplets. The size of single chlorosomes, FMO complexes, LH2 complexes, and dimers of the FMO complexes were precisely identified with electrical mobility analysis. This was the first study reported in the literature on characterization of light-harvesting complexes using the electrospray.

vi. Identified the charge-state of airborne light-harvesting complexes generated with a collision nebulizer. Although the nebulization method does not involve electrical process, the aerosolized light-harvesting complexes carried as many as +4 elementary charges. Aerosolization, drying and charging in flight with a collision nebulizer has the advantages of high throughput and relatively facile scale up. The methodology focused on the generation of charged light-harvesting complexes to form functional films using electrophoresis.

**7.2 Future directions**

This work demonstrated the wide range of applications of the electrospray technique. Fundamental studies were conducted to explore the use of electrospray to form thin films and coatings of several functional materials.

Chapter 3 addressed the significance of both nanoparticle surface charge and nanoparticle agglomeration in the precursor suspension to generate agglomerates with electrospray. However, there are experimental indications that the particle size and particle crystal phase may play a role in the conductivity of nanosuspensions, particularly in materials such as $TiO_2$, which show polymorphism. Hence more detailed studies are needed to elucidate such effects on the dynamics of the electrospray and on the characteristics of the final agglomerates. The studies conducted in this dissertation certainly may serve as a model for future research on the electrospray of nanosuspensions.

A novel area to explore is the processing of natural light-harvesting complexes from photosynthetic bacteria. Chapters 5 and 6 addressed some fundamental questions in the aerosolization of such complexes and Chapter 6 proved the concept of a nanobio hybrid photovoltaic device fabricated using electrospray. However, the resulting charging characteristics of such light-harvesting complexes with electrospray still remain unclear. In addition, although electrospray is a useful tool to fabricate nanostructured devices, it is not the most suitable method when it comes to industrial scale. Hence, alternative approaches such as charging with conventional nebulization, with more industrial flexibility, need to be further investigated.

Hollow spherical vesicles made of lipid bilayers, as in the walls of cell membranes of various organisms, are of great interest for drug encapsulation and delivery. Currently such vesicles, or liposomes, are prepared by mixing a series of lipids followed by extruding the suspension to reduce the polydispersity of the liposomes, which is a multistep process. Electrospray could be used to aerosolize a lipid suspension (containing a desired drug) and form monodisperse, nanometer-sized liposomes in-flight, which would allow controlling their transport characteristics and assessing their deposition location in the human respiratory tract. Another approach is the use of dual capillary electrospray, in which the inner capillary feeds a drug solution and the outer capillary feeds the lipid suspensions. In this manner effective encapsulation of the drug may be achieved at the capillary outlet. However, fundamental studies of size, surface charge, and charge-state of the liposomes as a result of the electrospray and neutralization processes would be required to investigate the aerosol characteristics of the vesicles.

**Appendix I: Experimental Schematics and Supporting Data**

## A.1 Estimation of the Activation Energy (E$_{ac}$) for Sintering of Iron-oxide Films using Images of Electrospray-deposited Films

The following procedure is explained as an alternative to calculate a film's surface area reduction and thus the energy of activation for sintering. The surface area of powders annealed a various temperatures may be estimated using the Brunauer-Emmett-Teller (BET) technique. However, when I comes to nanostructured films not all BET instruments have such capability. Electrospray of nanostructured films allows for deposition onto a targeted area on the substrate and of a small amount of material. Ideally we would like to measure the decrease of film total surface area at different stages in the annealing procedure. Alternatively, we could record several scanning electron microscopy (SEM) images of the films and then adjust the contrast between the film and the substrate and have the software to calculate the coated area. A procedure to estimate the activation for sintering is described below:

The transient variation of surface area may be defined as [1,2]:

$$\frac{da}{dt} = \frac{1}{\tau_s}\left(a - a_s\right) \tag{1}$$

where $a$ is the initial surface area of the agglomerate, $\tau_s$ is the characteristic sintering time, $a_s$ is the surface area of an sphere with the same volume as the agglomerates, and $t$ is the time at which the surface area measurement was recorded (or the annealing time).

Kobata et al [3] proposed an equation for the sintering time of TiO$_2$ particles in high temperature reactors:

$$\tau_s = A d_p^4 T \exp\left(E_{ac}/RT\right) \tag{2}$$

where $A$ is the pre-exponential factor (s K$^{-1}$ m$^{-4}$), $E_{ac}$ is the activation anergy of the diffusion process (kJ mol$^{-1}$), R is the ideal gas constant (kJ K$^{-1}$ mol$^{-1}$), $T$ is the temperature (K), and $d_p$ is the initial particle diameter (m).

To estimate $E_{ac}$ of the films:

1.  Electrospray-deposit a film and anneal it at a given temperature $T$.

2. Use BET to measure the film surface area at different annealing time $t$. Or, take SEM images of the cross section area of the films annealed at temperature $T$ at different annealing times $t$.

3. Use an imaging software to calculate the cross section area of the film at each annealing time $t$.

4. From the BET measurements or the cross section area reduction in step 3 obtain $\Delta a/\Delta t$ (i.e., $da/dt$) and $\tau_s$ (i.e., the time $t$ at which the films sintered completely, this is an experimental $\tau_s$).

5. Combine expressions (1) and (2) to obtain:

$$\ln(\tau_s) - \ln(Ad_p^4 T) = \frac{E_{ac}}{RT} \tag{3}$$

6. Make a plot of $\ln(\tau_s)$ against $(1/T)$; from the slope of the line find $E_{ac}$ and from the intersection with the y-axis find the exponential factor $A$.
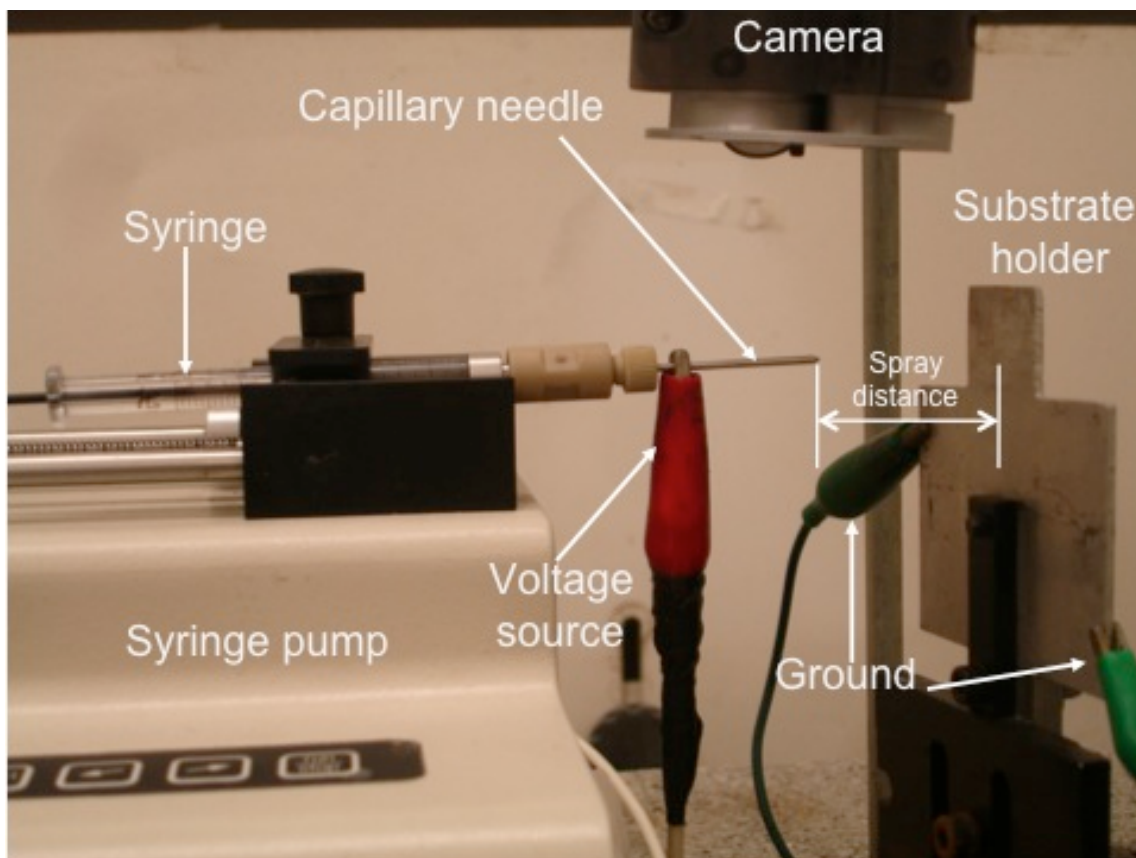
References:

(1)    Cho, K.; Biswas, P. *Aerosol Sci. Tech.* **2006**, *40*, 309.

(2)    Friedlander, S. K. *Smoke, dust, and haze : fundamentals of aerosol dynamics*; 2nd ed.; Oxford University Press: New York, 2000.

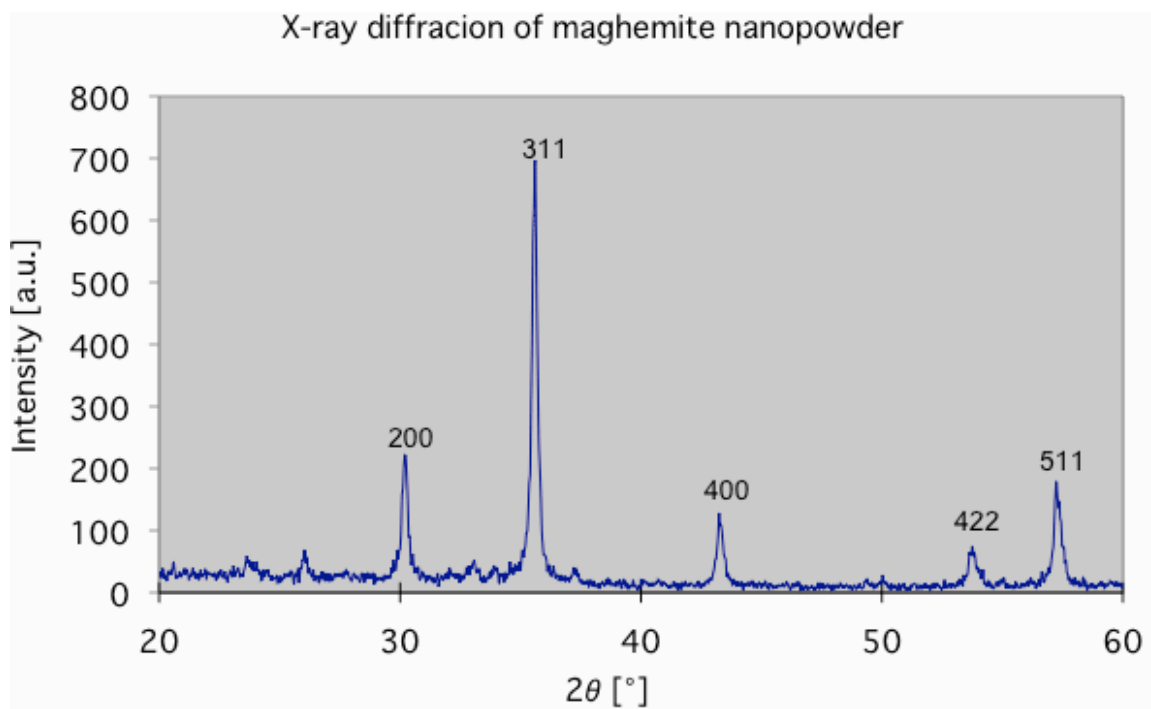(3)    Kobata, A.; Kusakabe, K.; Morooka, S. *AIChE J.* **1991**, *37*, 347.
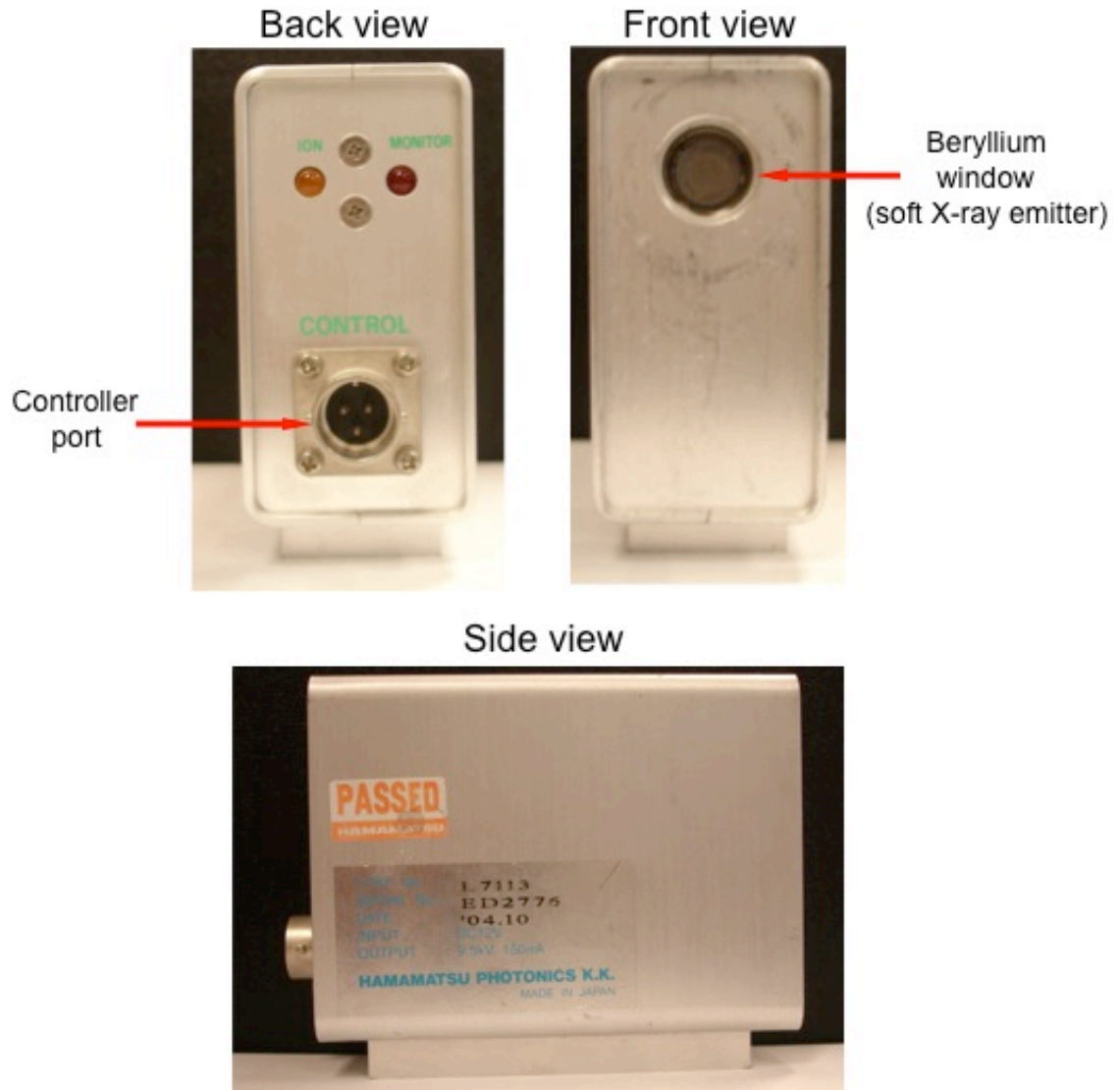
**Figure I-1:** Schematic of the soft X-ray charger used for the study in Chapter 1.

**Figure I-2:** Electrospray deposition setup used in the studies of Chapters 3 and 4.

**Figure I-3:** X-ray diffraction pattern of the maghemite nanopowder used in the Raman study of Chapter 4.

The data was recorded with a Rigaku D-MAX/A9 diffractometer with CuKα radiation (λ = 1.5418 Å).

**Table I-1:** pH of ethanol/water $TiO_2$ nanosuspensions at particle volume fractions and varying nitric acid concentrations (for the study in Chapter 3).

| Volume fraction of particles, $\phi_p$ [%] | 0 mM $HNO_3$ (curve (a) in Fig. 2) | | 0.32 mM $HNO_3$ (curve (f) in Fig. 2) | |
|---|---|---|---|---|
| | pH | Zeta potential [mV] | pH | Zeta potential [mV] |
| 0.004 | 7.5 | - 5.2 | 3.71 | + 8.59 |
| 0.02 | 6.0 | - 2.2 | 3.72 | + 9.30 |
| 0.04 | 5.02 | + 4.1 | 3.69 | + 10.1 |
| 0.1 | 4.62 | - | 3.76 | - |
| 0.2 | 4.40 | - | 3.65 | - |
| 0.4 | 4.37 | - | 3.68 | - |

The pH measurements were recorded with a Cole Parmer pH meter (Accumet AB15) and the zeta potential measurements were carried out with a Malvern Zetasizer Nanoseries.
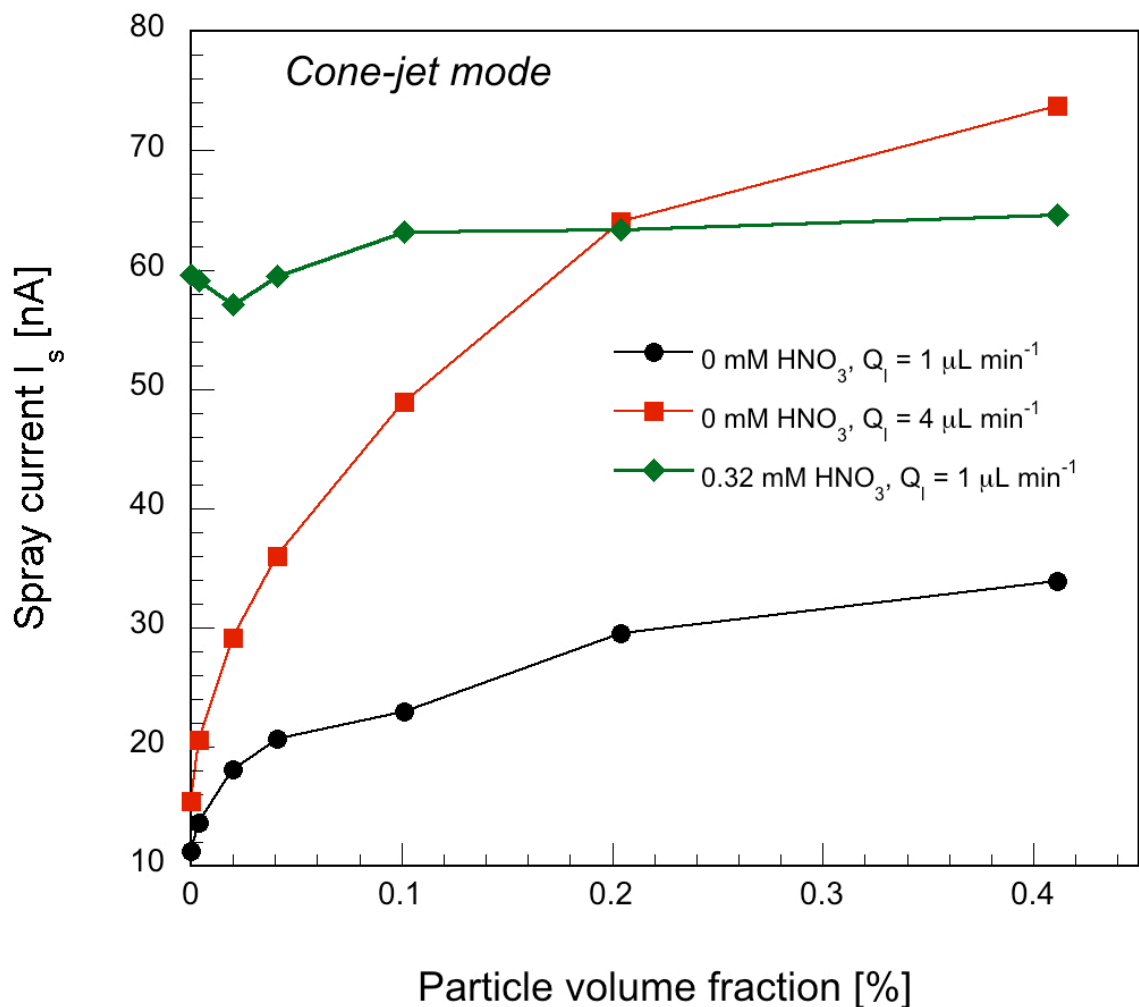
**Figure I-4:** Current emitted by the electrospray plume of the $TiO_2$ nanosuspensions studied in Chapter 3 as a function of particle volume fraction (for liquids with low and high conductivity). Note that the data were recorded in the cone-jet mode at two different liquid flow rates ($Q_l$), 1 and 4 μL min$^{-1}$.

The spray current was measured in an electrospray-deposition setup as described in Figure I-2. The spray current was measured using a picoammeter (Keithley, model 6485).
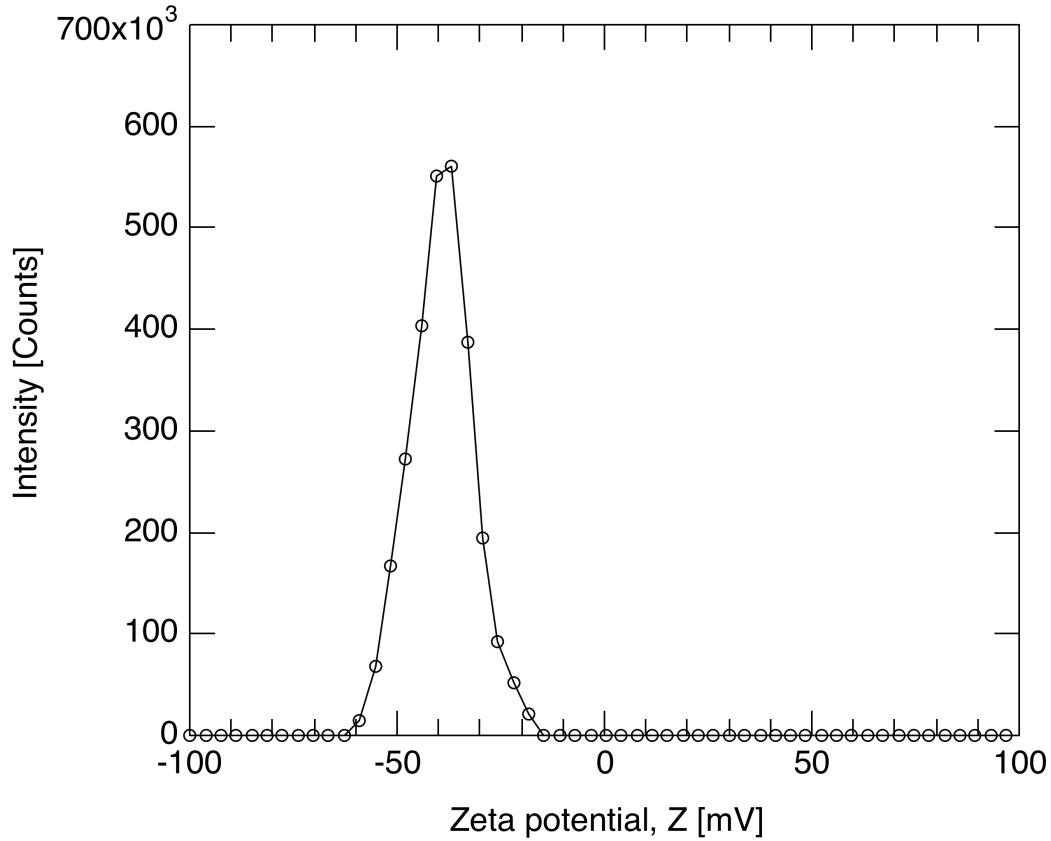
**Figure I-5**: Zeta potential measurement of chlorosomes suspended in pure water.

The measurement corresponds to the chlorosome suspension used in the nanobio hybrid light-harvesting device fabrication with electrospray in Chapter 5. The highly negative zeta potential indicates that the suspension was stable and chlorosomes did not agglomerate and sediment.
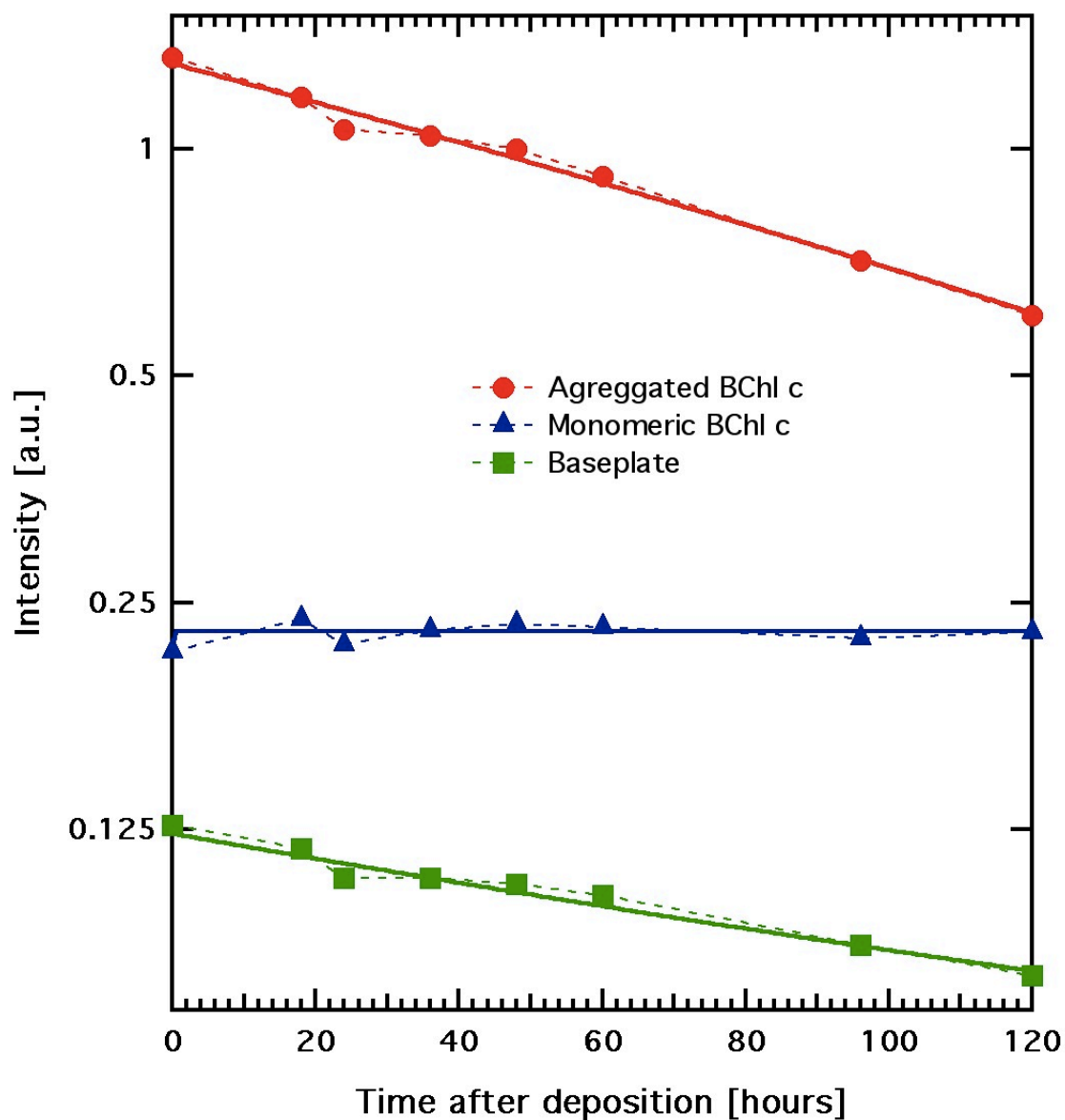
**Figure I-6:** Stability of chlorosomes electrospray-deposited onto an ITO-coated glass over time. The figure shows absorption maxima of the three characteristic peaks of the chlorosomes at 670 nm (monomeric BChl *c*), 740 nm (aggregated BChl *c*), and 805 nm (baseplate) as a function of time. The intensity of the aggregated BChl *c* and the baseplate decreases with increasing the time after deposition.
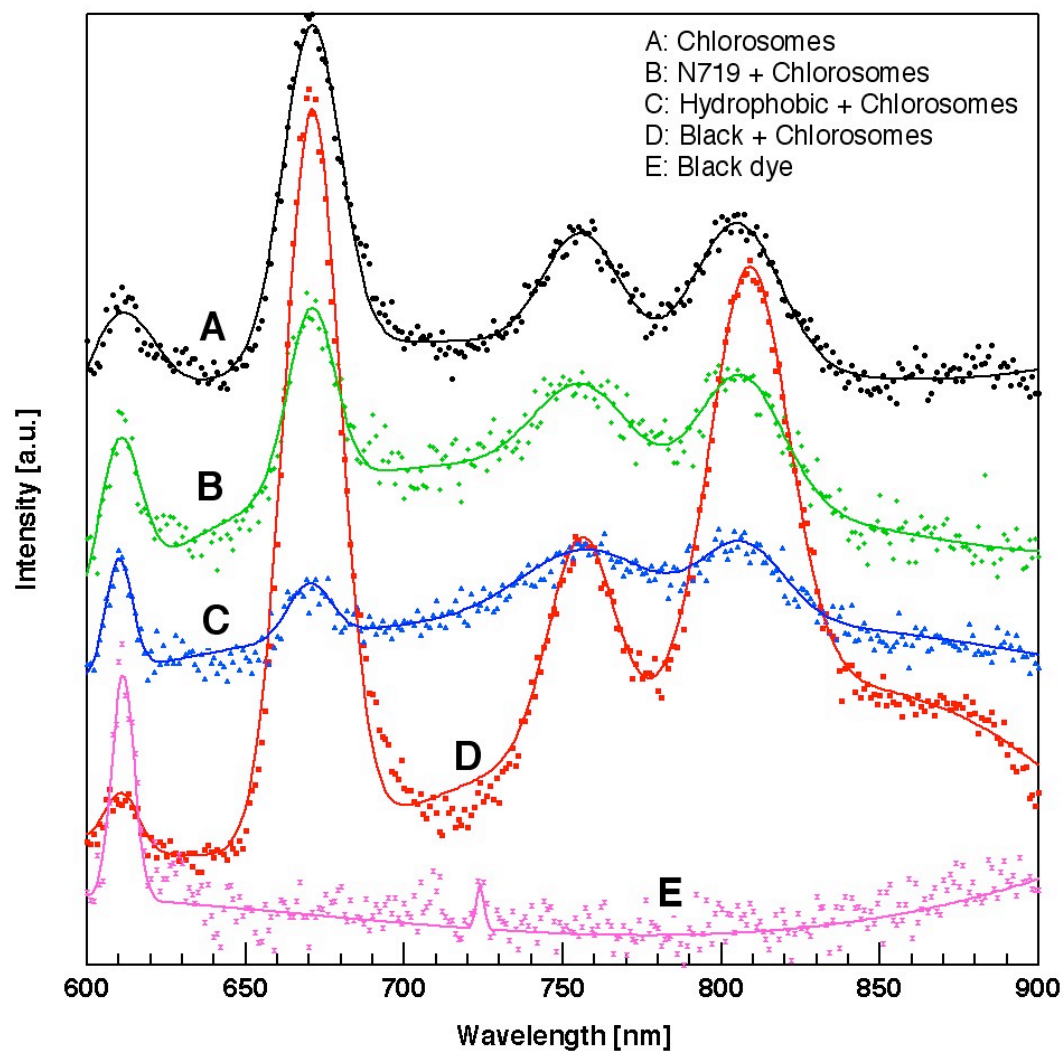
**Figure I-7:** Fluorescence spectra of aqueous suspensions of chlorosomes with various dyes. There seems to be an interaction of chlorosomes with the black dye that increases the fluorescence of the baseplate (at the bottom of the chlorosome envelope) at ~ 810 nm.
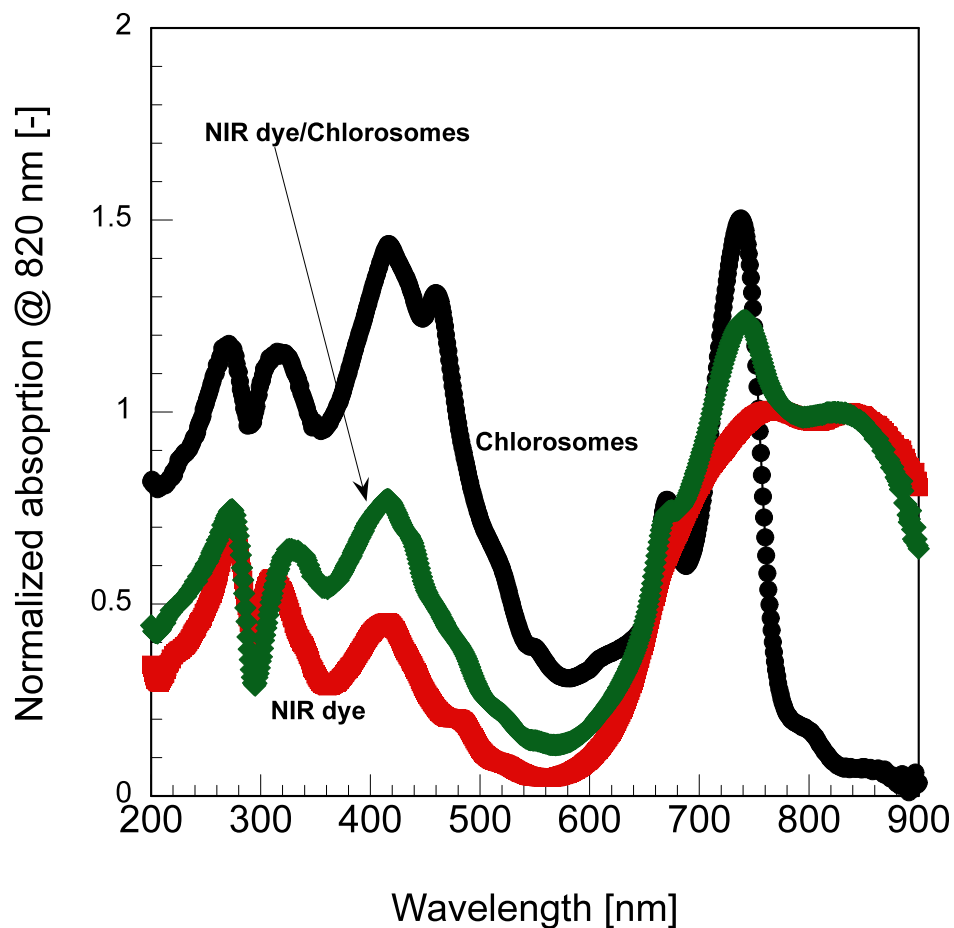
**Figure I-8**: UV-visible absorption spectra of films of chlorosomes, NIR dye (abs. max. @ 820 nm), and chlorosomes/NIR dye deposited onto an ITO-coated glass. The absorption of the chlorosome baseplate is close to the absorption maxima of the NIR dye, hence there is a possibility of energy transfer and funneling from the chlorosome envelope to the dye molecules.
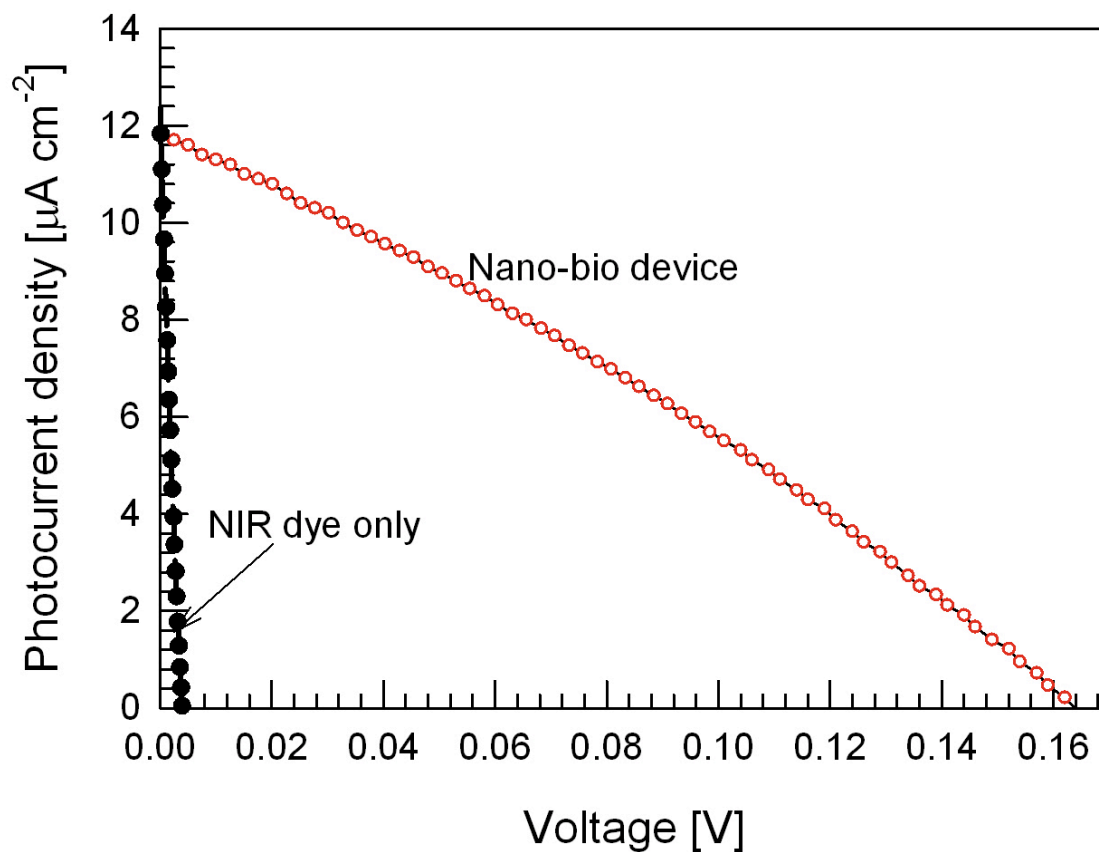
**Figure I-9:** I-V curve of a nanobio hybrid photovoltaic device, with chlorosomes, such as the one designed in the study of Chapter 5. However, in this case a near-infrared (NIR) dye was used instead of a black dye. The NIR dye has strong absorption maxima at 820 nm, hence it was expected to serve as an effective artificial reaction center for solar energy transfer from the chlorosomes to a $TiO_2$ film.

Further study of the NIR dye-chlorosome system is needed to elucidate the mechanism of energy transfer.
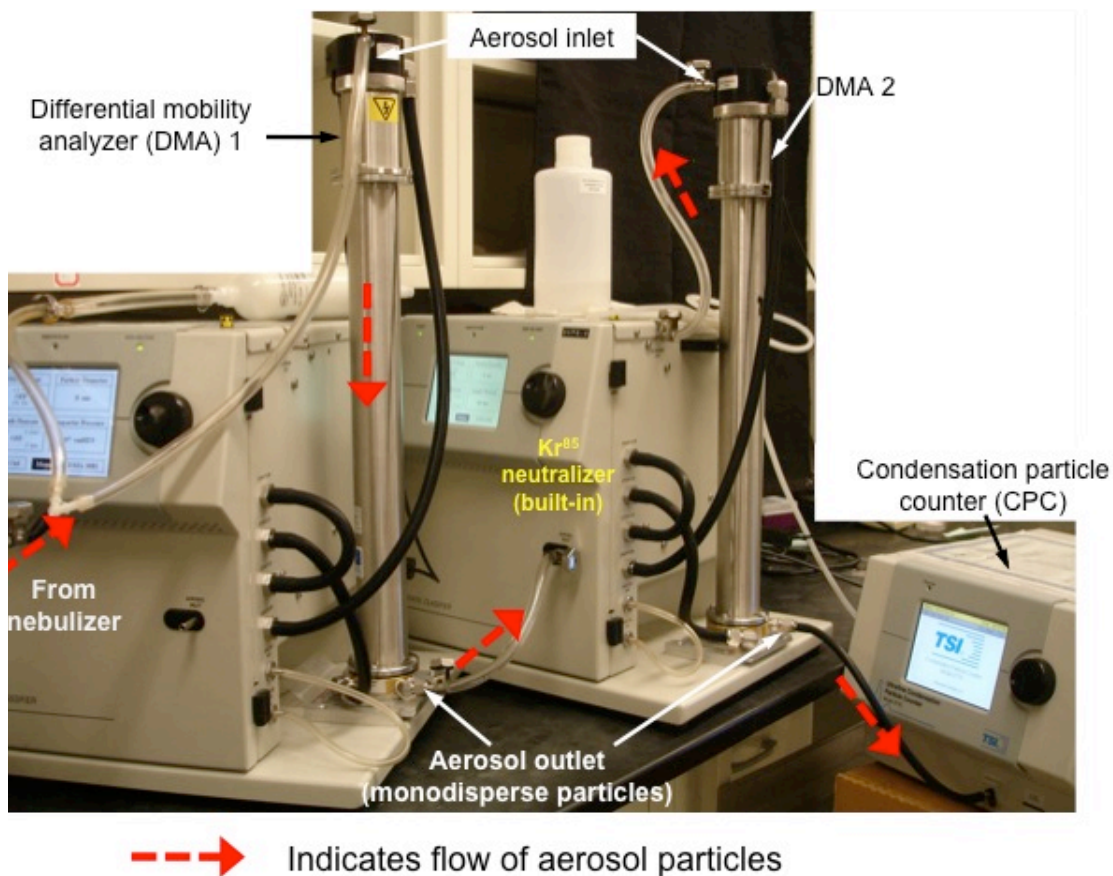
**Figure I-10:** Tandem differential mobility setup used in the charge distribution study of Chapter 6.

The first DMA selects particles with a specific electrical mobility. Then particles are passed through a $Kr^{85}$ neutralizer where they reach the Boltzmann equilibrium charge-state. More specifically, particles are in charge equilibrium with the surrounding gas media and they carry mostly a single charge. Subsequently, the second DMA scans over a range of electrical motilities to obtain the particle size distribution.

**Table I-2:** Procedure to calculate the fraction of singly charged chlorosomes with and electrical mobility of 9.52 x $10^{-8}$ m$^2$/Vs, corresponding to a mobility diameter of 50 with +1 charge. A data reduction procedure has to be applied to subtract the contribution of larger particles with multiple charges that may have the same electrical mobility of 9.52 x $10^{-8}$ m$^2$/Vs (73 nm with +2, 91.9 nm with +3, and 109 nm with +4).

| Selected with DMA 1 | | | DMA 2 | | | | |
| $Z_p$ (x $10^{-8}$ m$^2$/Vs) | $D_p$ (nm) | Charge unit, $p$ | $Z_p$ (x $10^{-8}$ m$^2$/Vs) | Charge unit, p | $f_{p,B}$ [-] | Estimated $D_p$ (nm) | Measured $D_p$ (nm) |
|---|---|---|---|---|---|---|---|
| 9.52 | 50 | +1 | 9.52 | +1 | 0.1840 | 50.0 | 50.0 |
| | | | 19 | +2 | 0.0047 | 34.6 | 34.2 |
| | | | 28.6 | +3 | 0.0010 | 28.0 | - |
| | | | 38.1 | +4 | 0.0000 | 24.1 | - |
| | 73 | +2 | 4.77 | +1 | 0.2230 | 73.0 | 73.0 |
| | | | 9.53 | +2 | 0.0181 | 50.0 | 50.0 |
| | | | 14.3 | +3 | 0.0003 | 40.2 | |
| | | | 19.1 | +4 | 0.0000 | 34.6 | |
| | 91.9 | +3 | 3.17 | +1 | 0.2370 | 91.9 | 91.0 |
| | | | 6.39 | +2 | 0.0320 | 62.3 | 62.1 |
| | | | 9.51 | +3 | 0.0012 | 50.0 | 50.7 |
| | | | 12.7 | +4 | 0.0000 | 42.9 | - |
| | 109 | +4 | 2.36 | +1 | 0.2410 | 109.0 | 108.0 |
| | | | 4.37 | +2 | 0.0045 | 73.3 | 73.5 |
| | | | 7.09 | +3 | 0.0027 | 58.6 | 60.0 |
| | | | 9.46 | +4 | 0.0000 | 50.2 | - |
| | 124 | +5 | 1.9 | +1 | 0.2420 | 124.0 | 123.0 |
| | | | 3.81 | +2 | 0.0551 | 82.8 | 82.7 |
| | | | 5.71 | +3 | 0.0047 | 66.0 | 66.8 |
| | | | 7.61 | +4 | 0.0000 | 56.4 | - |

$Z_p$ is the electrical mobility, $D_p$ is the mobility diameter, p is the number of elementary charges, and $f_{p,B}$ is the fraction of particles with $p$ charges in the Boltzmann charge-state (i.e., the probability that a particle with mobility diameter $D_p$ carries $p$ charges).

• $Z_p = \dfrac{pe C_c(D_p)}{3\pi\mu D_p}$

- $e$ is the electron elementary charge $= 1.6 \times 10^{-19}$ C.

- $\mu$ is the gas viscosity.

- $C_c(D_p)$ is the Cunningham slip correction factor.

$$C_c(D_p) = 2.514 \frac{\lambda}{D_p} + 0.8 \frac{\lambda}{D_p} \exp\left(-0.55 \frac{\lambda}{D_p}\right)$$

- $\lambda$ is the gas mean free path (66 nm for air).

- The fraction of particles in the Boltzmann equilibrium charge state was calculated with:

$$f_{p,B} = \frac{2e}{\left(\pi D_p kT\right)^{1/2}} \exp\left(-\frac{p^2 e^2}{D_p kT}\right)$$

- $k$ is the Boltzmann constant $1.38 \times 10^{-23}$ m$^2$ kg s$^{-2}$ K$^{-1}$.

- $T$ is the absolute temperature.

# Appendix II: Curriculum Vitae

# Luis Balam Modesto López

Date of Birth: 02/21/1981
Email:    luis.modesto.lopez@gmail.com
Website: http://students.cec.wustl.edu/~lbm2
Office phone:  +1 (314) 935-6018

## Professional Profile

Aerosol scientist. Expertise in electrospray and charged particles deposition of nanostructured organic and inorganic materials with a number of applications, including materials charging, film synthesis, and inhalation studies. Diverse background in aerosol measurement techniques, particle collection and removal with electric fields, synthesis of nanoparticles by aerosol reactors, fabrication of nanostructured films by aerosol-assisted chemical vapor deposition, and colloidal science. Experience in the design of aerosol education modules. Languages: Spanish (native), English (fluent), Japanese (fluent).

## Education

- Doctor of Philosophy, Energy, Environmental & Chemical Engineering, Washington University in St. Louis, MO, United States. May 2010.
- Bachelor of Engineering, Chemical Engineering, Hiroshima University, Japan. March 2006.
- Associate of Engineering, Chemical Engineering and Materials Science, Miyakonojo National College of Technology, Japan. March 2004.

- Chemical Engineering Program, Autonomous University of San Luis Potosí, Mexico. Until February 2000.

## Honors and Awards

- Winner of Student Grant, American Association for Aerosol Research Annual Meeting, Minneapolis, MN, USA (2009).
- Cherryll and Alan Frick Scholarship, Washington University in St. Louis, MO, USA (2006 -2007).
- Kumahira Scholarship for International Students, Hiroshima, Japan (2005 -2006).
- Higashi-Hiroshima City International Exchange Council's Scholarship, Hiroshima, Japan (2004 – 2005).
- Scholarship of The Ministry of Education of Japan for Undergraduate Studies, Tokyo, Japan (2000 – 2004).
- Recognition for Highest Grades in the Chemical Engineering Program, Autonomous University of San Luis Potosi, Mexico (2000).

**Teaching Experience**

- *Unit Operations* (Spring 2007): Graded homework and exams.
- *Transport Phenomena I* (Fall 2007): Planned and conducted help sessions, graded homework and exams.
- *Senior Chemical Engineering Laboratory* (Fall 2008): Guided experiments, conducted discussion and help sessions, graded lab reports.


**Service**

- **Coordinator** (2008 – 2009), American Association for Aerosol Research Washington University in St. Louis Student Chapter. Organized monthly presentations and research discussions among students. Presented student chapter research projects at national meetings.
- **Officer** (2008 – 2009), Air and Waste Management Association Washington University in St. Louis Student Chapter. Organized monthly discussions and visit to coal power plant.
- **Research Mentor** (Washington University in St. Louis), Undergraduate Students: John Schupach (Fall 2008), Rohit Ray (Spring 2009); and High School Student: Jereme Kramer (STARS Fellow, Summer 2008).


**Publications**

*A. Referred Publications*
1. Ogi T, **MODESTO-LOPEZ LB**, Iskandar F, and Okuyama K (2007). Fabrication of a large area monolayer of silica particles on a sapphire substrate by a spin coating method. *Colloids and Surfaces A*, 297 (1-3), 71 – 78.
2. **MODESTO-LOPEZ LB**, Pasteris JD, and Biswas P (2009). Sensitivity of micro-Raman spectrum to crystallite size of electrospray-deposited and post-annealed films of iron-oxide nanoparticle suspensions. *Applied Spectroscopy,* 63(6), 627 – 635.
3. **MODESTO-LOPEZ LB**, Thimsen EJ, Collins AM, Blankenship RE, and Biswas P (2010). Electrospray-assisted characterization and deposition of chlorosomes to fabricate a light-harvesting biomimetic device. *Energy and Environmental Science,* 3, 216 – 232.
4. **MODESTO-LOPEZ LB**, and Biswas P (2010). Role of the effective electrical conductivity of nanosuspensions in the generation of $TiO_2$ agglomerates with electrospray. *Journal of Aerosol Science. In print.*
5. **MODESTO-LOPEZ LB**, Kettleson E, and Biswas P. (2010) Soft X-ray charger (SXC) system for use with electrospray for mobility measurement of bioparticles. *Journal of Electrostatics. In review.*
6. Chattopaydhay S**, MODESTO-LOPEZ LB**, Venkataraman C, and Biswas P (*2010*). Size distribution and morphology of liposome aerosols generated by two methodologies. *Aerosol Science and Technology. In review.*

*B. Manuscripts in Preparation*
1. **MODESTO-LOPEZ LB**, Collins AM, Wen JZ, Blankenship RE, and Biswas P (2010). In-flight charging of natural light-harvesting complexes by aerosol methodologies.
2. An WJ, **MODESTO-LOPEZ LB**, Zhu L, and Biswas P (2010). Nanobio hybrid system with natural light-harvesting catalyst for hydrogen production. *Journal of the American Chemical Society.*

*C. Conference Proceedings*
1. **MODESTO-LOPEZ LB**, Thimsen EJ, and Biswas P. Electrospray deposition characteristics of $TiO_2$ nanoparticles suspensions for thin film fabrication. October 2008. American Association for Aerosol Research Annual Meeting. Orlando, FL, USA.
2. Thimsen E, Collins AM, **MODESTO-LOPEZ LB**, Blankenship RE, and Biswas P. Bionano antenna-reaction center (ARC) hybrid solar cells facilitated by aerosol processing. October 2008. American Association for Aerosol Research Annual Meeting, Orlando, FL, USA.
3. **MODESTO-LOPEZ LB**, Collins AM, Blankenship RE, and Biswas P. Characterization of chlorosomes using mobility-base techniques and electrospray deposition to create nanobio hybrid structures for efficient solar energy harvesting. August 2009. American Chemical Society Fall Meeting. Washington, DC, USA.
4. **MODESTO-LOPEZ LB**, Collins AM, Blankenship RE, and Biswas P. Characterization and deposition of natural light-harvesting chlorosomes using electrospray. October 2009. American Association for Aerosol Research Annual Meeting. Minneapolis, MN, USA.

*D. Posters*
1. Hogan Jr. CJ, **MODESTO-LOPEZ LB**, and Biswas P. Synthesis of nanoparticles and nanostructured films using biological complexes. September 2007. American Association for Aerosol Research Annual Meeting. Reno, NV, USA.
2. **MODESTO-LOPEZ LB**, Kettleson E, and Biswas P. Application of a soft X-ray charger in charge-reduced electrospray mobility analysis of biological particles. October 2009. American Association for Aerosol Research Annual Meeting. Minneapolis, MN, USA.
3. Chattopadhyay S, **MODESTO-LOPEZ LB**, Venkataraman C, and Biswas P. Aerosolization of nanometer-sized liposome suspension by electrospray. October 2009. American Association for Aerosol Research Annual Meeting. Minneapolis, MN, USA.
4. **MODESTO-LOPEZ LB**, Collins AM, An W-J, Blankenship RE, and Biswas P. Characterization of photosynthetic antenna complexes and fabrication of biomimetic light-harvesting devices by aerosol techniques. January 2010. Photosynthetic Antenna Research Center (PARC) Meeting. St. Louis, MO, USA.